

The effect of long chain branching on processibility of polymer melts

Jan Musil

Bachelor Thesis
2006



Tomas Bata University in Zlín
Faculty of Technology

Univerzita Tomáše Bati ve Zlíně
Fakulta technologická
Ústav výrobního inženýrství
akademický rok: 2005/2006

ZADÁNÍ BAKALÁŘSKÉ PRÁCE (PROJEKTU, UMĚLECKÉHO DÍLA, UMĚLECKÉHO VÝKONU)

Jméno a příjmení: **Jan MUSIL**

Studijní program: **B 3909 Procesní inženýrství**

Studijní obor: **Technologická zařízení**

Téma práce: **The Effect of Long Chain Branching on Processibility of Polymer Melts**

Zásady pro vypracování:

1. Vypracujte literární studii na dané téma.
2. Provedte měření smykové a elongační viskozity pro taveninu mLLDPE s různým stupněm větvení, a to na základě vhodně vybrané experimentální metody.
3. Popište naměřená data vhodným reologickým modelem včetně kvantifikace stupně větvení na základě parametrů daného modelu.
4. Ohodnoťte vliv větvení na zpracovatelnost mLLDPE vytlačováním.

Rozsah práce:

Rozsah příloh:

Forma zpracování bakalářské práce: **tištěná/elektronická**

Seznam odborné literatury:

1. Morrison, F.A.: **Understanding Rheology**. New York, 2001.
2. Cogswell, F.N.: **Polymer Melt – A Guide for Industrial Practice**. Cambridge, 1994.
3. Macosko, CH.W.: **Rheology–Principles, Measurements and Applications**. New York, 1994.
4. Zatloukal, M., Vlček, J., Tzoganakis, C., Sáha, P.: **Improvement in techniques for determination of extensional rheological data from entrance flows: computational and experimental analysis**, *J. Non – Newt. Fluid Mech.*, 107 (2002).
5. Sentmanat, M.L.: **Miniature universal testing platform: from extensional melt rheology to solid-state deformation behaviour**, *Rheol. Acta*, 43 (2004).

Vedoucí bakalářské práce:

doc. Ing. Martin Zatloukal, Ph.D.

Centrum polymerních materiálů

Datum zadání bakalářské práce:

14. února 2006

Termín odevzdání bakalářské práce:

13. června 2006

Ve Zlíně dne 19. ledna 2006

prof. Ing. Josef Šimoník, CSc.
děkan



doc. Ing. Miroslav Maňas, CSc.
ředitel ústavu



ABSTRAKT

Polymerní taveniny jsou při toku ve vytlačovacích hlavách (paralelní, sbíhavé či rozbíhavé štěrbiny, výtoková oblast výstupní štěrbiny) často vystaveny intenzivnímu smykovému a elongačnímu toku, což může při dosažení kritických podmínek vyvolat poruchy toku a následně destabilizaci celého zpracovatelského procesu. Stanovení smykové a elongační viskozity je pak zcela nezbytné pro navržení vhodného designu vytlačovací hlavy, ohodnocení vhodnosti příslušných typů polymerních materiálů a nastavení optimálních zpracovatelských podmínek. Z tohoto pohledu patří metalocenové typy polymerů mezi velmi obtížně zpracovatelné polymery. V této práci bylo studováno, zda-li je možné zpracovatelnost těchto materialů zlepšit zaváděním bočních větví na základní řetězec. Pro výzkum byl vybrán metalocenový typ LLDPE, který se používá na výrobu fólií vyfukováním. Celkem tři modifikace tohoto polymeru, odlišující se od sebe různým stupněm větvení, byly v první fázi reologicky hodnoceny, a to ve smykovém a elongačním toku z pohledu jejich zpracovatelnosti pomocí technologie vytlačování. Bylo provedeno experimentální stanovení časově závislých a ustálených elongačních viskozit (metody dle Cogswella, Bindinga a Sentmanatův elongační reometr), komplexní viskozity, elastické poddajnosti a bylo zjištěno, že s rostoucím stupněm větvení roste Newtonská viskozita, elastická poddajnost, elongační viskozita a mírně klesá smyková viskozita při vysokých deformačních rychlostech. Kvantifikace stupně větvení u všech tří vzorků byla provedena pomocí generalizovaného Newtonského a Maxwellového modelu. Zpracovatelnost polymerů byla následně hodnocena jejich vytlačováním na různě dlouhých hubicích, a to s ohledem na nástup jevu shark skin a lomu taveniny. Nejdůležitějším závěrem celé práce je zjištění, že s rostoucím stupněm větvení u metalocenového typu LLDPE do příslušného optima dochází ke stabilizaci toku zatímco s dalším růstem větvení se stává zpracovatelské okno užší. Z uvedeného vyplývá, že zavádění bočních větví do základního řetězce je vhodnou metodou, jak zlepšit zpracovatelnost metalocenových typů polymerů.

Klíčová slova: větvení, metalocenový typ LLDPE, elongační viskozita, shark skin, toková stabilita, Cogswellův model, Bindingův model, vstupní viskozita, Sentmanatův elongační reometr, generalizovaný Maxwellův model, generalizovaný Newtonův model

ABSTRACT

Effect of different long chain branching levels in metallocene based LLDPE on shear and extensional flow behavior has been carefully investigated from the processibility point of view. It has been revealed experimentally that by increasing of the branching level in mLLDPE up to the particular optimum level leads to flow stabilization whereas, beyond this optimum, the processing window has been found to be decreasing again.

Keywords: long chain branching, metallocene LLDPE, elongational viscosity, shark skin, flow stability, Cogswell model, Binding model, entrance viscosity, Sentmanat Extensional Rheometer, generalized Maxwell model, generalized Newtonian model

ACKNOWLEDGEMENT

I would like to express my sincere gratitude to all people who supported me during the work on the thesis.

I am especially grateful to my supervisor, doc. Ing. Martin Zatloukal, Ph.D. for his patience, guidance and support throughout the process of analysing data and writing thesis.

Many thanks go to doc. Ing. Anežka Lengálová, Ph.D. for her time she devoted to proof-reading of my Bachelor Thesis.

I should also like to acknowledge my uncle, Ing. Jaroslav Císař who helped me with photo-documentation of the experiments and DSC analysis.

I am also indebted to Ing. David Sámek, Ph.D. for his advice concerning about 3D figures and animations which are used in this thesis and its presentation.

The support of the project by the Czech Grant Agency (Grant no. 103/05/2311) is gratefully acknowledged.

We would like to thank Dipl.-Phys. Torsten Remmler from Malvern Instruments who allowed us to use 250 PSI pressure transducer and specially designed zero-length die for entrance viscosity measurements.

Last but not least, I would like to extend my gratitude to my family and all my true friends for their support.

I agree that the results of my Bachelor Thesis can be used by my supervisor's decision. I will be mentioned as a co-author in the case of any publication.

I declare I worked on this Bachelor Thesis by myself and I have mentioned all the used literature.

Zlín, May 28, 2006

Jan Musil

“πάντα ρεῖ” (everything flows)

Heraclites (c.535–475 B.C.)

TABLE OF CONTENTS

INTRODUCTION	10
I THEORETICAL BACKGROUND	11
1 EXTENSIONAL FLOWS IN POLYMER PROCESSING: MEASUREMENT AND MODELING.....	12
1.1 REVIEW OF BASIC POLYMER PROCESSING TECHNOLOGIES	12
1.1.1 Extrusion	12
1.1.2 Calendering	13
1.1.3 Injection moulding	13
1.1.4 Fiber spinning.....	14
1.1.5 Tubular film blowing	14
1.2 REVIEW OF ELONGATIONAL VISCOSITY MEASUREMENT DEVICES	15
1.2.1 Münstedt tensile rheometer	16
1.2.2 Meissner's metal belt clamping rheometer	17
1.2.3 Capillary rheometer.....	18
1.2.4 SER Universal Testing Platform.....	19
1.3 EFFECT OF LONG CHAIN BRANCHING ON VISCOSITIES OF POLYMERS	23
1.3.1 Shear flow	23
1.3.2 Elongational flow	24
1.4 CONSTITUTIVE EQUATIONS FOR POLYMER MELTS.....	25
1.4.1 Generalized Newtonian model	26
1.4.2 Generalized Maxwell model	27
2 AIMS OF THE WORK	28
II EXPERIMENTAL	29
3 MATERIALS.....	30
4 EQUIPMENT AND METHODS	31
4.1 CAPILLARY RHEOMETER ROSAND RH7-2	31
4.1.1 Shear viscosity determination technique.....	34
4.1.2 Entrance viscosity	35
4.1.3 'Effective entry length correction'	35
4.1.4 Corrected Cogswell method.....	37
4.1.5 Corrected Binding method	38
4.2 ROTATIONAL RHEOMETER ADVANCED RHEOMETRIC EXPANSION SYSTEM (ARES)	39
4.3 SER-HV-A01 UNIVERSAL TESTING PLATFORM	40
RESULTS AND DISCUSSION	45
CONCLUSION REMARKS.....	87
REFERENCES.....	88
LIST OF SYMBOLS	91
LIST OF FIGURES	95

LIST OF TABLES	100
LIST OF APPENDICES	101

INTRODUCTION

Viscosity is an important rheological property which expresses the resistance of the material to flow and two of them can be considered as the basic ones; shear and extensional viscosities. The former represents the resistance of fluid to the shear flow, whereas the latter reflects the resistance to the stretching. The knowledge of both viscosities is crucially important for better understanding of polymer molecular structure and it significantly helps to optimize the polymer processing conditions and equipment design to achieve stable flow conditions. In more details, there are technologies with predominantly shear flows (extrusion) or with predominantly extensional flows (the flow through converging channels in the extrusion/coextrusion dies, injection moulding, calendering and post die processes such as, fibber spinning, tubular film blowing, cast film [1-5, etc.] and with the aim to capture the flow behaviour in such flow situations properly into account, corresponding viscosity (or both) should be considered. It should be mentioned that the extensional viscosity of the material is much more difficult to measure in comparison with the shear viscosity as reported in the literature [6]. In the open literature, several types of extensional rheometers and experimental techniques have been developed [6-11] to measure this very important variable. However each of them is applicable for only limited range of extensional rates or stresses and the low experimental error can be observed only in the case when the elongation flow is stable for a sufficient time for large enough volume of the sample. Even if the extensional viscosity is determined for certain polymer, it is not trivial to make direct link between this property and polymer molecular structure (branching type, amount and its distribution for example). Therefore, the main aim of this work is to firstly, evaluate chosen experimental techniques for extensional viscosity determination. Secondly, to measure the extensional viscosity for metallocene based LLDPEs having introduced three different levels of the long chain branching. Thirdly, quantify the measured data through simple constitutive equations and finally, to evaluate the processibility of all three resins in the simple extrusion from the onset of the shark skin phenomenon point of view.

I. THEORETICAL BACKGROUND

1 EXTENSIONAL FLOWS IN POLYMER PROCESSING: MEASUREMENT AND MODELING

In this section, firstly, basic types of the flow domains occurring during the polymer processing with predominantly extensional flow components will be showed. Secondly, the review about the most popular techniques for the extensional viscosity determination will be provided. Thirdly, the effect of the molecular structure (long chain branching) on the flow behaviour will be discussed and finally, two, very simple constitutive equations will be introduced as a good candidates for quantification of the shear and extensional viscosities.

1.1 Review of basic polymer processing technologies

It should be kept in mind that virtually every type of polymer processing flow consist of both, shear and extensional flow components and therefore both shear and extensional viscosities should be used for the adequate flow description. In reality, the complex industrial flows are often simplified in such a way that the minor flow component is neglected and the flow situation is viewed as the simple shear flow or as the simple extensional flow, which significantly reduces the amount of the needed rheology characterization as well as computational difficulties. In many cases, the situation is even more simplified due to difficulties connected with the extensional viscosity measurement, i.e. even if the flow situation consist of predominantly by the extensional flow, only shear viscosity curves are employed. Of course, this simplification usually leads to unrealistic representation of the flow in many cases. With the aim to see where the extensional flow components plays the important role in the polymer processing, and thus should be taken into account, short overview in this sense is provided bellow.

1.1.1 Extrusion

During the flow in the extrusion dies, polymer melts usually flows through converging channels, usually occurring at the die exit region, where significant extensional flow components occur as visible in Fig. 1 [7]. In more detail, the elongation flow is uniaxial and planar for circular and flat die, respectively. As visible in Fig. 1, during the extensional flow, the cross sectional area is reduced significantly due to velocity rearrangement occurring at the converging channel.

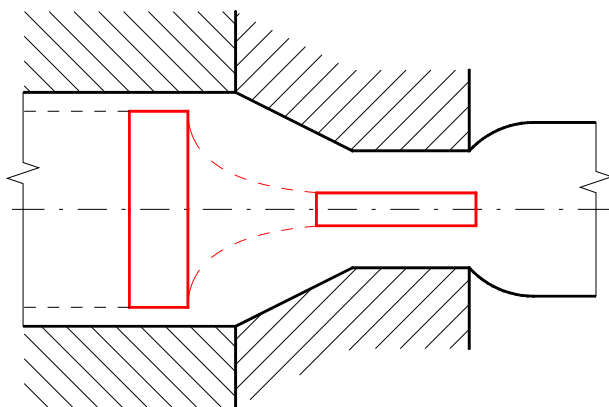


Fig. 1. Flow through extrusion die (material is flowing from left to right)

1.1.2 Calendering

Calendering is based in feeding plasticized material between two rotating rolls [12]. As shown in Fig. 2, the rolls rotating in opposite directions draw the material into the nip and the material element is both, intensively sheared and stretched due to presence of the planar elongational flow.

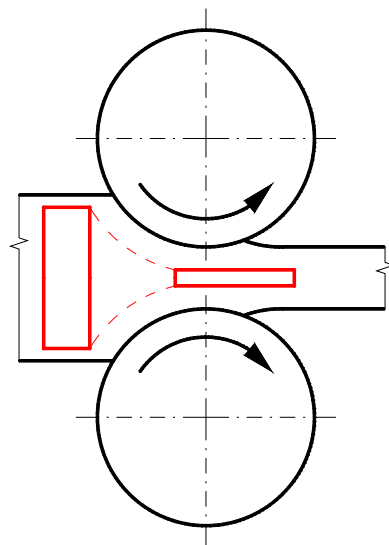


Fig. 2. Calendering

1.1.3 Injection moulding

Fig. 3 presents the scheme of injection moulding process [13]. In this technology, the polymer melt is injected into the closed hollow mould in very high speed by the piston/crew (represented by thin dashed lines) which forces the melt into the mould (the arrows mean pressure). As visible in Fig. 3 on the right side, the front part of the melt

stream filling the mould (in the figure marked as red) is stretched significantly and the extensional flow occurring in this area can be uniaxial, planar or biaxial according to type of the mould.

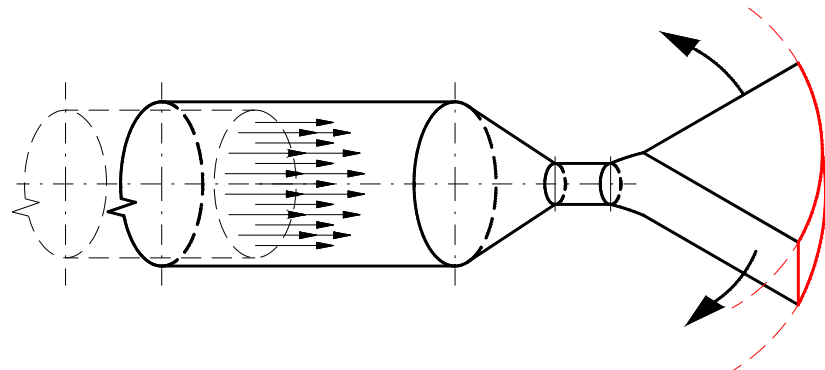


Fig. 3. Injection moulding

1.1.4 Fiber spinning

Fiber spinning is technology during which the annular extrudate at the post die area is stretched significantly by the haul off device where uniaxial elongational flow dominates i.e. the polymer chains are stretched in one direction, as shown in Fig. 4 as the red element, and shrinks equivalently in other two directions for isotropic materials. Very high level of the molecular orientation occurring during this process significantly improves tensile properties of final fibers.

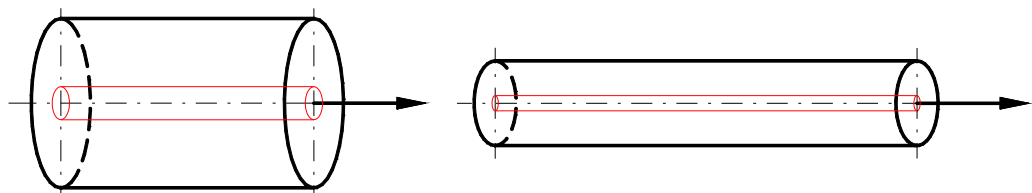
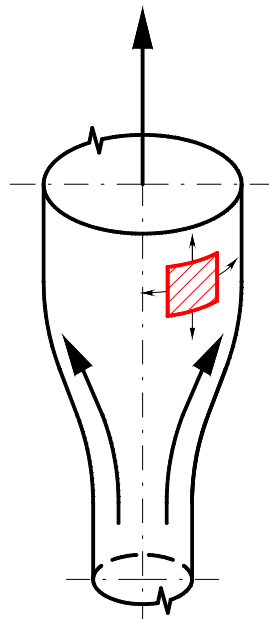


Fig. 4. Fiber spinning

1.1.5 Tubular film blowing

The tubular film blowing process is technology for the film production during which the polymer melt is extruded through annular die to form the tube [1]. Due to internal pressure and the take-up force at the post die area, the tube is inflated and cooled down as visible in Fig. 5 (the take-up force is visualized here as the arrow on top of the bubble, the inflation as the two symmetric arrows inside the bubble and deformed bubble

element as red). In this case, it is clear, that the biaxial extensional flow dominates in this case.



*Fig. 5. Tubular
film blowing*

From the above mentioned examples, it is evident that the knowledge of extensional viscosity is crucially important for understanding the relationships between polymer material, optimum processing conditions and equipment design.

1.2 Review of elongational viscosity measurement devices

As shown above, the knowledge of the extensional viscosity is crucially important in many industrial flows and thus the relevant question is in what way and how precisely this important rheological property can be measured. To answer these two questions, the most often used instruments and experimental procedures for the determination of extensional viscosity are introduced in next section and their advantages/disadvantages are carefully discussed.

1.2.1 Münstedt tensile rheometer

The first elongational rheometers were introduced at the end of the 1970's years. Probably the best known is the rheometer by Münstedt [8], [14] which was introduced in 1979. The principle of operation is shown in Fig. 6 [14].

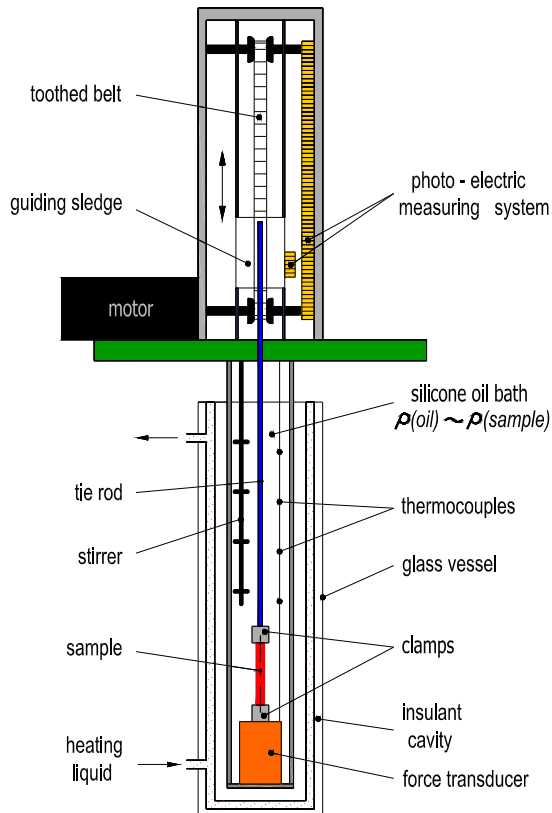


Fig. 6. Schematic drawing of Münstedt tensile rheometer

At this type of tensile rheometer the sample is put into two clamps, one of which is situated on the force transducer, the other is attached to the tie rod. When the sample is placed into clamps, the inside space of the rheometer is filled with silicone oil. The density of silicone oil has to be approximately equal to the density of the sample to limit the effect of the gravity force. The silicone oil also ensures constant temperature distribution along the sample. The required temperature is reached by heating liquid in the outside shell. To keep ideal temperature distribution, the silicone oil is mixed by a stirrer. The temperature is taken by thermocouples, which are placed at different distances from the sample. Heat losses are limited by the insulating cavity between heating-liquid space and the glass vessel.

The extensional viscosity is determined with the aid of the force transducer data and photo-electric measuring system. The advantage of this type of elongational rheometer consists in capability to measure the recoverable portion of elongation and stop the movement of the clamps at different states of deformation.

1.2.2 Meissner's metal belt clamping rheometer

For the measurement of equibiaxial and planar elongational viscosities two types of rheometers were developed by Meissner [6], [15]. The first one was introduced more than 30 years ago, the other, novel version, was revealed in 2003. The scheme of novel version is outlined in Fig. 7 [15].

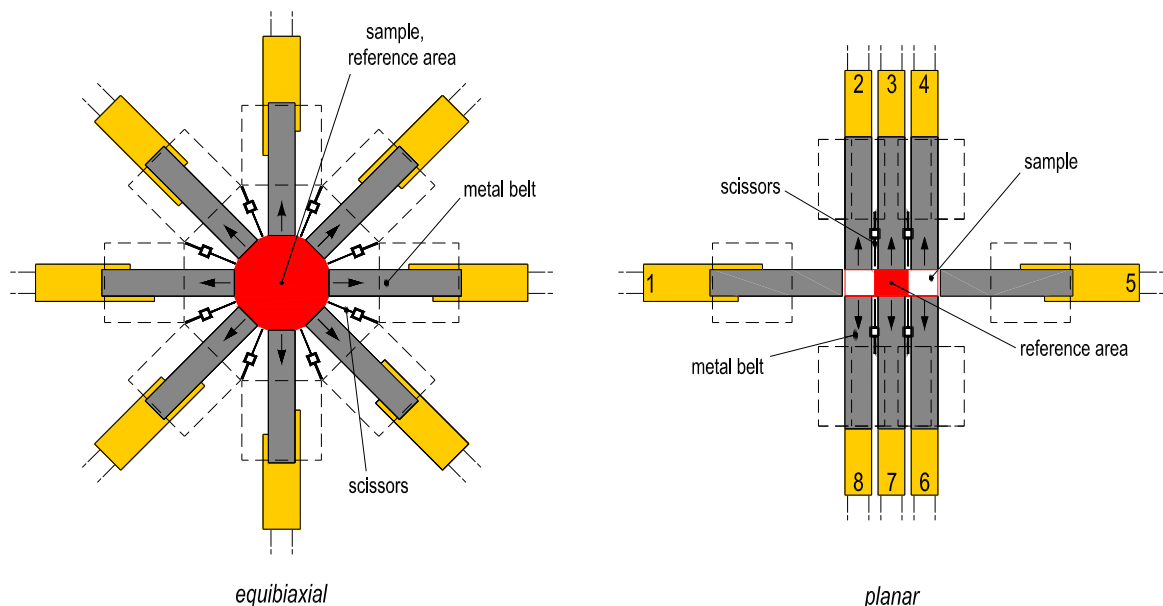


Fig. 7. Scheme of Meissner's metal belt clamping rheometer producing equibiaxial and planar elongational flows

The sample is in the form of polymer film. It is clamped in the rheometer with a metal belt, which ensures stretching the sample. In the case of equibiaxial elongation eight clamps are placed in circle. All metal belts rotate at the same constant speed. On the contrary, in planar elongation six clamps (2-4, 6-8 in Fig. 7) rotate, while clamps 1 and 5 do not and only hold the sample in a fixed lateral position. As can be seen in the figure, in the case of planar elongation the reference area cannot be a complete rectangle due to inhomogeneities near the ends of the sample. For this reason the reference area is only in the middle of the sample. Between the clamps there are scissors that intermittently cut into the sample so that with each cut its tips form a new reference area, which is extended

until the next cut is made. In both cases metal belts are situated inside the heated volume, but the force transducers and driving motors are placed outside. During the experiment the polymer sample is drawn between two rotating metal belts (Fig. 8 [15]) and the sample is supported by a cushion of inert gas (nitrogen).

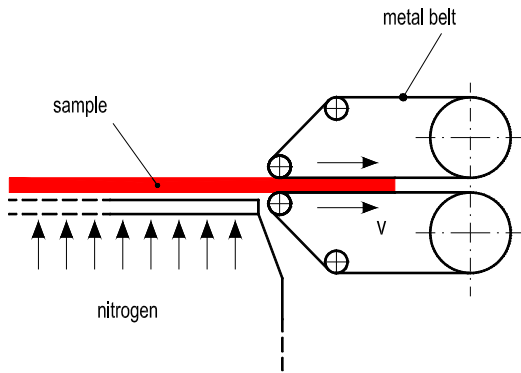


Fig. 8. Sample clamping by metal belts

1.2.3 Capillary rheometer

Capillary rheometer is a universal viscosimeter which can be used for the determination of shear viscosity, elongational viscosity, first/second normal stress differences and wall slip. The rheometer can be in several configurations. The first contains a single – bore barrel, the second a twin – bore (dual) barrel. The twin – bore types save the testing time because they are able to obtain two results in one test cycle. Another type is on – line capillary rheometer which is mounted on an extruder.

As shown in Fig. 9 [6], a modern capillary rheometer consists of a heated barrel and a piston that drives molten material through a calibrated die. The geometry of the die can be changed to measure rheological properties at different conditions. The polymer sample is in the form of granules, which are filled to the reservoir and perfectly compacted. The sample size depends on the barrel size and the shear rate. An experimental difficulty is vortexes in the entrance region, where highly accurate pressure transducers are located. At the end of the die, where the melt exits, a typical elastic phenomenon appears – '*die swell*', which can be measured by a laser micrometer mounted below the die exit. Extensional viscosity can be determined through entrance pressure drop measurements and special computational treatment (Cogswell [16], Binding [17], Gibson [18] methods). The major advantage of entrance pressure drop technique is the capability to evaluate extensional viscosity at very high extensional strain rates ($10 - 1000 \text{ s}^{-1}$), which

is impossible to achieve on any other instrument. The main problem connected with this technique is non-homogeneous elongational flow occurring at the die entrance region.

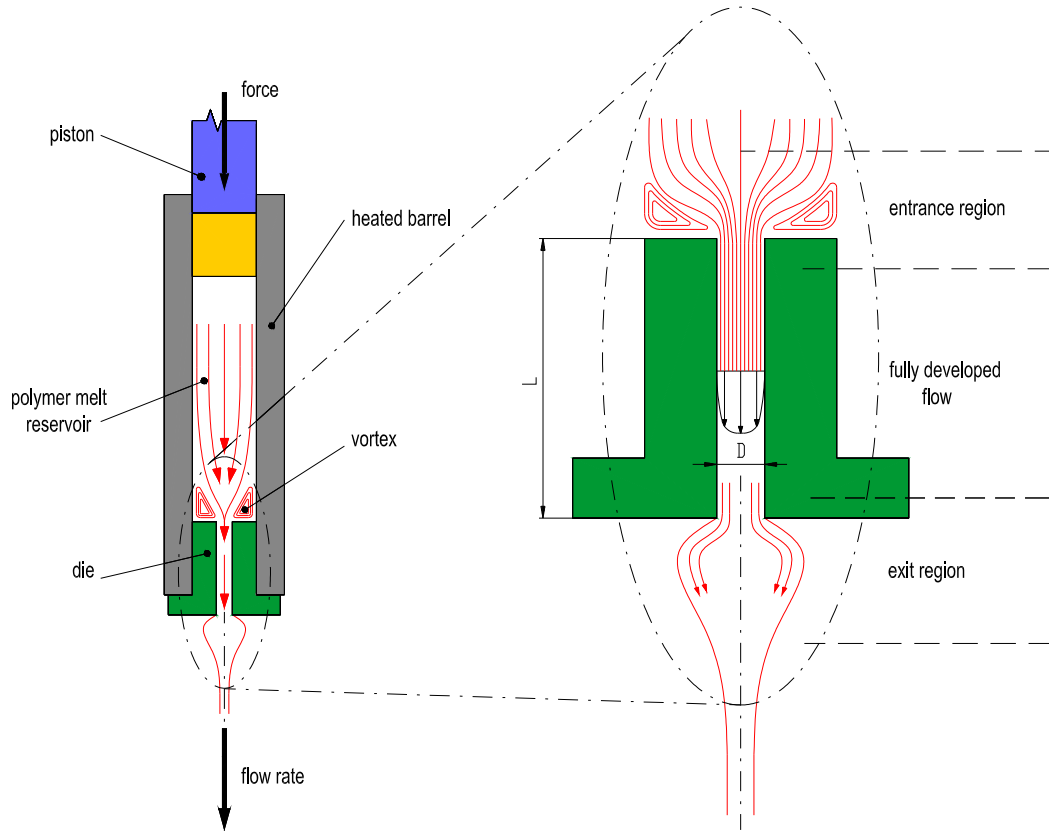


Fig. 9. Scheme of capillary rheometer

1.2.4 SER Universal Testing Platform

Sentmanat Extensional Rheometer (SER) Universal Testing Platform is a novel type of extensional rheometer, which was developed by M. L. Sentmanat [9], [10]. It was constructed as a detachable fixture for commercially available rotational rheometers. The SER can be used to perform uniaxial extension tests on polymer melts and elastomers.

The principle of operation is shown in Fig. 10 [9]. The main parts are master drum and slave drum, which turn in bearings placed in the chassis. Both drums are connected mechanically with intermeshing gears. The gears are rotated by a drive shaft and consequently cause turning of both drums. The rotation speed of the master and slave drums is equal, but opposite; this type of intermeshing gears changes only the direction of rotation (the gear ratio is 1:1). The sample of polymer is placed to securing clamps (one is on the master drum, the other on the slave drum) and with the rotation of both drums the sample is stretched above the unsupported length, L_0 (centreline distance between the

master and slave drums). As a result of the sample resistance tangential force will appear on both drums. This force produces torque, \bar{T} , which is measured by torque transducer on the torque shaft.

The worldwide patented technology applied on this type of extensional rheometer has several advantages. Firstly, the deformation zone is permanently visible from one place. Secondly, this platform is possible to mount on commercially available rotational rheometers (in both configurations: Controlled-Rate Rheometer and Controlled-Stress Rheometer) as a host system. Another advantage is that this rheometer places no lateral load on the torque transducer. Last but not least, an advantage is the versatility, because not only the extensional rheology can be performed on this platform but it is also able to carry out other types of tests: T – peel/adhesion, friction, tear, tensile and high / rate [9], [10].

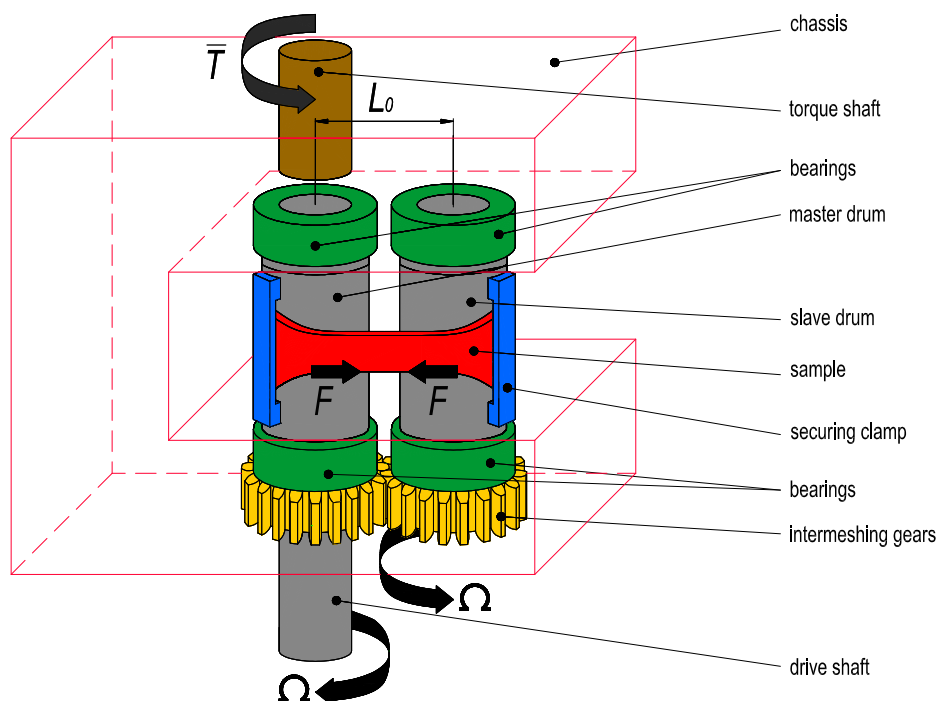


Fig. 10. Scheme of SER Universal Testing Platform. This type is mounted on Controled - Rate rotational rheometer Configuration (CRR), which has a separate motor and transducer (L_0 - unsupported length, Ω - drive shaft rotation rate, \bar{T} - torque, F - tangential force)

The behaviour of the sample during the experiment is shown in Fig. 11 (adapted from [9]). The length of the sample increases while the cross-section area decreases. Elongational viscosity is determined from the measured torque.

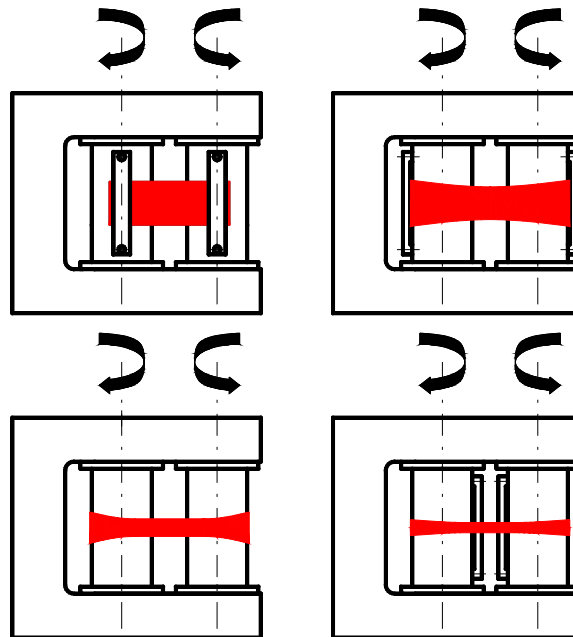


Fig. 11. Behaviour of the sample during the experiment on SER

The comparison between SER and other extensional rheometers is shown in Fig. 12 [19]. As can be seen, SER can be used to perform wide spectrum of polymer testing whereas common extensional rheometers can be used to investigate melt extensional viscosity only.

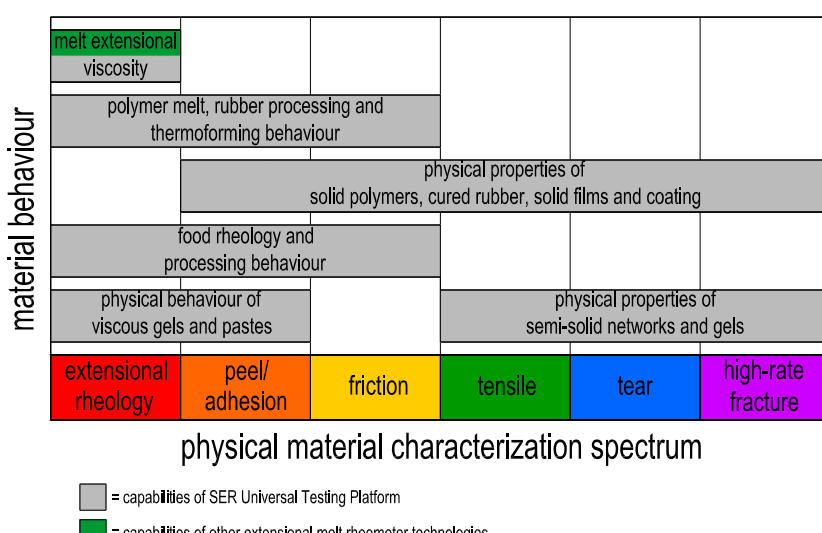


Fig. 12. Comparison of the capabilities of SER Universal Testing Platform and other melt rheometer technologies

At the end of this chapter we present the conditions, sampling and other factors relevant to the above described rheometers.

Tab. 1. Extensional rheometers overview, (adapted from [6])

Feature	Münstedt tensile rheometer	Meissner's metal belt clamping rheometer	Capillary rheometer	SER Universal Testing Platform
Type of elongation	Uniaxial	Planar or equibiaxial	Uniaxial	Uniaxial
Sample	Polymer film	Polymer film	Granules	Polymer film
Sample size	10 g; care must be taken to minimize end effects	< 2 g; requires careful preparation and loading	40 g minimum	5 – 200 mg
Restriction of gravity force	Silicone oil	Inert gas cushion	None	Geometry of the sample and its clamping
Viscosity range	High viscosity	High viscosity	Both low and high viscosities	> 10 000 Pa.s (zero-shear viscosity)
Flow stability	Subject to gravity, tension and air currents	Can be unstable at high rates	Unstable at very high rates	Stable up to 20 s ⁻¹
Homogenous	Not at the ends	Could be, with care	No – mixed shear and elongational flow	Yes – truly uniform extensional deformation
Pressure effects	None	None	Yes – compressibility of melt in the reservoir could cause difficulties	None
Elongational rates	Maximum rates depend on clamp speeds	Maximum elongational rate is limited by the ability to maintain the sample in steady flow	High and low rates possible	Maximum recommended elongational strain rate is 20 s ⁻¹

1.3 Effect of long chain branching on viscosities of polymers

The shape of viscosity curves is affected by many factors. Beside molecule weight, polydispersity, flow memory, temperature and pressure also long chain branching has an important effect [6]. Basically, polymers are divided into two groups – linear and branched. The former has only the main chain, while the latter contains side chains (branches) connected to the backbone. These branches can significantly influence the flow behaviour of the material. The differences between the two types of molecules are shown in Fig. 13.

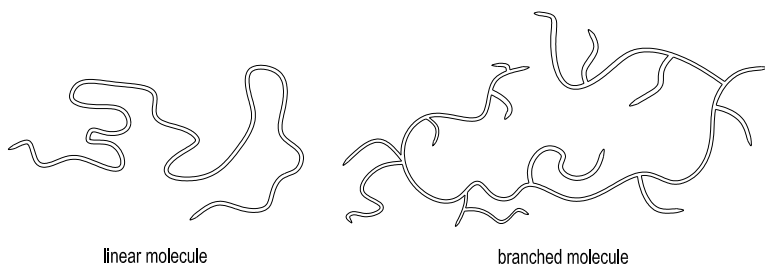


Fig. 13. Linear and branched molecule of polymers

1.3.1 Shear flow

Although there are several theories [20] which explain the behaviour of polymer chains at flows (shear and extensional), this behaviour is not fully understood so far.

One very simple theory [7] is based on the idea that the molecules are entangled into clumps and it is assumed that at shear flow these clumps are not entangled, but only slide, which is visualized in Fig. 14.

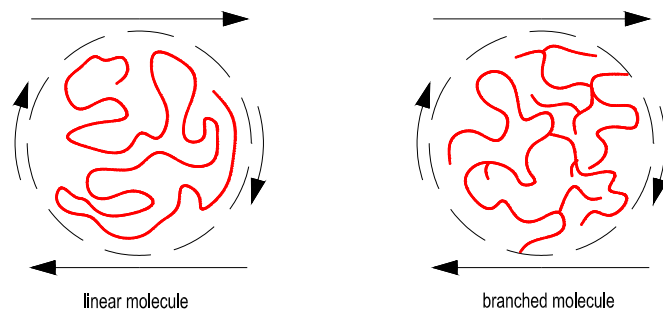


Fig. 14. Linear and branched molecule at shear flow

Based on this simplified theory the differences between linear and branched polymers are very difficult to distinguish from shear viscosity curve, which is also confirmed experimentally. As an example a study can be shown [21] which concentrated on the

differences between two identical types of polyethylene (LDPE), produced in two batches. The results are shown in Fig. 15 [21].

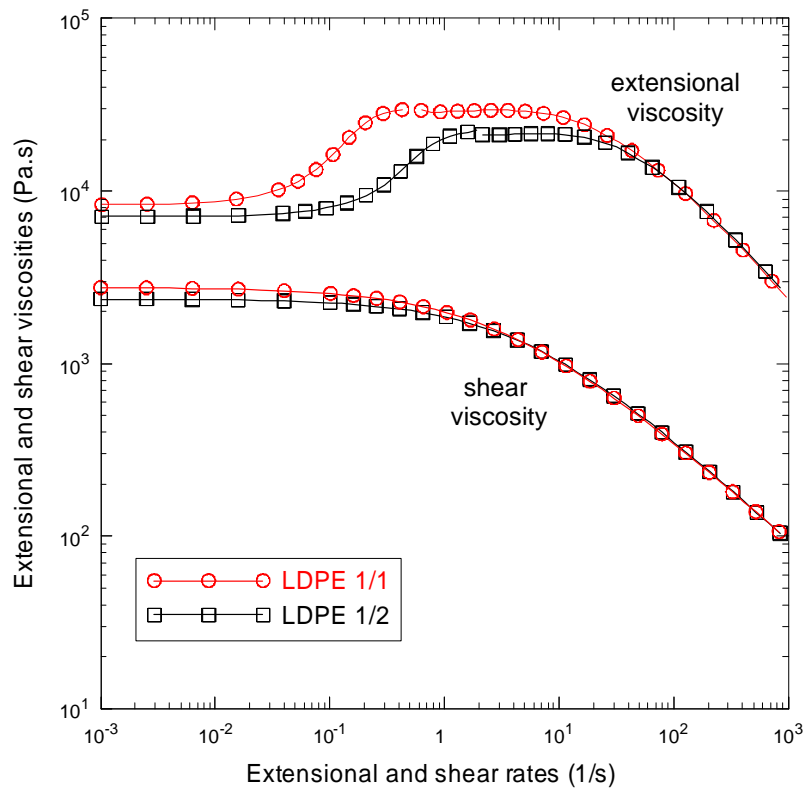


Fig. 15. Linear and branched molecule at shear flow

From this graph it is evident that while under shear the two batches behave nearly identically, their extensional flow is different. Thus, shear flow is not able to distinguish little variances in the structure of the material. On the contrary, from elongational curves the high sensitivity to the structure of the polymer is clearly seen.

1.3.2 Elongational flow

As shown above, elongational viscosity is able to distinguish even a little variance in the structure of a polymer. The reason is that individual molecules which are rolled up to clumps are stretched under flow. Linear molecules show small resistance to flow, so extensional viscosity of the polymer will decrease with increasing rate.

On the other hand, the elongational viscosity curve of branched polymer will first increase and only then it will begin to decrease (see Fig. 15 for example). This phenomenon is called “strain–hardening”. The “strain–hardening” is caused by the initial resistance of entangled branched molecules to stretching. However, at higher rates the resis-

tance of entangled branched chains will be overcome and extensional viscosity will decrease. The differences between the two types of molecules in elongational flow are shown in Fig. 16 [7].

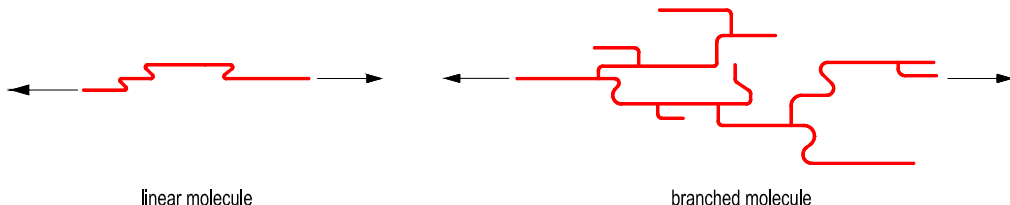


Fig. 16. Linear and branched molecule at elongational flow

1.4 Constitutive equations for polymer melts

Constitutive equations are mathematical relationships which are often derived from different assumptions and idealizations about mechanisms that produce stress and molecular or structural forces. These equations are mainly used in the case of liquids which have particular flow memory – polymers. The behaviour of polymers lies between Newtonian liquids and Hookean solids (because of relatively long macromolecules), therefore they cannot be described by simple physical laws.

Constitutive equations can be divided into two groups: differential and integral (according to the mathematical form). The constitutive equations help to predict a polymer melt behaviour during its processing and thus can save time and material in specifying optimum manufacturing conditions.

There are a number of models which can be used for a particular purpose [22]. In this work we use recently proposed Generalized Newtonian model [23] and Generalized Maxwell model [24], whose main advantage consists in analytical form of equations for description of shear and extensional viscosities. For this reason, the model parameters identification on the experimental data is straightforward and simple by using least square minimization method which is not the case when more sophisticated constitutive equations are employed.

1.4.1 Generalized Newtonian model

Generalized Newtonian model is derived from the simple Newtonian model, whose form is following [23]:

$$\underline{\tau} = 2\eta_0 \underline{\underline{D}} \quad (1)$$

where $\underline{\tau}$ represent extra stress tensor, η_0 is Newtonian viscosity, and $\underline{\underline{D}}$ stands for the deformation rate tensor.

The disadvantage of this model consists in η_0 . In this expression Newtonian viscosity is constant, but in reality the polymer melt viscosity depends on temperature and strain rate. In this work, we have used the following generalized expression for the Newtonian viscosity proposed in [23]:

$$\eta(T, II_D, III_D) = \eta(T, II_D)^{f(T, III_D)} \quad (2)$$

where T is temperature, II_D and III_D stands for the second and third invariants of deformation rate tensor, respectively.

The $\eta(T, II_D)$ in Eq. (2) is Carreau – Yasuda function.

$$\eta(T, II_D) = \frac{\eta_0 a_t}{\left[1 + (\lambda a_t \sqrt{2II_D})^a \right]^{\left(\frac{1-n}{a} \right)}} \quad (3)$$

where a_t is Arrhenius equation for temperature-dependent shift factor:

$$a_t = \exp \left[\frac{E_a}{R} \left(\frac{1}{273.15 + T} - \frac{1}{273.15 + T_r} \right) \right] \quad (4)$$

where E_a stands for activation energy, R represents universal gas constant, T_r is reference temperature; η_0 , λ , a , n are adjustable parameters.

For function $f(T, III_D)$ in Eq. (2) the following expression was proposed in [23]:

$$f(T, III_D) = \left[\frac{\tanh(\alpha a_t \sqrt[3]{4(III_D)} + 1)}{\tanh(1)} \right]^\zeta \quad (5)$$

where ζ is adjustable parameter and α is extensional strain-hardening parameter.

Extensional viscosity determination for polymer melt is given as:

$$\eta_E = \frac{\tau_{xx} - \tau_{yy}}{\dot{\varepsilon}} \quad (6)$$

The main advantage of this model is capability to capture both, strain hardening as well as strain softening in the extensional flows as discussed in [23].

1.4.2 Generalized Maxwell model

White, Metzner and Barnes proposed generalization of the Maxwell model in such way that viscosity and relaxation time are allowed to vary with the second invariant of the strain – rate deformation tensor [24], [25]. This dependence is expressed in the following form:

$$\underline{\underline{\tau}} + \bar{\lambda}(II_D) \overset{\nabla}{\underline{\underline{\tau}}} = \eta(II_D) \underline{\underline{D}} \quad (7)$$

where II_D stands for the second invariant of the rate of deformation tensor, $\bar{\lambda}(II_D)$ represents the deformation rate-dependent relaxation time, $\eta(II_D)$ is the deformation rate-dependent viscosity, $\underline{\underline{\tau}}$ stands for the stress tensor, $\overset{\nabla}{\underline{\underline{\tau}}}$ represents upper convected stress tensor derivate and $\underline{\underline{D}}$ is deformation rate tensor. As shown by Barnes and Roberts [24], with the help of specific functions of $\eta(II_D)$ and $\bar{\lambda}(II_D)$ (Eqs. (3) and (8)) the model can be used for very good description of elongational viscosity of real polymer melts, because it does not predict infinite elongational viscosity:

$$\bar{\lambda}(II_D) = \frac{\lambda_0 a_t}{1 + K_1 a_t II_D} \quad (8)$$

where λ_0, K_1 are constants. One additional condition is $(\lambda_0 / K_1) < (\sqrt{3} / 2)$.

The generalized Maxwell model is represented in Eqs. (3), (7) and (8) together with the physical limitation for λ_0 and K_1 . The generalized Maxwell model can be applied only in steady flows because in this model the relaxation time depends on II_D .

2 AIMS OF THE WORK

The main aim of this work is to firstly, evaluate chosen experimental techniques for extensional viscosity determination for two highly branched LDPEs. Secondly, to measure the extensional viscosity for metallocene based LLDPEs having introduced three different levels of the long chain branching by the help of two experimental techniques chosen in the first step. Thirdly, to quantify the measured data through simple constitutive equations and finally, to evaluate the processibility of all three resins in the simple extrusion from the onset of the shark skin phenomenon point of view.

II. EXPERIMENTAL

3 MATERIALS

In this work, the following material has been used:

- LDPE, Basell Lupolen 1840H (BASF): density 0.919 g.cm^{-3} , melt index 1.5 g/10 min , $M_w = 258,000 \text{ g.mol}^{-1}$, $M_n = 15,542 \text{ g.mol}^{-1}$
- LDPE, Escorene LD 165 BW1 (Exxon, USA): density 0.922 g.cm^{-3} , melt index 0.33 g/10min , $M_w = 366,300 \text{ g.mol}^{-1}$, $M_n = 30,280 \text{ g.mol}^{-1}$
- mLLDPE low level of LCB (virtually linear structure)
- mLLDPE middle level of LCB
- mLLDPE high level of LCB

It should be mentioned that the details about the last three materials are not provided in this work because they are confidential.

4 EQUIPMENT AND METHODS

In order to distinguish various degrees of chain branching two types of rheometers were chosen, they are introduced at section 1.3. First, capillary rheometer RH7-2 (Rosand Precision, Ltd., Great Britain) was used, because it is able to generate moderate as well as very high extensional flow. Second, the SER Universal Testing Platform (Xpansion Instruments, USA) has the ability of very precise determination of extensional viscosity at low extensional rates. The detachable fixture SER was mounted into the Advanced Rheometric Expansion System (ARES) Rheometrics as a host system.

4.1 Capillary rheometer Rosand RH7-2

As can be seen in Figs. 17 and 18, capillary rheometer Rosand RH7-2 is a twin-bore instrument which allows to perform two measurements at the same time. It is equipped with two (orifice and long) capillary dies. Due to twin-bore technology, shear and extensional data can be obtained without using a set of various capillary dies.

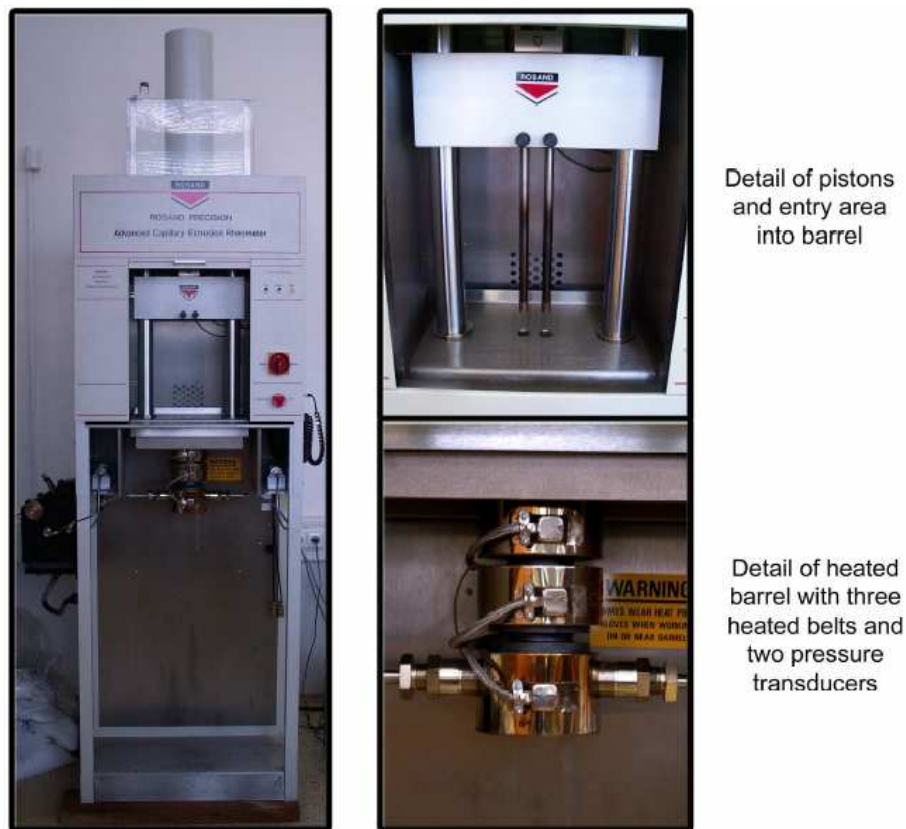


Fig. 17. Photo of Rosand RH7-2 twin-bore capillary rheometer

The measurements were performed in a constant piston speed mode at the shear rate range of $(0.05\text{-}2300) \text{ s}^{-1}$. In our measurements we used pressure transducers (Dynisco, USA) in ranges of (10000) PSI (68.9476 MPa), (1500) PSI (10.3421 MPa), (500) PSI (3.4473 MPa). In order to obtain the most accurate data of extensional viscosity for low extensional rates range, the highly sensitive pressure transducer (250) PSI (1.7237 MPa) calibrated into its down resolution limit was used for pressure recording at the entrance to the orifice capillary die (right-hand capillary in Figs. 18 and 19).

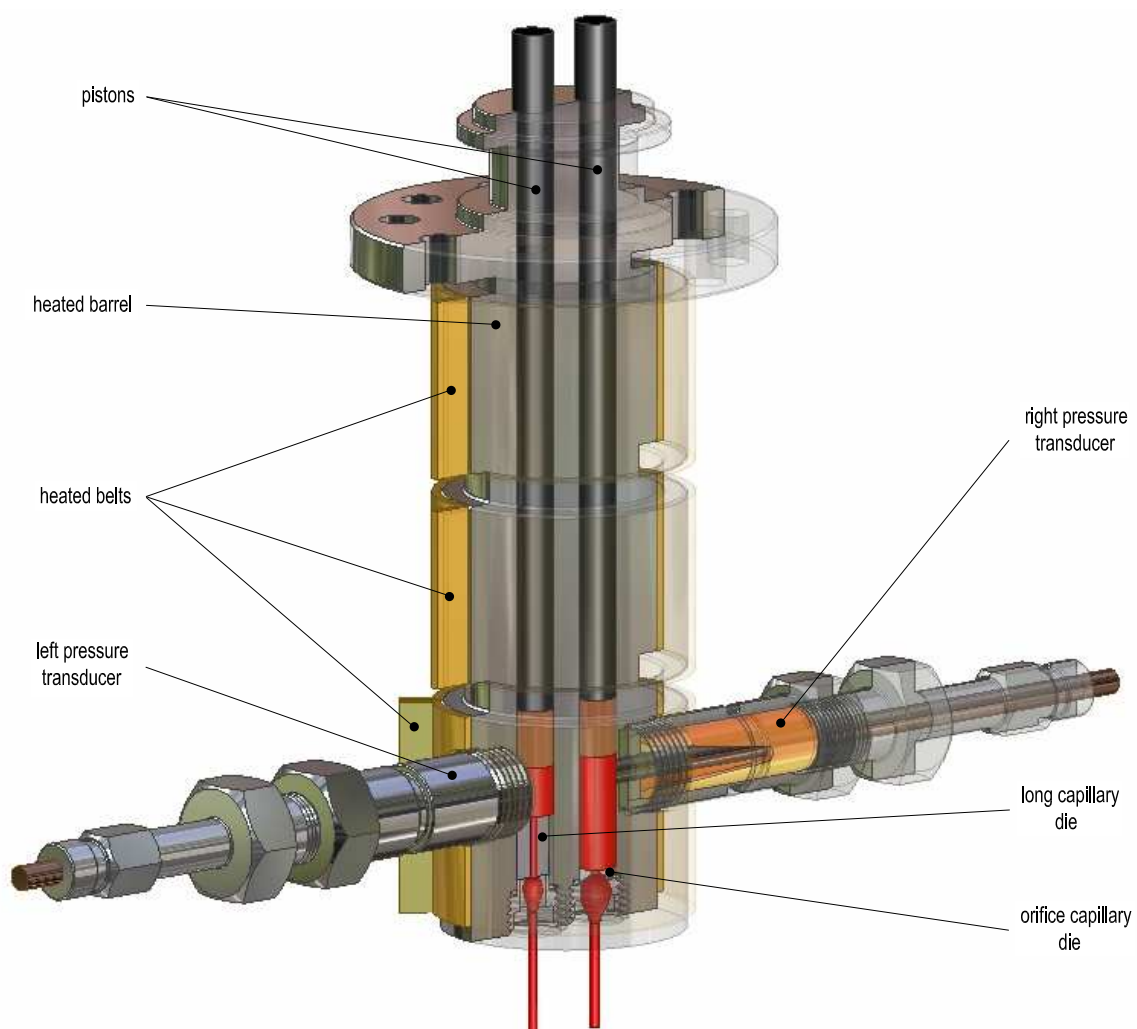


Fig. 18. Scheme of twin-bore capillary rheometer

Three sets of capillaries were used for the measurements. Their dimensions were following:

- orifice (short) capillary die: $L_{0C} = 0 \text{ mm}$, $D_{0C} = 1 \text{ mm}$

$$L_{0C} = 0 \text{ mm}, D_{0C} = 2 \text{ mm}$$

$$L_{0C} = 0 \text{ mm}, D_{0C} = 3 \text{ mm}$$

- long capillary die: $L_{LC} = 16 \text{ mm}$, $D_{LC} = 1 \text{ mm}$

$$L_{LC} = 32 \text{ mm}, D_{LC} = 2 \text{ mm}$$

$$L_{LC} = 27 \text{ mm}, D_{LC} = 3 \text{ mm}$$

The scheme of capillary dies is shown in Fig. 19. The diameter of barrel was $D_B = 15 \text{ mm}$.

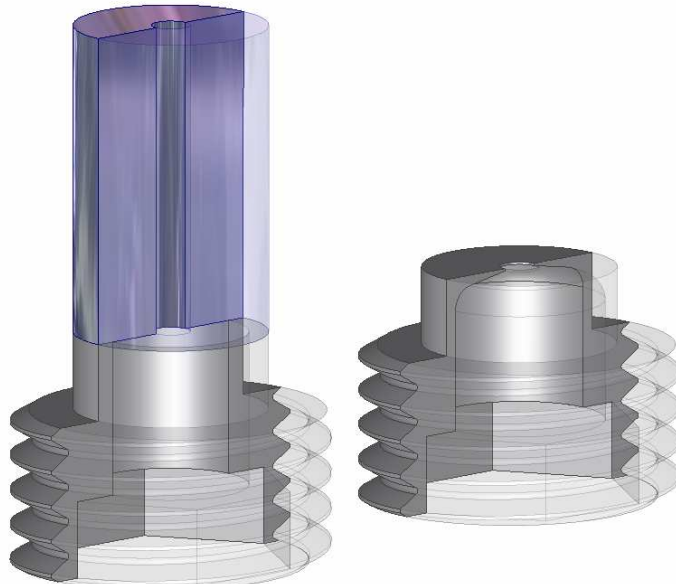


Fig. 19. Detail of long (left) and orifice (right) capillary dies

The rheological properties of the sample materials were investigated at temperatures 150°C, 160°C, 180°C and 200°C for LDPE Bassel Lupolen 1840H, 200°C for LDPE Escorene LD 165 BW1, 140°C, 150°C and 170°C for three types of mLLDPEs. In order to perfectly compact the sample granules and eliminate air bubbles, two preheating steps (for 3 and 6 minutes) and two compression steps (to 0.5 MPa) were applied before each experiment cycle.

4.1.1 Shear viscosity determination technique

With the aid of suitable software, the Rosand rheometer analyses the measured data. In order to obtain true shear stress data, it is necessary to use the Bagley correction. However, the twin-bore technology of the Rosand rheometer allows to apply the Bagley correction automatically on the measured data. It is not difficult to show that the shear viscosity can be determined from below provided relationships. The corrected shear stress is calculated according to following equation:

$$\tau_{xy} = \frac{(P_{LC} - P_{OC})}{2L_{LC}} R_C \quad (9)$$

where P_{LC} stands for pressure drop measured on the long capillary, P_{OC} on the orifice capillary; L_{LC} is the length of the long capillary, and R_C represents capillary die radius.

Apparent shear rate, $\dot{\gamma}_{APP}$, can be determined from equation:

$$\dot{\gamma}_{APP} = \frac{4Q}{\pi R_C^3} \quad (10)$$

where Q is volume flow rate and R_C represents capillary radius.

In order to obtain the real shear rate, Rabinowitsch correction has to be used on apparent shear rate:

$$\dot{\gamma} = \frac{4Q}{\pi R_C^3} \frac{3n+1}{4n} \quad (11)$$

where n represents power-law index and can be obtained from the following expression:

$$n = \frac{d(\log \tau_{xy})}{d(\log \dot{\gamma}_{APP})} \quad (12)$$

Finally, shear viscosity is simply:

$$\eta = \frac{\tau_{xy}}{\dot{\gamma}} \quad (13)$$

4.1.2 Entrance viscosity

In the case of capillary rheometer, the entrance pressure drop is measured (the pressure transducers are situated in the entrance region) by the help of the orifice die (right-hand capillary in Fig. 19). With the aid of apparent shear rate ($\dot{\gamma}_{APP}$) the entrance viscosity can be determined according to the following equation [11]:

$$\eta_{ENT} = \frac{P_{0C}}{\dot{\gamma}_{APP}} \quad (14)$$

where P_{0C} stands for the entrance pressure drop, which can be measured directly on the orifice capillary die or can be obtained from the Bagley plot.

Due to the fact that it is difficult or practically impossible to measure entrance viscosity at very low of $\dot{\gamma}_{APP}$, it seems to be very useful to fit the measured data by a suitable model and take the low apparent shear rate data from the model fit as the measurements. As was suggested in [11], the equation which describes the entrance viscosity dependence on the shear rate is following:

$$\log(\eta_{ENT}) = \log\left(\frac{\eta_{ENT,0}}{\left[1 + (\lambda' \dot{\gamma}_{APP})^{a'}\right]^{\frac{(1-n')}{a'}}}\right) \left[\frac{\tanh(\alpha' \dot{\gamma}_{APP} + \beta')}{\tanh(\beta')} \right]^{\xi'} \quad (15)$$

This is an empirical equation which combines a Carreau-Yasuda model and an additional term that controls strain-hardening behaviour; $\eta_{ENT,0}$ is the plateau-value of entrance viscosity, and λ' , a' , n' , α' , β' , ξ' are adjustable parameters.

For fitting the entrance viscosity data, a simplified version of the above equation ($a' = 1 - n'$ and $\beta' = 1$) will be used in this work:

$$\log(\eta_{ENT}) = \log\left(\frac{\eta_{ENT,0}}{\left[1 + (\lambda' \dot{\gamma}_{APP})^{a'}\right]}\right) \left[\frac{\tanh(\alpha' \dot{\gamma}_{APP} + 1)}{\tanh(1)} \right]^{\xi'} \quad (16)$$

4.1.3 ‘Effective entry length correction’

The Cogswell and Binding methods do not accurately predict the correct value of 3 (Trouton ratio) in uniaxial extension viscosity as shown in [11]. This number is the ratio of extensional viscosity to shear viscosity at low shear rates range (Newtonian plateau). For this reason the measured entrance viscosity data has to be treated through so

called ‘*effective entry length correction*’, which has recently been proposed in [11], i.e. the corrected entrance viscosity can be determined according to the following equation:

$$\eta_{\text{ENT,C}} = \frac{4\eta \left(\frac{L_{LC}}{D_{LC}} \right)_b \left[\left(\frac{L_C}{D_C} \right)_{Tr} - \left(\frac{L_{0C}}{D_{0C}} \right)_a \right]}{\left(\frac{L_{LC}}{D_{LC}} \right)_b - \left(\frac{L_{0C}}{D_{0C}} \right)_a} + \eta_{\text{ENT,a}} \quad (17)$$

where η is shear viscosity, $\left(\frac{L_{0C}}{D_{0C}} \right)_a$ represents ratio of length to diameter at orifice capillary and $\left(\frac{L_{LC}}{D_{LC}} \right)_b$ at long capillary, $\eta_{\text{ENT,a}}$ stands for entrance viscosity measured on the

orifice capillary die, and ratio $\left(\frac{L_C}{D_C} \right)_{Tr}$ is expressed as:

$$\left(\frac{L_C}{D_C} \right)_{Tr} = \frac{1}{2} \left(\frac{\eta_{\text{ENT,a,0}}}{2\eta_0} - \frac{\eta_{\text{ENT,0,e}}}{2\eta_0} \right) \frac{\left(\frac{L_{0C}}{D_{0C}} \right)_a - \left(\frac{L_{LC}}{D_{LC}} \right)_b}{\left(\frac{L_{LC}}{D_{LC}} \right)_b} + \left(\frac{L_{0C}}{D_{0C}} \right)_a \quad (18)$$

where $\eta_{\text{ENT,a,0}}$ represents the entrance viscosity plateau that is measured on an orifice capillary die with $\left(\frac{L_{0C}}{D_{0C}} \right)_a$ ratio, η_0 is the Newtonian viscosity, and $\eta_{\text{ENT,0,e}}$ stands for the entrance viscosity plateau, which is calculated from following relationships:

$$\eta_{\text{ENT,0,e}} = 1.633\eta_0 \quad (\text{Cogswell method}) \quad (19)$$

$$\eta_{\text{ENT,0,e}} = 1.8856\eta_0 \quad (\text{Binding method}) \quad (20)$$

4.1.4 Corrected Cogswell method

Equations and extensional flow parameters in Cogswell method are obtained through minimizing local pressure gradients in the converging region. This analysis is based on the following assumptions in the converging region [6]:

Assumptions for Cogswell analysis of contraction flow

1. Incompressible fluid;
 2. Funnel-shaped flow; no slip ($v_z = 0$) on funnel surface;
 3. Unidirectional flow in funnel region;
 4. Fully developed flow upstream and downstream;
 5. Axis symmetry;
 6. Pressure drops due to shear and elongation may be calculated separately and summed to given total entrance pressure loss;
 7. Neglected Weissenberg-Rabinowitsch correction, $\dot{\gamma} = \dot{\gamma}_{APP} = \frac{4Q}{\pi R_C^3}$;
 8. Shear stress is related to shear rate through a power law, $\tau_{xy} = m\dot{\gamma}_{APP}^n$;
 9. Elongational viscosity is constant;
 10. Shape of funnel is determined by the minimum generated pressure drop;
 11. No effect of elasticity (shear normal stresses neglected);
 12. Inertia neglected.
-

For determination of elongational curve Cogswell [16] derived following equations. Extensional stress is calculated according to below relationship:

$$\sigma_E = \frac{3}{8}(n+1)\eta_{ENT,C}\dot{\gamma}_{APP} \quad (21)$$

The extensional rate is express as:

$$\dot{\varepsilon} = \frac{4}{3(n+1)} \frac{\eta\dot{\gamma}_{APP}}{\eta_{ENT,C}} \quad (22)$$

where $\eta_{ENT,C}$ stands for corrected entrance viscosity, and η represents shear viscosity, which can be defined as:

$$\eta = \frac{\tau_{xyC}}{\dot{\gamma}_{APP}} \quad (23)$$

where τ_{xyC} means the corrected shear stress.

The extensional viscosity is then given by a simple ratio of extensional stress to extensional rate:

$$\eta_E = \frac{\sigma_E}{\dot{\varepsilon}} \quad (24)$$

4.1.5 Corrected Binding method

As shown in [17], the equations and extensional flow parameters, according to Binding method are obtained by minimizing the viscous energy dissipation in the converging region. Binding's assumptions are summarized below [6]:

Assumptions for Binding analysis of contraction flow

1. Incompressible fluid;
 2. Funnel-shaped flow; no slip ($v_z = 0$) on funnel surface;
 3. Unidirectional flow in funnel region (see assumption 10);
 4. Fully developed flow upstream and downstream;
 5. Axis symmetry;
 6. Shear viscosity is related to shear rate through a power law, $\eta = m\dot{\gamma}^{n-1}$;
 7. Elongational viscosity is given by power-law, $\eta_E = l\dot{\varepsilon}^{k-1}$;
 8. Shape of funnel is determined by the minimum work to drive flow;
 9. No effect of elasticity (shear normal stresses neglected);
 10. Quantities $\left(\frac{dR_C}{dz}\right)^2$ and $\frac{dR_C^2}{dz^2}$ related to funnel shape are neglected; this has the implication that the radial velocity is neglected when calculating the rate of deformation;
 11. Neglect energy required to maintain corner circulation;
 12. First normal stress difference due to the shear flow is neglected ($N_1 = 0$);
 13. Inertia neglected.
-

The extensional rate along the centreline in Binding analysis is:

$$\dot{\varepsilon} = \frac{(3n+1)(1+k)^2}{3k^2(1+n)^2} \frac{\eta \dot{\gamma}_{APP}}{\eta_{ENT}} \left(\frac{3n+1}{4n} \right)^n \quad (25)$$

The extensional stress is express as:

$$\sigma_E = \frac{2^{(k-1)} 3k(1+n)^2}{(3n+1)(1+k)^2} \frac{\eta_{ENT} \dot{\gamma}_{APP}}{I_{nk}} \quad (26)$$

The integral I_{nk} is determined from:

$$I_{nk} = \int_0^1 \left\{ \text{abs} \left[2 - \left(\frac{3n+1}{n} \right) \right] \zeta^{\frac{(1+n)}{n}} \right\}^{(k+1)} \zeta d\zeta \quad (27)$$

The unknown parameter k in Eqs. (24), (25) and (26) is calculated from following expression:

$$k = \frac{\hat{t}}{1 + n - \hat{t}} \quad (28)$$

where \hat{t} is defined as:

$$\hat{t} = \frac{d \log(\eta_{ENT})}{d \log(\dot{\gamma}_{APP})} - 1 \quad (29)$$

As shown in [11], the Eq. (26) can be simplified, when $n \in (0;1)$ on shape:

$$I_{nk} = \frac{n \left[\frac{(1+n)}{n} \right]^{(k+1)}}{2n + (1+n)(k+1)} \quad (30)$$

4.2 Rotational rheometer Advanced Rheometric Expansion System (ARES)

Fig. 20 shows the Advanced Rheometric Expansion System, which was used for determination shear viscosity, loss modulus, storage modulus and activation energy. All measurements were performed with 2 K FRTN1 and 2 K FRTN2 transducers (provided by TA Instruments) with a lower resolution limit of 0.02 g/cm.

The three different mLLDPE materials were measured in oscillation mode with range of frequencies ($0.1\text{-}100 \text{ rad.s}^{-1}$). The measurements were performed with parallel plates geometry (plate diameter was 25 mm). The sample thickness was 1 mm and the experimental temperatures were 140°C, 160°C, 180°C and 200°C.

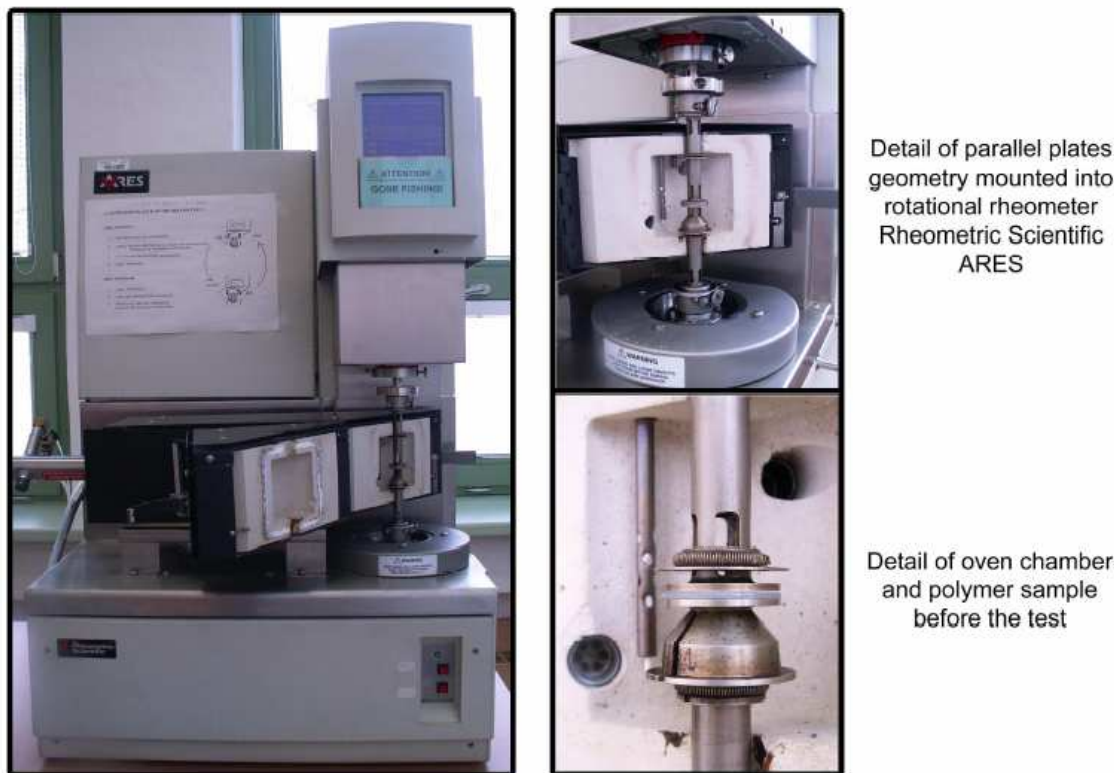


Fig. 20. Photo of Advanced Rheometric Expansion System ARES

4.3 SER-HV-A01 Universal Testing Platform

Fig. 21 shows the Advanced Rheometric Expansion System, which was used as a host system for the detachable fixture SER Universal Testing Platform from Xpansion Instruments. As can be seen in Figs. 10, 21 and 22, the SER Universal Testing Platform is an instrument which includes dual wind-up drums to guarantee truly uniaxial extension experiments on polymer melts.



Fig. 21. Photo of SER-HV-A01 Universal Testing Platform mounted in ARES

Note that SER-HV-A01 type was used in our measurements. The specifications of the instrument are following:

- diameter of the wind-up drum: 10.31 mm (0.406 in)
- stretch zone gage length: 12.72 mm (0.501 in)

The samples were prepared by compression-moulding of flat polymer samples and subsequent cutting into fixed width strips using a dual blade cutter. The dimensions of samples were:

- sample width: 12.7 mm (sample prepared by dual blade cutter with calibrated width)
- sample thickness range: (0.5-0.8) mm

With the aid of SER instrument the samples of three grades of mLLDPE were tested at temperature 140°C with the applied extensional rates in range (20s^{-1} , 10s^{-1} , 3.16s^{-1} and 1s^{-1}).

Extensional viscosity determination

The basic mathematical relationships for the determination of extensional viscosity will be introduced with reference to Figs. 10 and 22 [9].

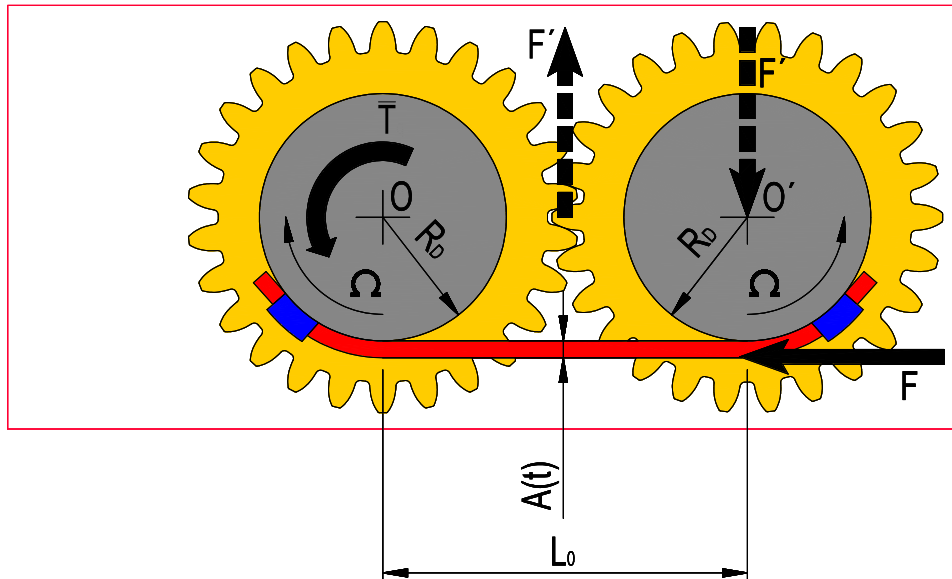


Fig. 22. Force diagram of SER Universal Testing Platform

As can be seen in figures, the tangential stretching force (F) on the slave drum and the resultant torque (\bar{T}) are measured with the aid of torque transducer of a decoupled drive motor and torque transducer host system. The meaning of the other symbols in Fig. 22 is following: Ω – drive shaft rotation rate, R_D – radius of drums, $A(t)$ – instantaneous cross-section area, F – tangential force and L_0 is unsupported length.

The extensional viscosity is determined from following relationships [9], [10]. For a constant drive shaft rotation rate, Ω , the elongational strain rate applied to the sample can be calculated according to equation:

$$\dot{\varepsilon} = \frac{2\Omega R_D}{L_0} \quad (31)$$

where L_0 stands for the fixed, unsupported length of the stretched, sample which is equal to the centerline distance between the master and slave drums (see also Fig. 10).

At the contact point of the intermeshing gears force F' acts, which counteracted by the tangential stretching force F on the slave drum. In the case of 1:1 gear ratio the intermeshing gear force F' can be calculated as a sum of moments about the slave drum's axis of rotation O' (as indicated in Fig. 22) according to the following expression:

$$F' = \frac{(F + F_F)R_D}{\frac{L_0}{2}} \quad (32)$$

where F_F represent the contribution of frictional force which may occur due to the friction of gears and bearings.

Force F' on the intermeshing gears is transposed as a radial force on the bearings and it is centered along the slave drum's axis of rotation, O' . Since the torque shaft is attached to the chassis along the master drum's axis of rotation, O , a total of moments about O axis can be expressed as:

$$\bar{T} = F'L_0 \quad (33)$$

After the substitution of Eq. (33) into Eq. (32):

$$\bar{T} = 2(F + F_F)R_D \quad (34)$$

As bearings and gears which are mounted into the SER unit are very precise, the friction term F_F is usually less than 2% of the stretch force F and it can be neglected for the values of torque greater than $4 \cdot 10^{-5}$ Nm. This results to a simplified expression for the measured torque:

$$\bar{T} = 2FR_D \quad (35)$$

In case there is no difference between the nominal and actual strain rates, the change of the instantaneous cross-section area, $A(t)$, of the stretched sample changes exponentially with time t for a constant elongational strain rate experiment:

$$A(t) = A_0 \exp[-\dot{\varepsilon}t] \quad (36)$$

where A_0 stands for the initial cross-section area of the unstretched sample, $\dot{\varepsilon}$ is the constant elongational strain rate and t represents the test time.

The width and thickness of the prepared polymer samples are measured at room temperature before clamping into SER system. Then, these dimensions are used for the

determination of the initial cross-section area, A_0 , of the unstretched sample. However, for melt rheology experiments the polymer samples exhibit a decrease in density upon melting, which is manifested as volumetric expansion of the sample span while it is clamped into the SER. For this reason the following expression should be used to calculate the cross-section area of the molten polymer sample:

$$A(t) = A_0 \left(\frac{\rho_s}{\rho_m} \right)^{\frac{2}{3}} \exp[-\dot{\varepsilon}t] \quad (37)$$

where A_0 is the cross-section area of the sample in the solid state, ρ_s represents the solid-state density, and ρ_m stands for the melt density of the sample.

For a constant elongational strain rate the equation for tensile stress growth, $\eta_E^+(t)$, of the stretched sample is:

$$\eta_E^+(t) = \frac{F(t)}{\dot{\varepsilon}A(t)} \quad (38)$$

where $F(t)$ is the instantaneous extensional force at time t , and it is determined with the aid of the measured torque signal, \bar{T} , and Eq. (30). This force represents the resistance of the sample to stretching.

RESULTS AND DISCUSSION

Entrance viscosity measurement issue

As has been mentioned in the above section, the very sensitive 250 PSI pressure transducer has been used to measure the entrance pressure drop by using the zero length die to achieve precise enough data. It has been found that the pressure calibration after each measurement is crucially important to get reliable entrance pressure drop, especially at low apparent shear rate range. The Fig. 23 shows six independent measurements of the entrance viscosity for the LDPE Escorene material where the pressure calibration has not been done after each measurement. On the other hand, the Fig. 24 shows the same experimental results but the calibration has been performed after each measurement. It is clearly visible, that specific care has to be done during the entrance pressure data collecting at very low apparent shear rates.

Comparison between corrected entrance pressure drop techniques and SER for highly branched LDPEs

Two highly branched LDPE materials (Basell Lupolen 1840H, Escorene LD 165 BW1) were used at the beginning to test reliability of the corrected Cogswell and Binding methodologies with respect to Sentmanat Extensional Rheometer.

At the first step, the measured entrance viscosities of both samples were measured and consequently fitted by the Eq. (16) as depicted in Figs. 24-25 and fitting parameters are provided in Tab. 2. It is clearly visible that in both cases, Eq. 16 represents the measured entrance viscosity data very well. In the second step, the model fitting lines for both materials were taken as the measurements. In the third step, effective entry length correction has been applied for these data with respect to Cogswell as well as Binding methods. Finally, the extensional viscosities have been calculated for the LDPEs according to both techniques and consequently compared with the SER steady state extensional viscosity data reported in the literature [10], [26] as visible in Figs. 26-31 (the shear viscosity data needed for extensional viscosity calculation has also been taken from these two references; corresponding Carreau-Yasuda model fitting parameters are provided in Tab. 3). Closer analysis of these Figures reveals the following conclusions.

Tab. 2. Parameters of the entrance pressure drop model (Eq. 16) for LDPEs and mLLDPEs

Material	$\eta_{ENT,0}$ (Pa.s)	$a'(-)$	$\lambda'(s)$	$\alpha'(s)$	$\xi'(-)$
LDPE Lupolen 1840H	17,123.981676	0.5908517882	0.0421690	4.074245	0.457389
LDPE Escorene LD165BW1	33,577.941877	0.4844595041	0.1091910	4.704289	0.310077
mLLDPE low	25,599.000000	0.5981200000	0.0129029	0.427290	0.000000
mLLDPE middle	7,863.024385	0.5873461851	0.0151370	3.203749	0.609419
mLLDPE high	7,722.100949	0.7351088581	0.0049170	2.091828	0.487700

Tab. 3. Parameters of Careau-Yasuda model (Eq. 3) for shear viscosity curves of LDPEs

Material	η_0 (Pa.s)	$\lambda(s)$	$a(-)$	$\bar{n}(-)$
LDPE Lupolen 1840H	59,950	1.5127000	0.38737	0.22245
LDPE Escorene LD165BW1	77,092	3.8285000	0.31350	0.29042

Firstly, steady state extensional viscosity data from the entrance pressure drop techniques shows strain hardening behavior for both LDPE melts but, on the other hand, the level of the stain hardening is lower compared to the SER data.

Secondly, the Binding method give slightly better agreement with the SER data than the Cogswell model at low extensional strain rates whereas at higher extensional rates, the Cogswell model gives better agreement with the SER data compared the Binding one. With the aim to take this finding into account, the SER data were compared with Binding's and Cogswell's extensional viscosity data at low and high extensional rates, respectively, as visible in Figs. 28 and 31. It is clear, that even if both techniques are combined together, the extensional viscosity data (in the strain hardening region) from the entrance pressure drop are still lower compared to SER data.

Finally, the inspection of Figs. 26-27 and Figs. 29-30 for LDPE Escorene and LDPE Lupolen, respectively, reveals that application of the effective entry length correction is crucially important to get relatively close agreement with the SER data.

Comparison between corrected entrance pressure drop techniques and SER for mLLDPEs with different level of long chain branching

In the first step, transient extensional rheology of the linear (mLLDPE Low) and branched (mLLDPE middle, mLLDPE high) materials were evaluated on the SER at 140°C as visible in Fig. 32. It clearly visible that an increase in the level of the long chain branching lead to increase in the extensional strain hardening.

In the second step, the steady extensional viscosities for all three samples were determined from the entrance viscosity measurements (Figs. 33-35) which were consequently compared with SER steady state extensional viscosity data. This comparison is provided in Figs. 36-44. Note the procedure for the determination of the extensional viscosity data from the measured entrance viscosities was the same as for the LDPEs and the fitting parameters of Eq. (16) are provided in Tab. 2. It should also be pointed out that the steady state extensional viscosity data were taken from the peaks appearing on the transient viscosity curves for corresponding extensional strain rates. This is due to the fact that beyond the maximum the elongated sample may become unstable to free surface perturbations that grow and cause a necking onset of the sample followed by a complete rupture. Closer analysis of the Figs. 36-44 reveals that corrected Cogswell and Binding models give very good agreement with steady SER extensional viscosity data for all three samples even if their predictions at low and high extensional rates quite different.

Experimental determination of complex viscosity and elastic compliance for mLLDPEs with different level of long chain branching

The comparison between frequency dependent complex viscosity (calculated from measured loss and storage modules – Tab. 4) for all three samples is given in Fig. 45. Clearly, the increase in the long chain branching slightly increases the Newtonian viscosity, however, at higher shear rates the viscosity for all three materials becomes almost identical. Particular values of the Newtonian viscosities and activation energies for all three samples are provided in Tab. 5.

In Fig. 46, much higher difference between all three materials can be visible from the measured frequency dependent elastic compliance point of view. It shows that elastic

compliance (defined here as $\frac{G'}{\eta^* \omega}$) increases with increasing level of long chain branching especially at low frequencies, which is in agreement with the open literature [14].

Tab. 4. Measured loss and storage modules for investigated mLLDPEs at 140°C

Material								
mLLDPE low			mLLDPE middle			mLLDPE high		
ω (rad.s ⁻¹)	G' (Pa)	G'' (Pa)	ω (rad.s ⁻¹)	G' (Pa)	G'' (Pa)	ω (rad.s ⁻¹)	G' (Pa)	G'' (Pa)
10 ⁻¹	11.334	1,732.8	10 ⁻¹	44.032	1,876.6	10 ⁻¹	86.439	1,955.4
10 ^{-0.8}	39.414	2,730.4	10 ^{-0.8}	99.184	2,940.6	10 ^{-0.8}	163.00	3,044.1
10 ^{-0.6}	131.05	4,284.5	10 ^{-0.6}	208.79	4,589.4	10 ^{-0.6}	320.01	4,737.9
10 ^{-0.4}	302.38	6,711.9	10 ^{-0.4}	428.94	7,154.4	10 ^{-0.4}	607.87	7,332.7
10 ^{-0.2}	695.64	10,483	10 ^{-0.2}	933.8	11,100	10 ^{-0.2}	1,191.3	11,290
10 ⁰	1,584.5	16,244	10 ⁰	1,926.2	17,127	10 ⁰	2,314.3	17,272
10 ^{0.2}	3,387.7	24,920	10 ^{0.2}	3,981.5	26,127	10 ^{0.2}	4,475.0	26,180
10 ^{0.4}	6,984.4	37,525	10 ^{0.4}	7,931.2	39,180	10 ^{0.4}	8,556.8	38,997
10 ^{0.6}	13,782	55,446	10 ^{0.6}	15,188	57,577	10 ^{0.6}	15,932	57,016
10 ^{0.8}	25,744	79,622	10 ^{0.8}	27,842	82,292	10 ^{0.8}	28,488	81,219
10 ¹	45,605	111,000	10 ¹	48,626	114,000	10 ¹	48,993	112,000
10 ^{1.2}	76,520	149,000	10 ^{1.2}	80,673	153,000	10 ^{1.2}	80,391	150,000
10 ^{1.4}	121,000	193,000	10 ^{1.4}	127,000	197,000	10 ^{1.4}	126,000	194,000
10 ^{1.6}	183,000	240,000	10 ^{1.6}	190,000	244,000	10 ^{1.6}	187,000	240,000
10 ^{1.8}	263,000	286,000	10 ^{1.8}	271,000	290,000	10 ^{1.8}	266,000	285,000
10 ²	360,000	325,000	10 ²	369,000	329,000	10 ²	363,000	324,000

Tab. 5. Newtonian viscosity (determined at 140°C) and activation energy for mLLDPEs

Material	η_0 (Pa.s)	E_a (kJ/mol)
mLLDPE low	17,620	22.708
mLLDPE middle	18,990	26.411
mLLDPE high	19,780	24.731

Quantification of the extensional strain hardening level for mLLDPE samples

Generalized Newtonian (Eq. 2) and Maxwell (Eq. 7) models were used to fit the steady state extensional viscosity data for all three tested mLLDPE melts. For such purpose, corrected Cogswell extensional viscosity data were employed. The comparison between measured and predicted steady extensional viscosity curves for all three samples is depicted in Fig. 47 and the model parameters are provided in Tab. 6. As visible, both models have reasonably good capability to describe all mLLDPEs (except of extensional strain hardening under-predictions for highly branched mLLDPE). As visible from Tab. 6, generalized Newtonian and generalized Maxwell models have capability to quantify the long chain branching level through parameters K_1/λ_0 and α , respectively, i.e. both parameters increases with increasing level of long chain branching of mLLDPEs.

Tab. 6. Function parameters of used constitutive equation for mLLDPE shear and extensional rheology description

Function	Carreau-Yasuda (Eq. 3)				Zatloukal et al. (Eq. 5)		Barnes-Roberts (Eq. 8)	
Material	η_0 (Pa.s)	λ (s)	a (-)	\bar{n} (-)	α (s)	ζ (-)	λ_0 (s)	K_1/λ_0 (-)
mLLDPE low	17,620	0.0415668	0.76966	0.28329	0.000150	0.565997	0.002768	1.582772
mLLDPE middle	18,990	0.0385936	0.71953	0.25160	8.035667	0.242168	41.463	1.596122
mLLDPE high	19,780	0.0370526	0.66402	0.23780	14.614299	0.266867	13.468	1.637437

The processibility evaluation of mLLDPE samples with respect to shark skin and gross melt fracture

Capillary rheometer equipped with long dies ($L/D = 16$) and orifice die ($L/D = 0$) having 1 mm die diameter has been employed to produce the extrudates at wide range of apparent shear rates (from 61 s^{-1} up to 2300 s^{-1}) at 140°C with the purpose to determine the onset of the shark skin and gross melt fracture phenomena for all three tested mLLDPE. With the aim to clarify meaning of these surface/bulk defects for mLLDPEs, the Figs. 48a-48c is provided here to show how these defects change the extrudate shape. For onset determination of these phenomena, extrudate cuts (Figs. 48d-48f) and external surface analysis of all extrudates (Figs. 49-56) has been performed. Critical apparent shear rates for the shark skin and gross melt fracture onset for all mLLDPE materials are provided in Tab. 7. Definition of stable, stable-unstable and unstable flow conditions for

linear mLLDPE (low) and highly branched mLLDPE (high) is given in Fig. 55 and Fig. 56, respectively.

Tab. 7. Capillary flow stability flow evaluation for mLLDPE samples

	Material					
	mLLDPE low		mLLDPE middle		mLLDPE high	
	Type of capillary die					
	long $\dot{\gamma}$ (s ⁻¹)	orifice $\dot{\gamma}$ (s ⁻¹)	long $\dot{\gamma}$ (s ⁻¹)	orifice $\dot{\gamma}$ (s ⁻¹)	long $\dot{\gamma}$ (s ⁻¹)	orifice $\dot{\gamma}$ (s ⁻¹)
<i>Unstable flow</i>	432	247	570	247	432	187
<i>Stable - unstable flow</i>	375	215	496	215	375	163
<i>Melt rupture</i>		754		496		496

If the result from the long die ($L/D = 16$, $D = 1$ mm) are analyzed, we can observe that low level of long chain branching can postpone the shark skin onset from 432 s^{-1} up to 570 s^{-1} (with comparison to shark skin onset for linear mLLDPE). However, for highly branched sample, the shark skin onset is the same as for the linear mLLDPE. This behaviour can be explained by the help of measured shear stress level measured on the high shear rate (Fig. 57). Clearly, shear stress reduction occurs for slightly branched mLLDPE (middle) only. No stabilization effect of highly branched mLLDPE (high) can be explained by the significant increase of the elasticity and extensional viscosity as depicted in Fig. 46 and 47, respectively. These conclusions are also supported from the results collected from the orifice die ($L/D = 0$) measurements, also summarized in Tab. 7. In this case, low level of long chain branching (mLLDPE middle) has no effect on the shark skin onset however, for highly branched mLLDPE (mLLDPE high), the shark skin occur at even smaller apparent shear rates compare to linear and slightly branched mLLDPE. To understand this behaviour, we should keep in mind that the orifice die generates the flow conditions where melt memory (influenced by elasticity and extensional viscosity) plays very important role, because the die has no any length to allow relaxation of the stresses generated at the die entry region. In the other word, predominantly melt elasticity level rather than shear viscosity is the main factor determining the flow stability in this case. From this point of view, it can be said that significant increase in the long chain branching increases the elasticity level, which causes easier development of the shark skin phe-

nomenon in the flow through orifice die. This is also in good agreement with the obtained melt rupture onset data provided in Tab. 7 where it is shown that increase in the long chain branching does not postpone this phenomena, i.e. the ‘LDPE’ like behaviour can be visible here for the branched mLLDPEs.

The above findings suggest that there exist optimum value of the long chain branching in the mLLDPE structure which can improve the processing window of these materials.

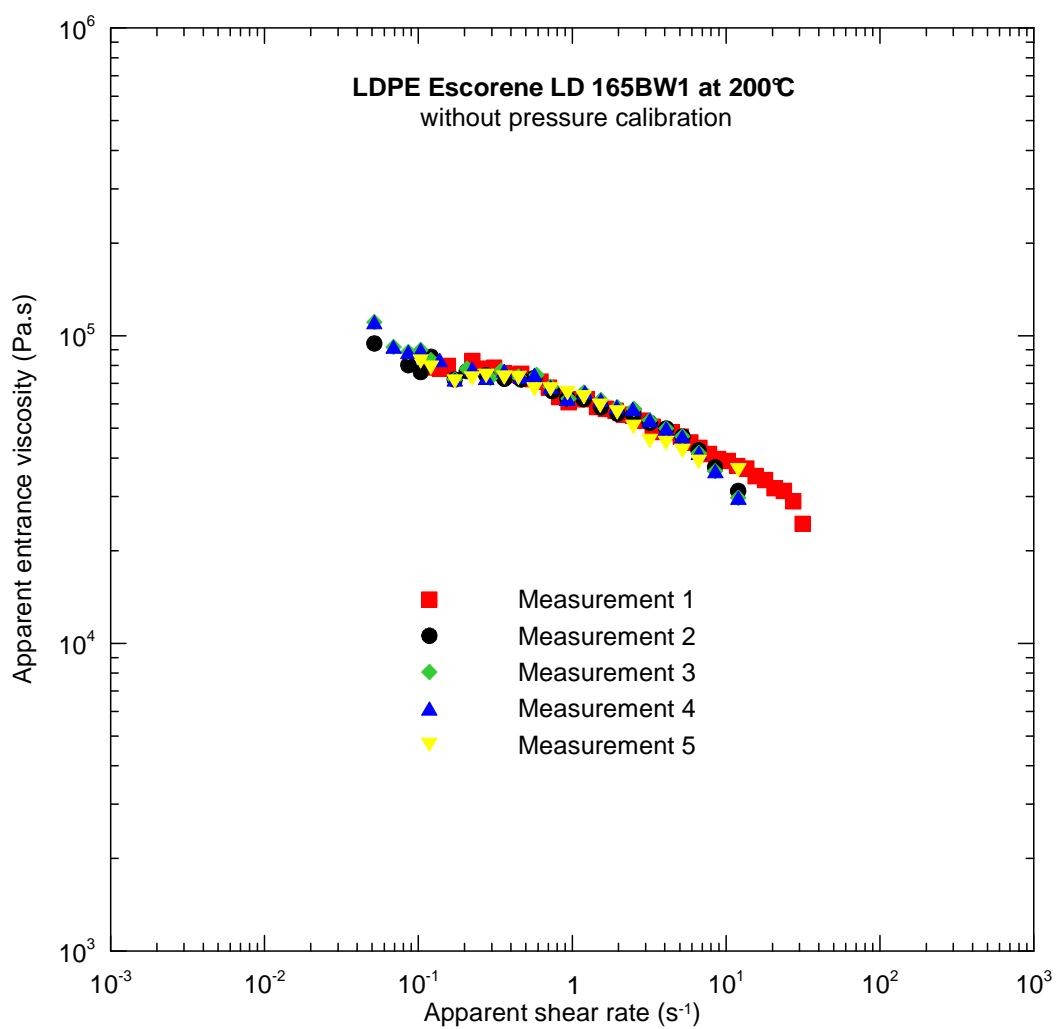


Fig. 23. Five times repeated measurements of the entrance viscosity for LDPE Escorene material with no pressure calibration between the measurements at 200°C

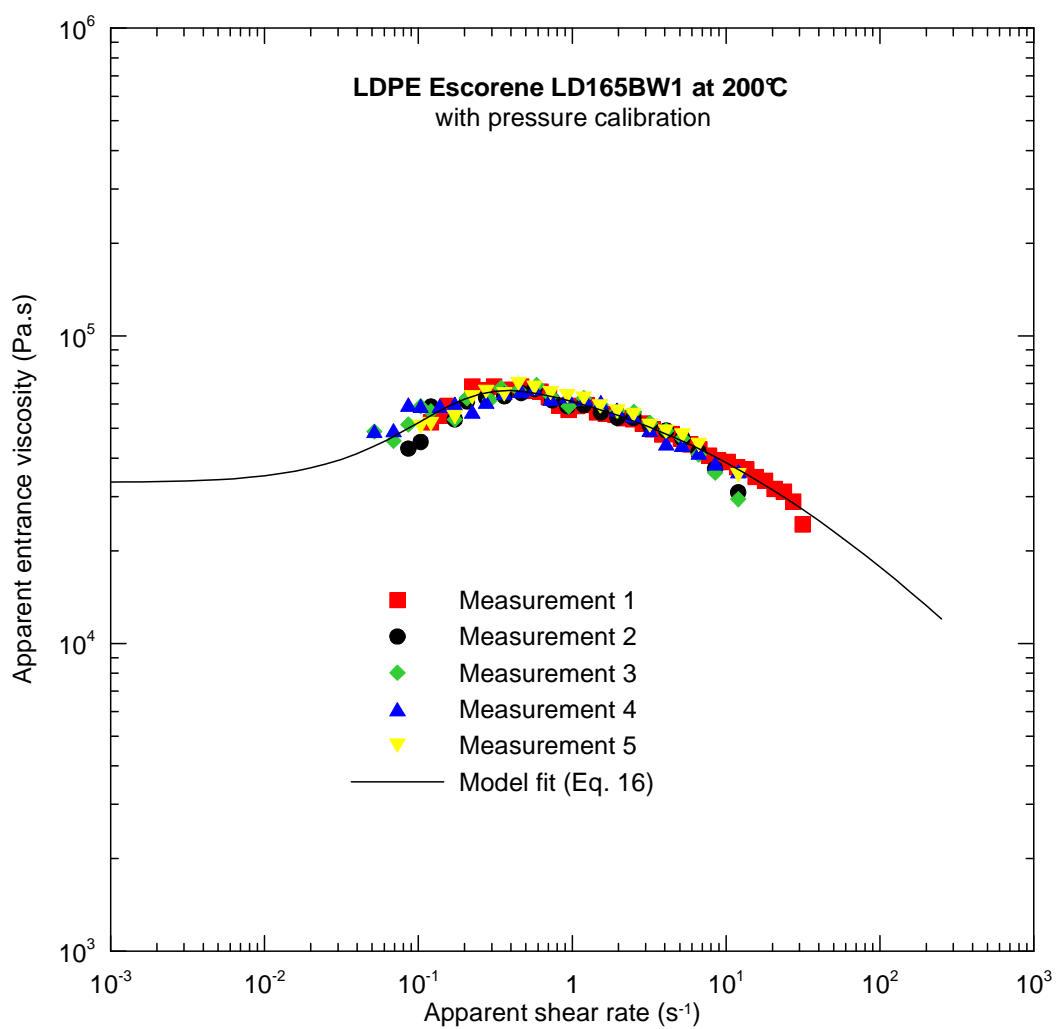


Fig. 24. Five times repeated measurements of the entrance viscosity for LDPE Escorene material with pressure calibration made between the measurements at 200°C. The solid line represents the entrance viscosity model fit (Eq. 16)

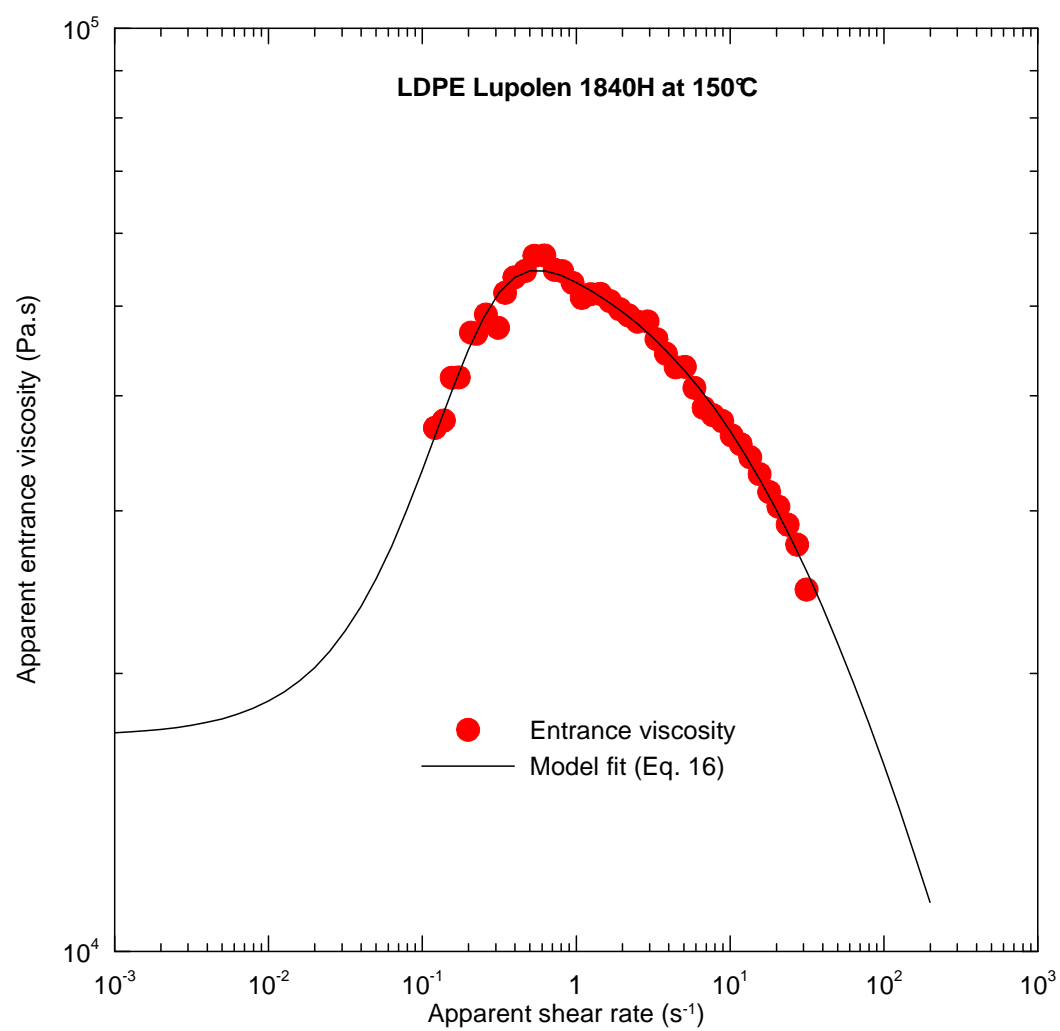


Fig. 25. Entrance viscosity for LDPE Lupolen material 150°C with applied pressure calibration. The solid line represents the entrance viscosity model fit (Eq. 16)

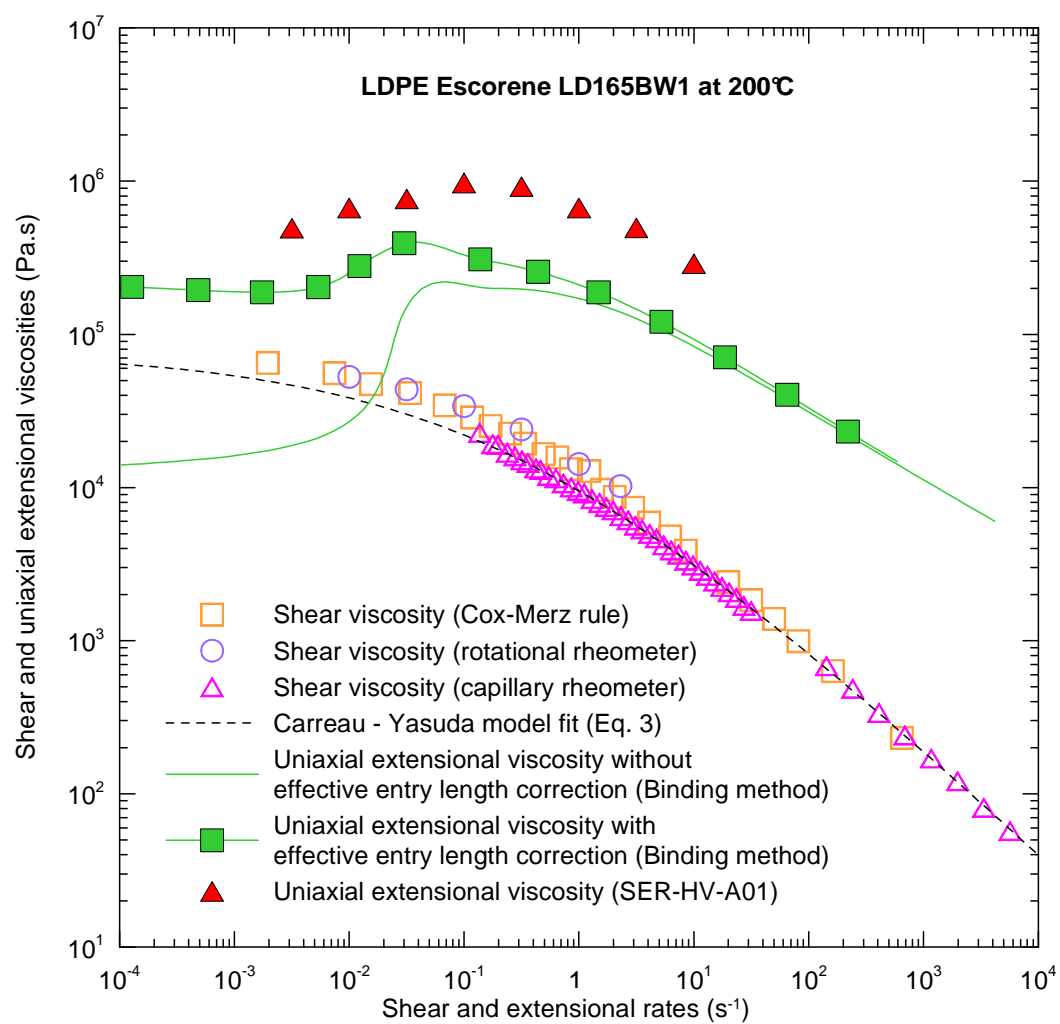


Fig. 26. Comparison between uncorrected/corrected Binding extensional viscosity data and SER measurements for LDPE Escorene at 200°C. Shear viscosity data obtained from rotational and capillary rheometer are also provided in this Figure

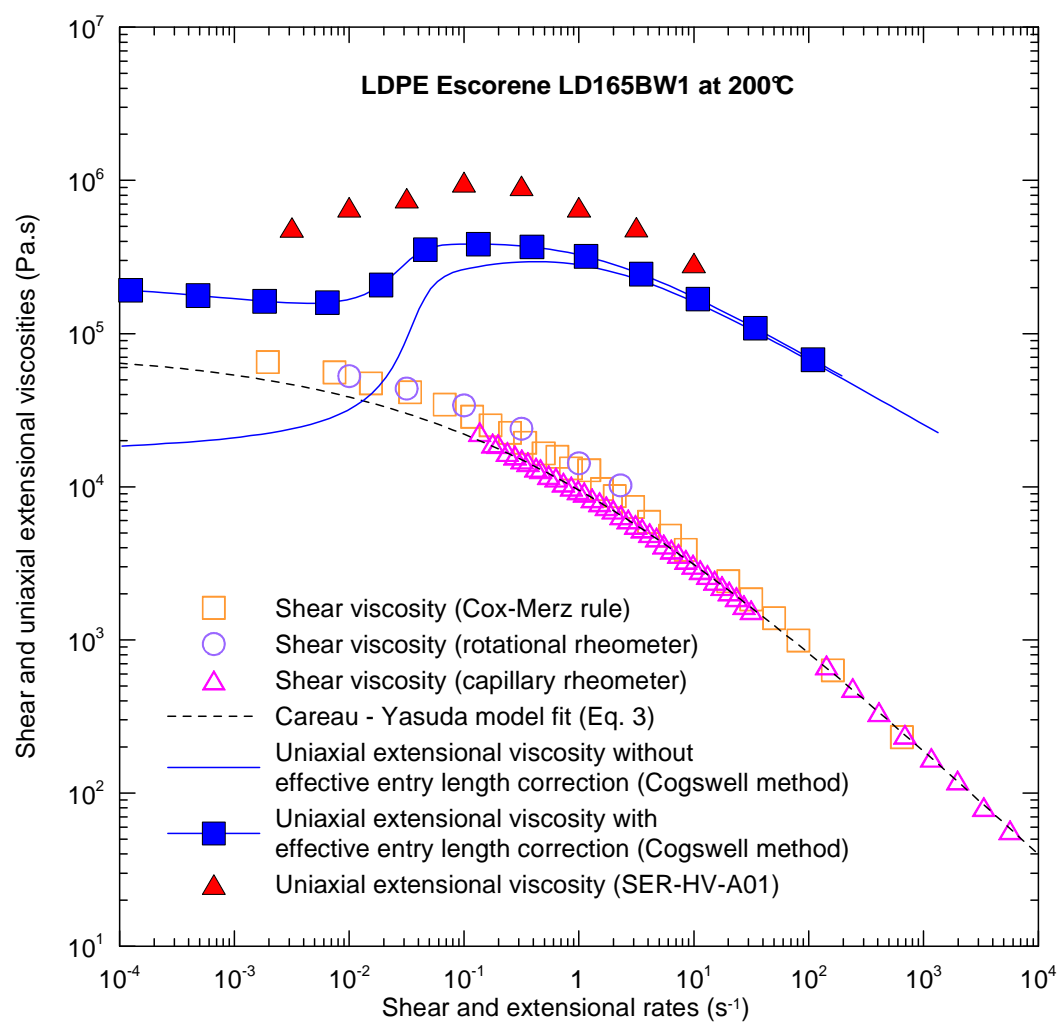


Fig. 27. Comparison between uncorrected/corrected Cogswell extensional viscosity data and SER measurements for LDPE Escorene at 200°C. Shear viscosity data obtained from rotational and capillary rheometer are also provided in this Figure

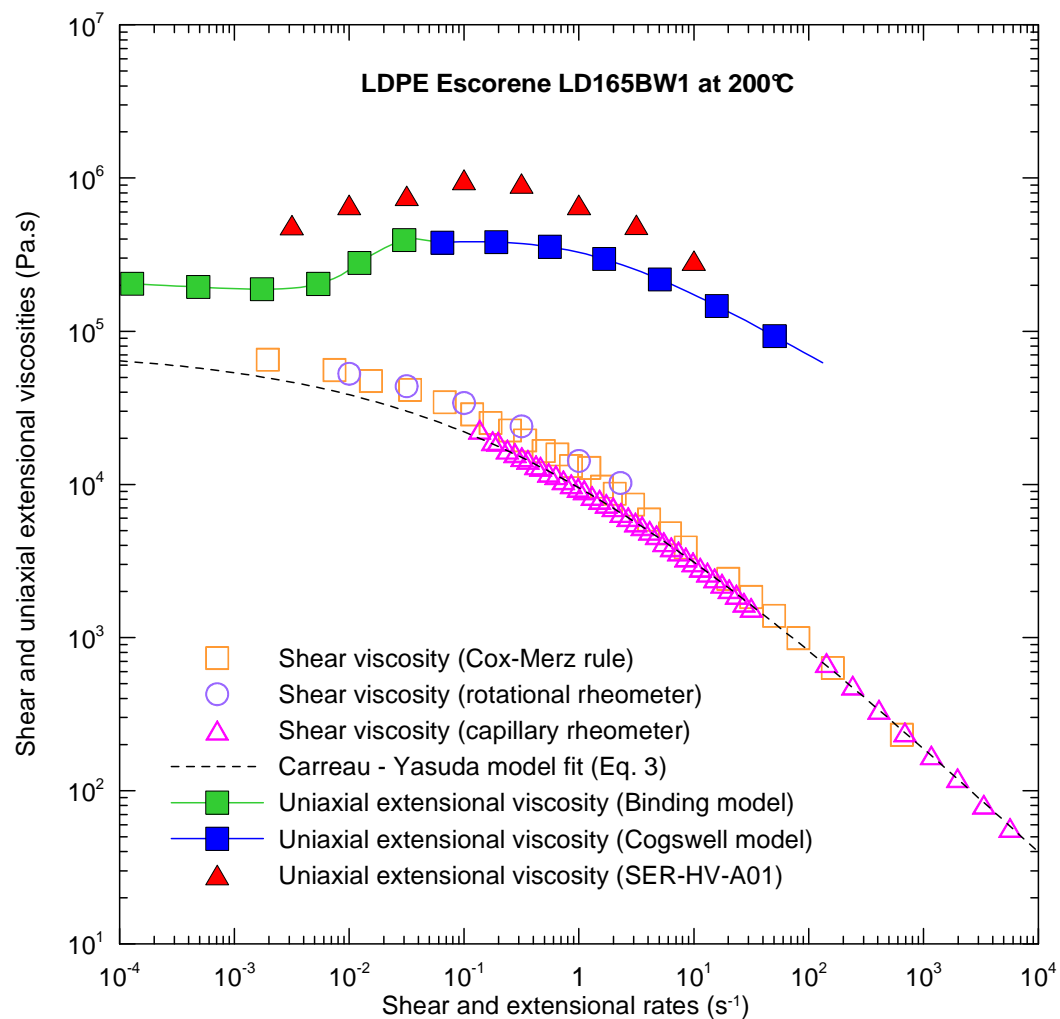


Fig. 28. Comparison between uncorrected/corrected Binding (low extensional rate range), Cogswell (high extensional rate range) extensional viscosity data and SER measurements for LDPE Escorene at 200°C. Shear viscosity data obtained from rotational and capillary rheometer are also provided in this Figure

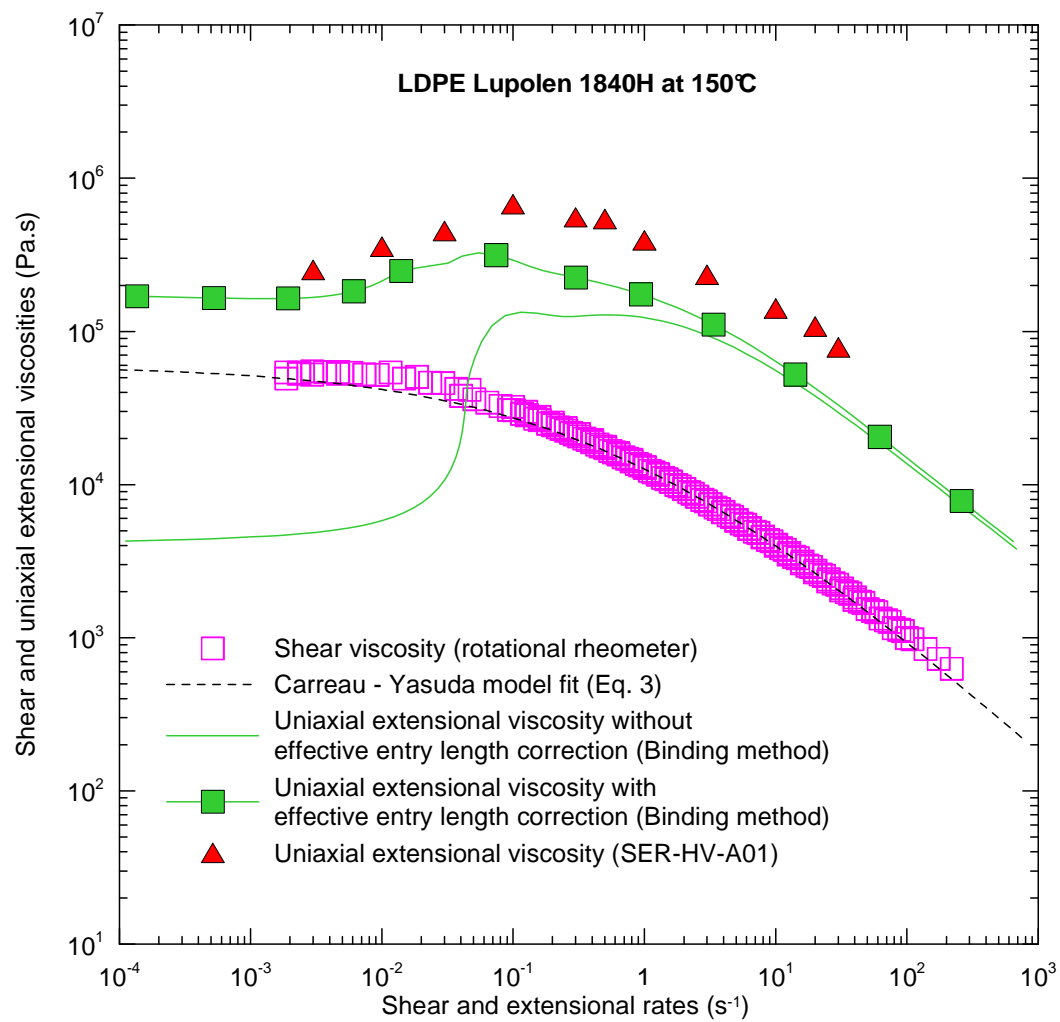


Fig. 29. Comparison between uncorrected/corrected Binding extensional viscosity data and SER measurements for LDPE Lupolen at 150°C. Shear viscosity data obtained from rotational rheometer are also provided in this Figure

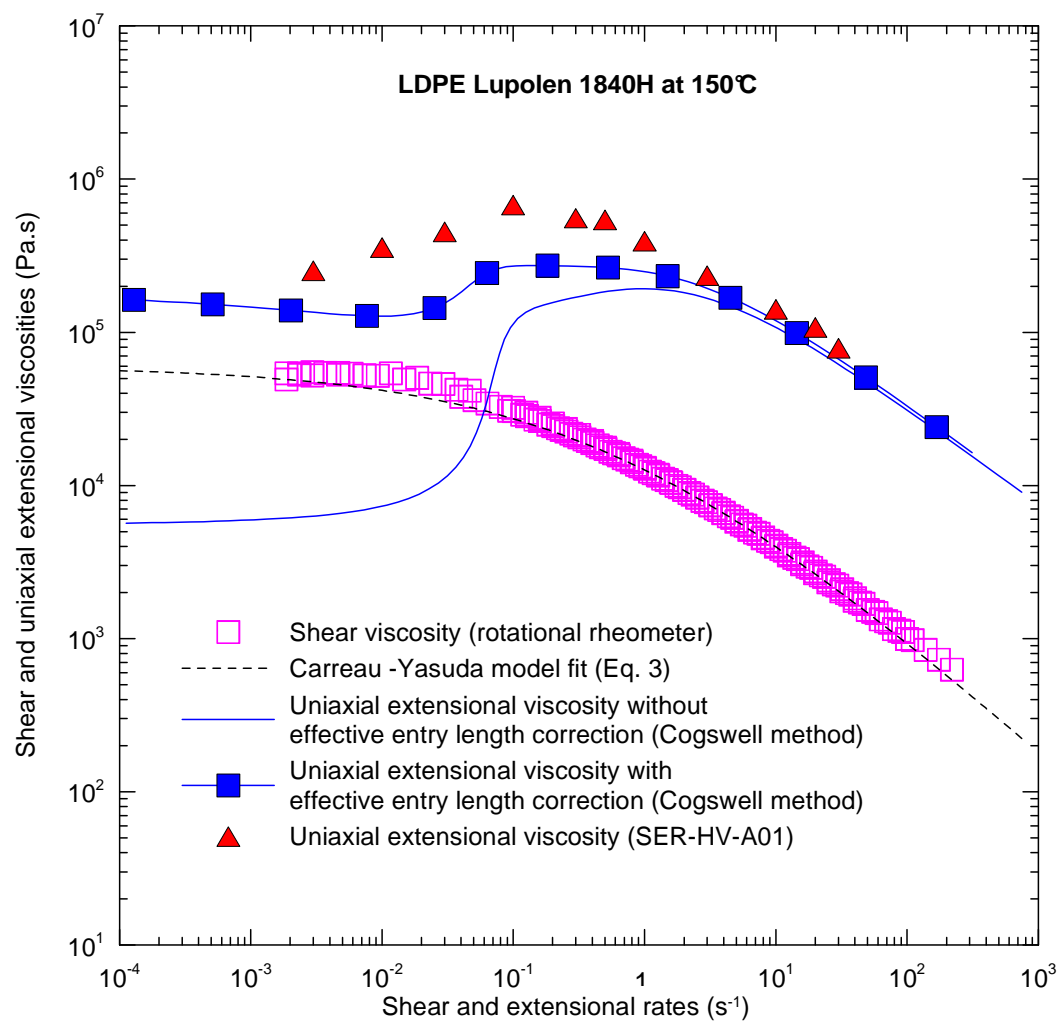


Fig. 30. Comparison between uncorrected/corrected Cogswell extensional viscosity data and SER measurements for LDPE Lupolen at 150°C. Shear viscosity data obtained from rotational rheometer are also provided in this Figure

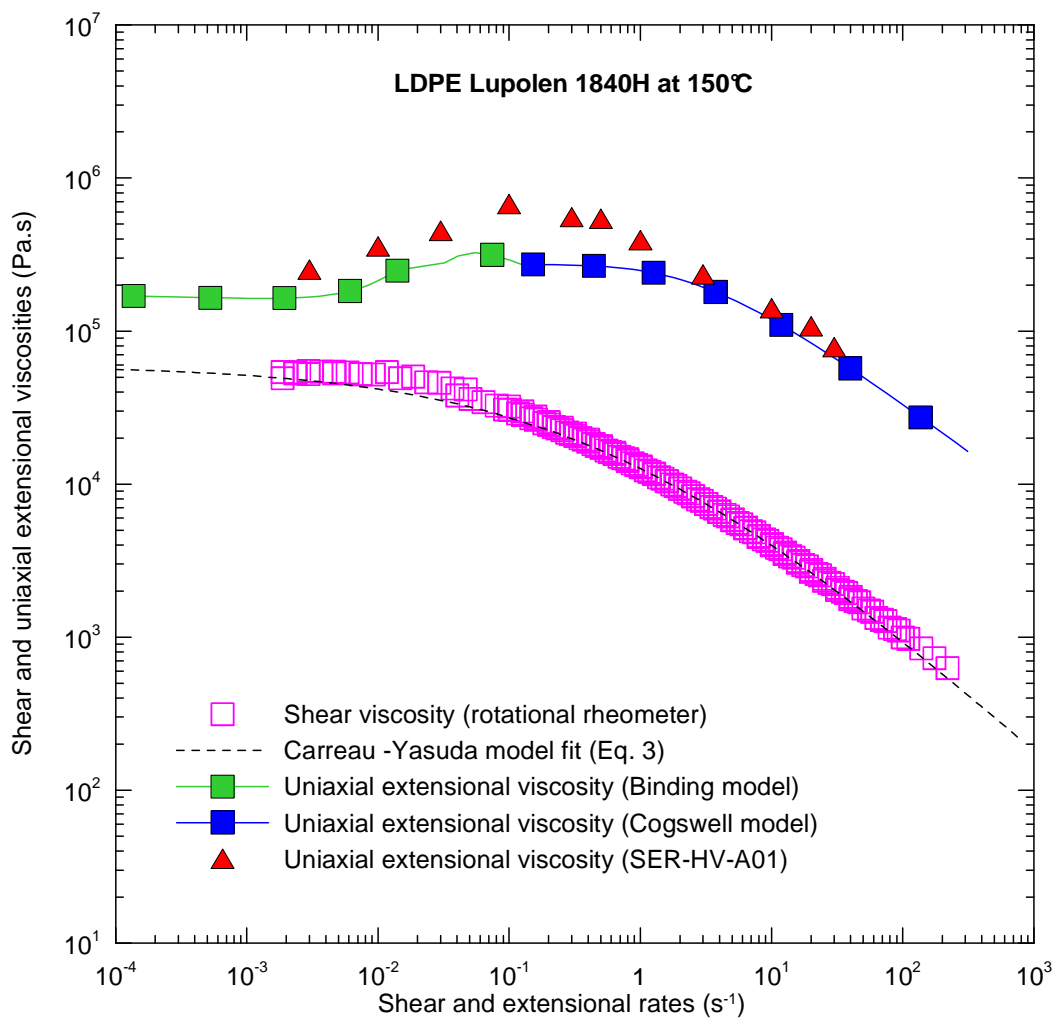


Fig. 31. Comparison between uncorrected/corrected Binding (low extensional rate range), Cogswell (high extensional rate range) extensional viscosity data and SER measurements for LDPE Lupolen at 150°C. Shear viscosity data obtained from rotational rheometer are also provided in this Figure

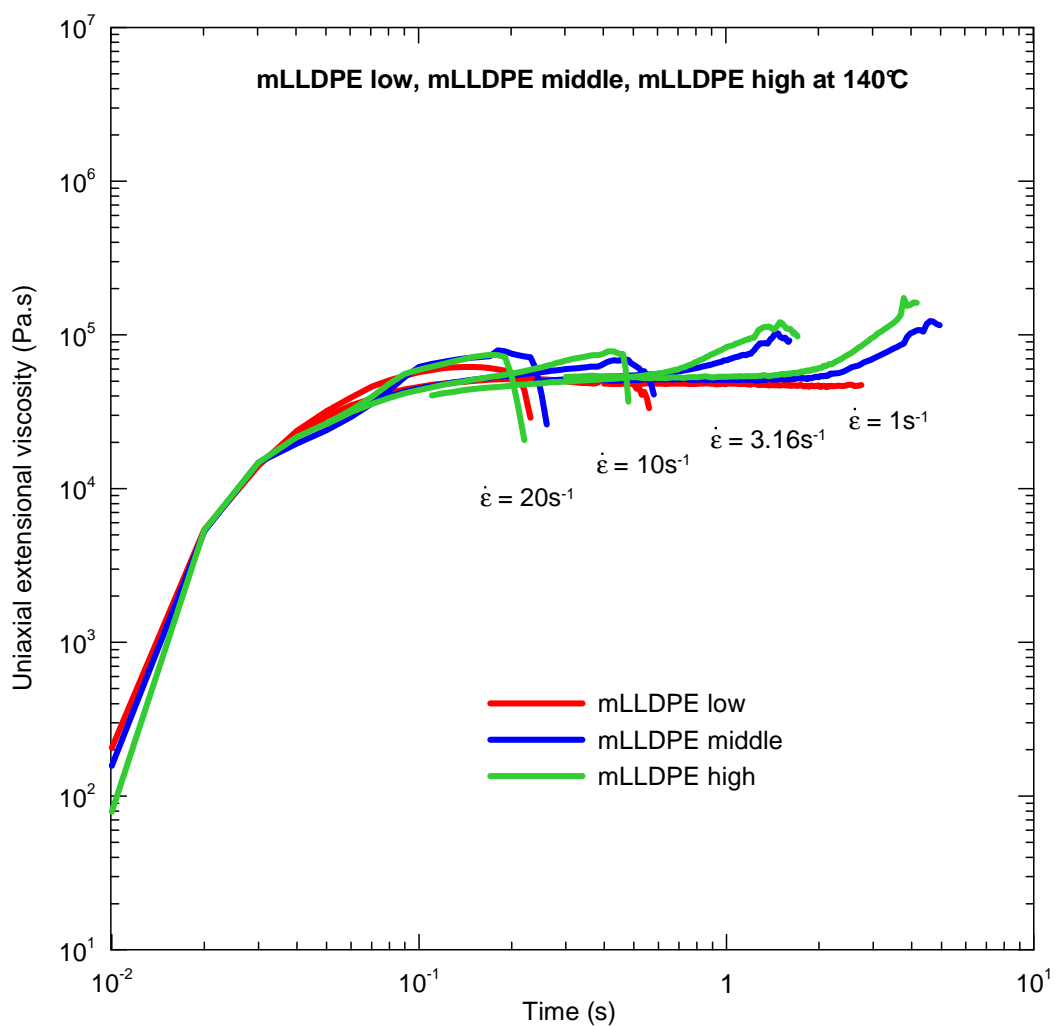


Fig. 32. Transient uniaxial extensional viscosity data for three mLLDPEs having different level of long chain branching obtained by SER at 140°C

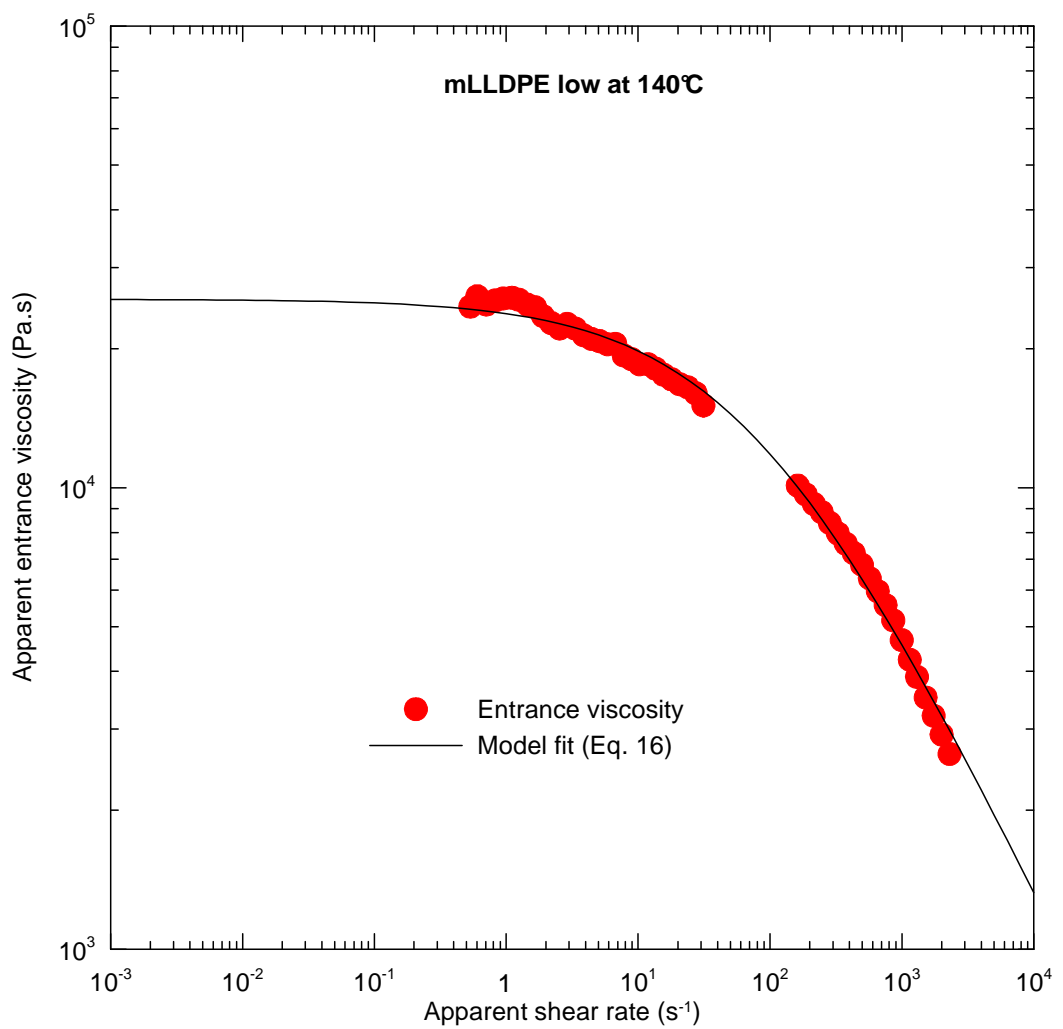


Fig. 33. Entrance viscosity for linear mLLDPE (low) at 140°C with applied pressure calibration. The solid line represents the entrance viscosity model fit (Eq. 16)

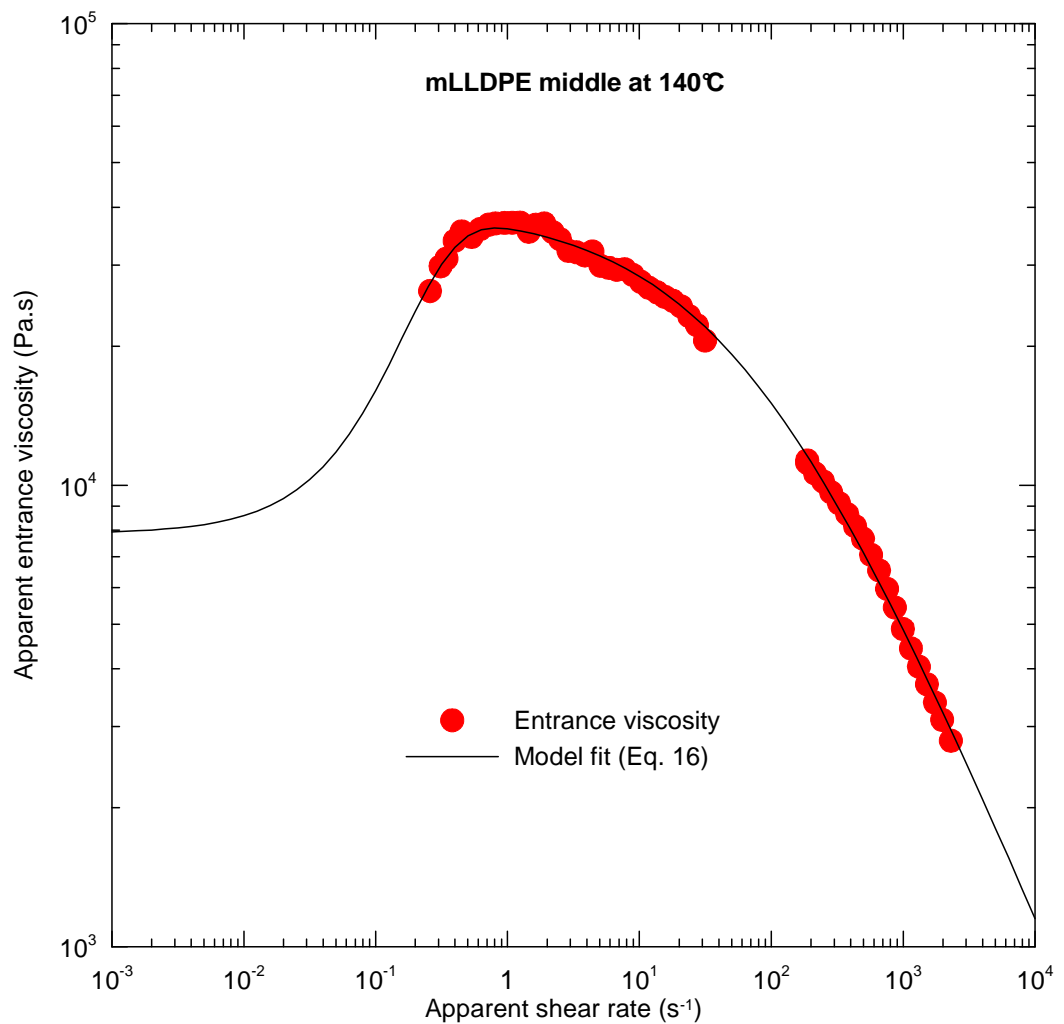


Fig. 34. Entrance viscosity for slightly branched mLLDPE (middle) at 140°C with applied pressure calibration. The solid line represents the entrance viscosity model fit (Eq. 16)

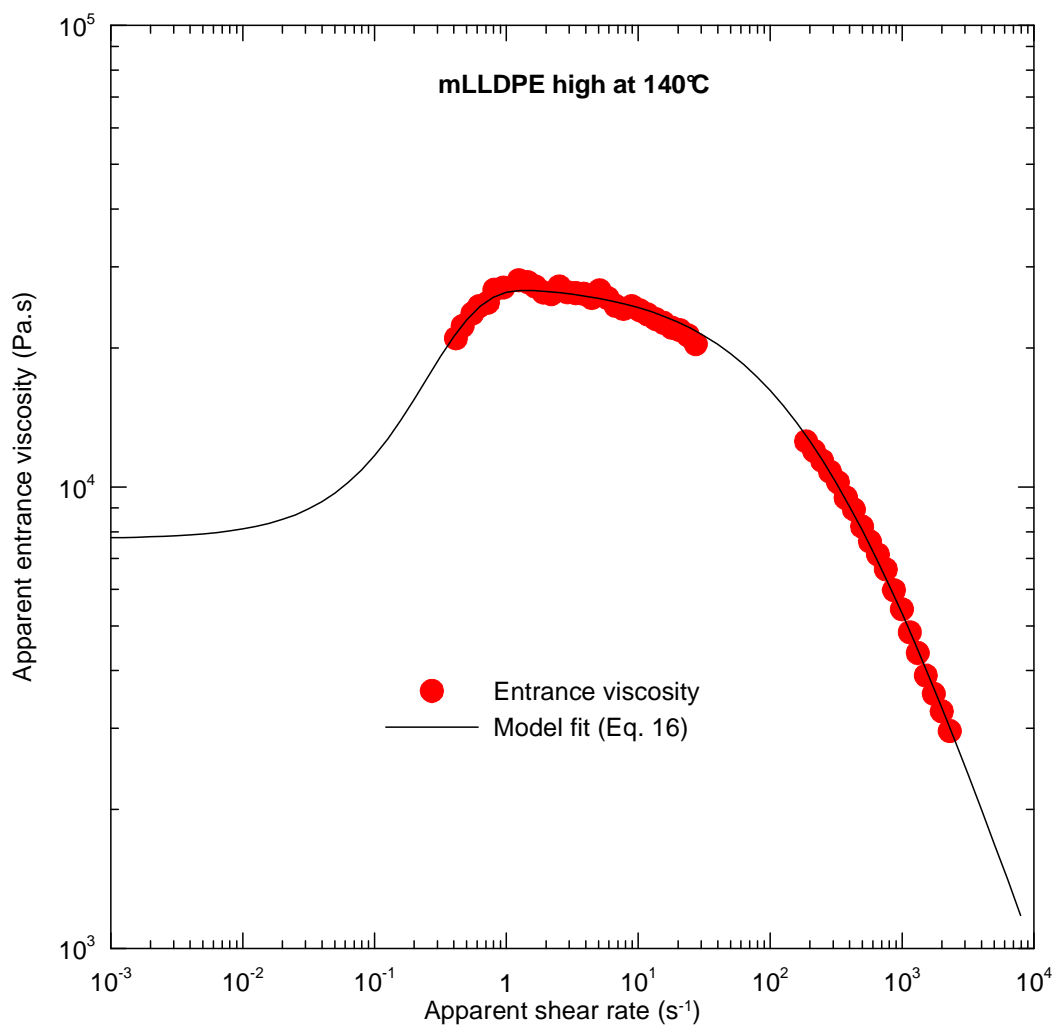


Fig. 35. Entrance viscosity for highly branched mLLDPE (high) at 140°C with applied pressure calibration. The solid line represents the entrance viscosity model fit (Eq. 16)

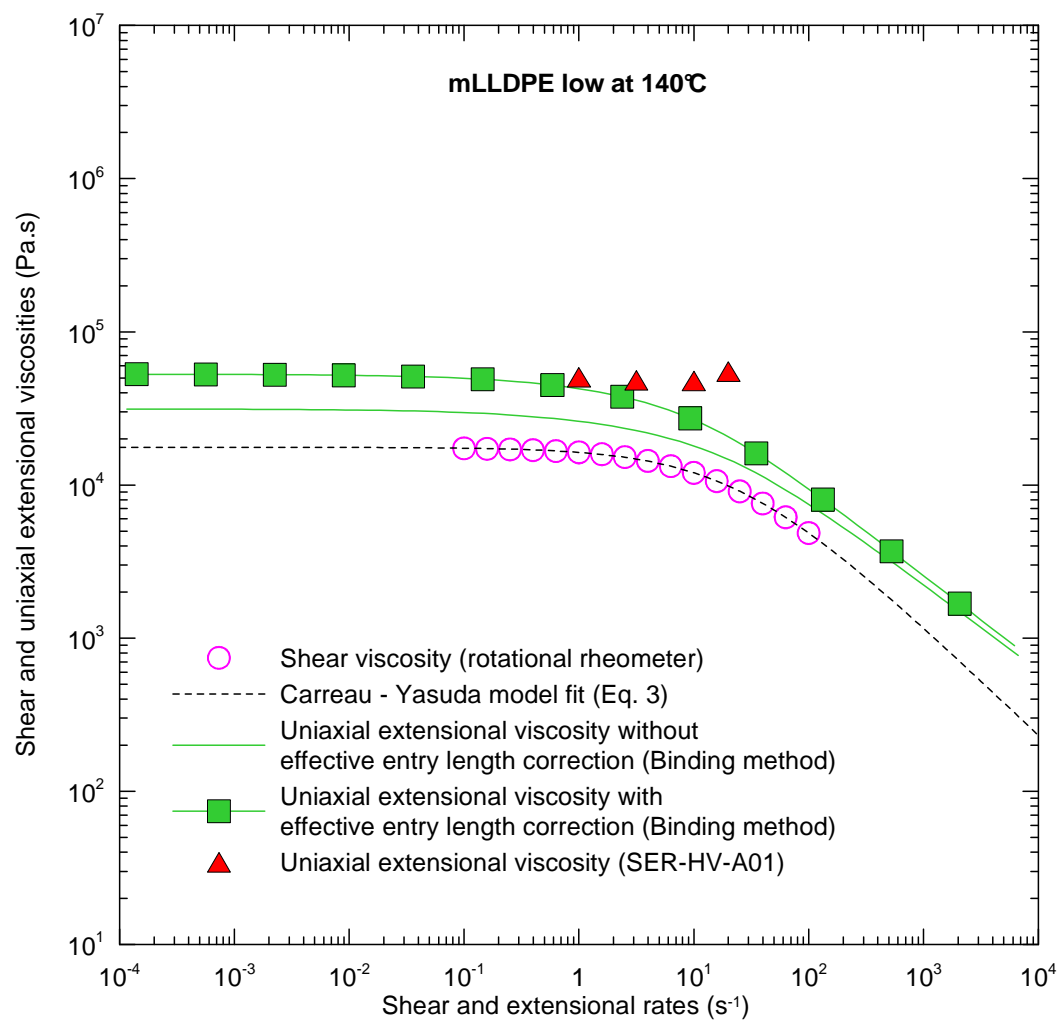


Fig. 36. Comparison between uncorrected/corrected Binding extensional viscosity data and SER measurements for linear mLLDPE (low) at 140°C. Shear viscosity data obtained from rotational rheometer are also provided in this Figure

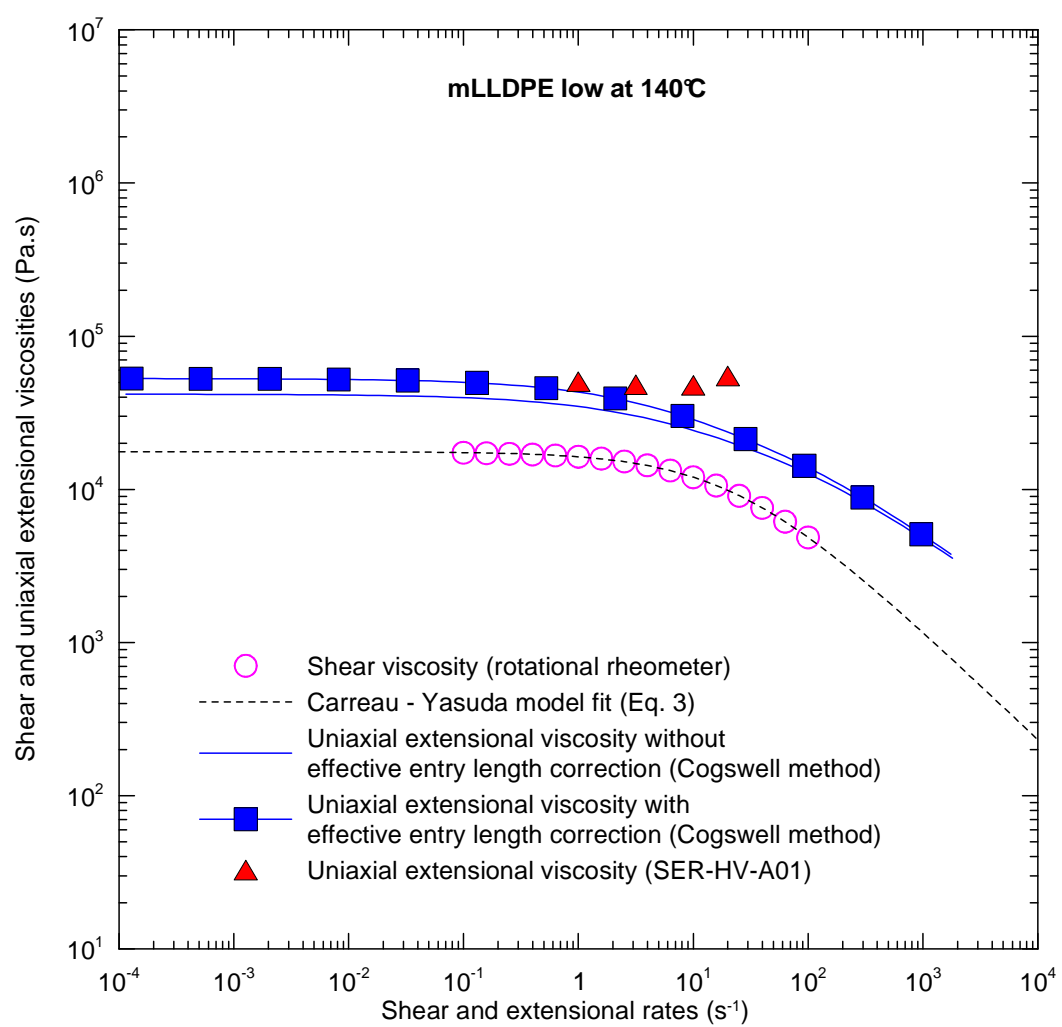


Fig. 37. Comparison between uncorrected/corrected Cogswell extensional viscosity data and SER measurements for linear mLLDPE (low) at 140°C. Shear viscosity data obtained from rotational rheometer are also provided in this Figure

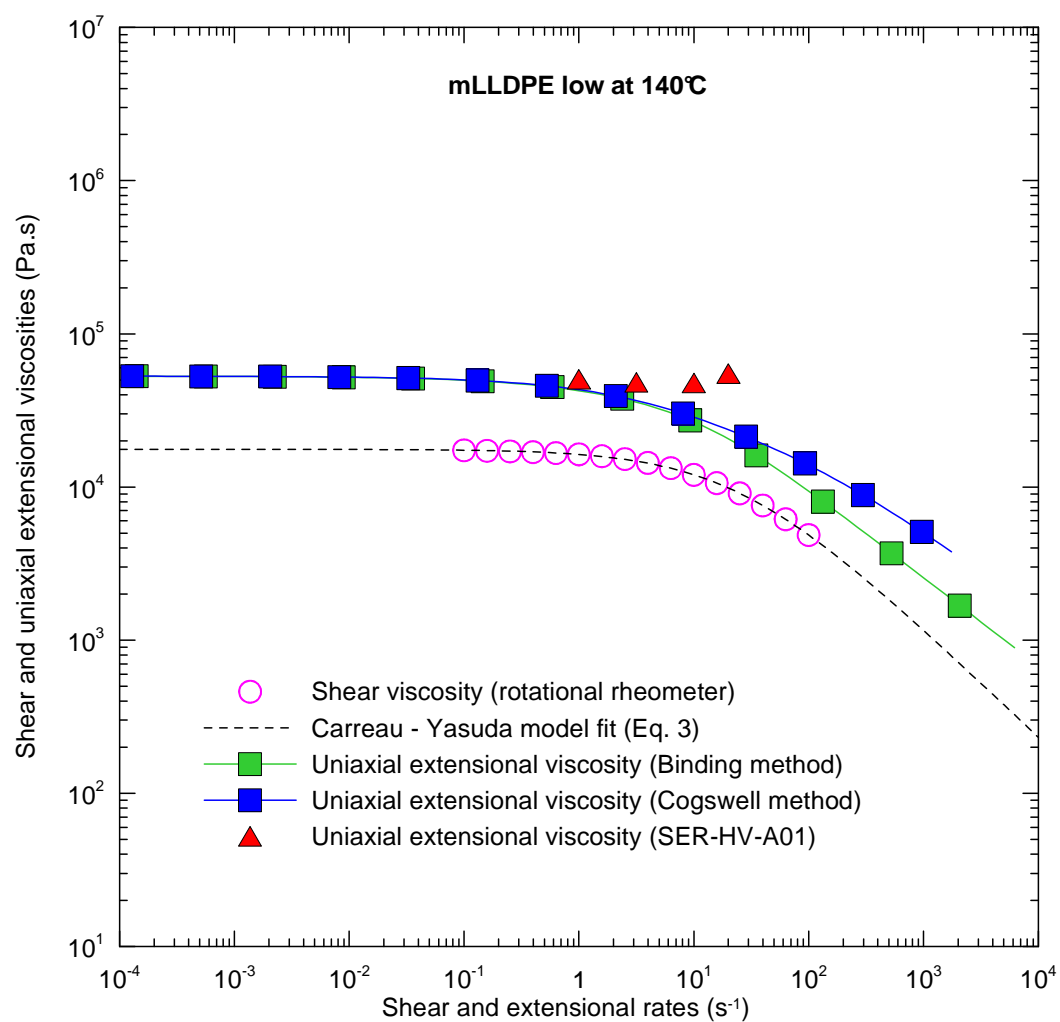


Fig. 38. Comparison between uncorrected/corrected Binding, Cogswell extensional viscosity data and SER measurements for linear mLLDPE (low) at 140°C. Shear viscosity data obtained from rotational rheometer are also provided in this Figure

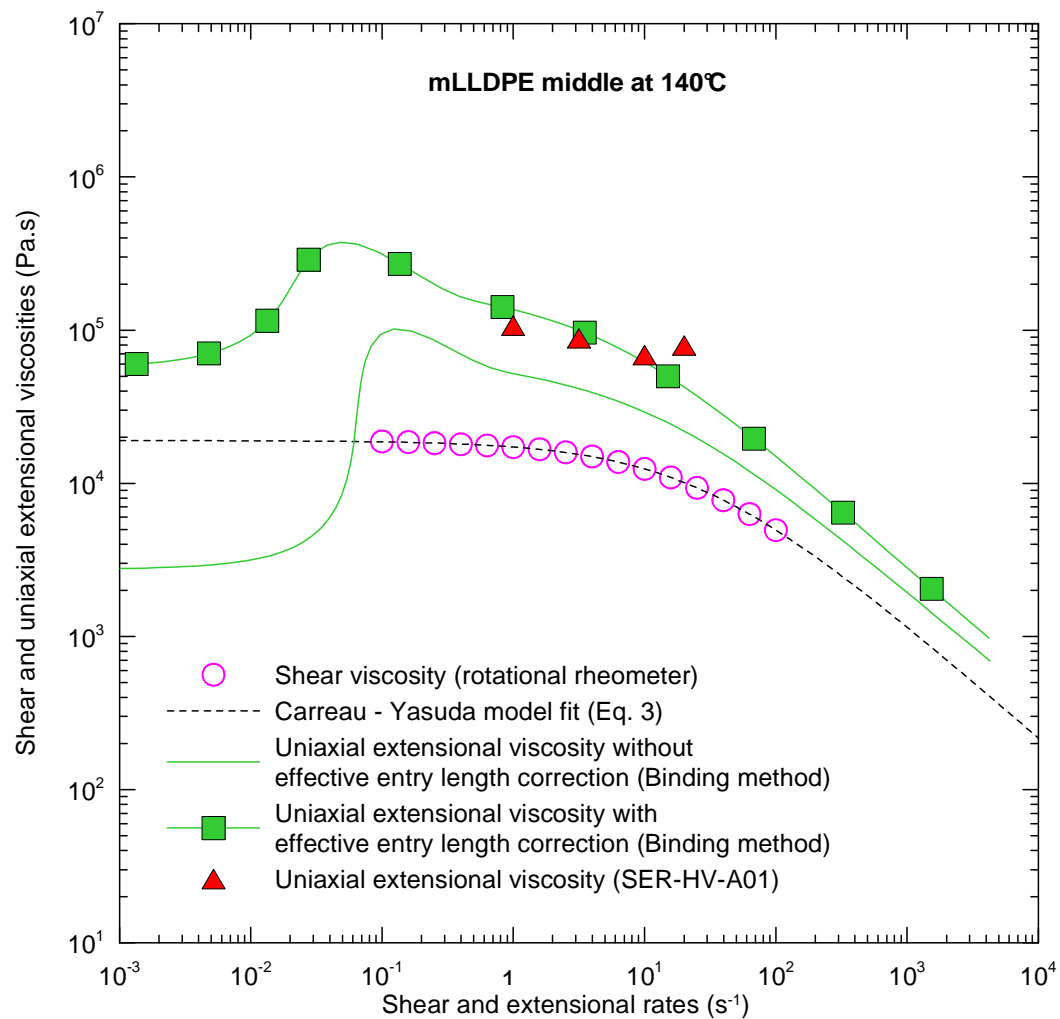


Fig. 39. Comparison between uncorrected/corrected Binding extensional viscosity data and SER measurements for slightly branched mLLDPE (middle) at 140°C. Shear viscosity data obtained from rotational rheometer are also provided in this Figure

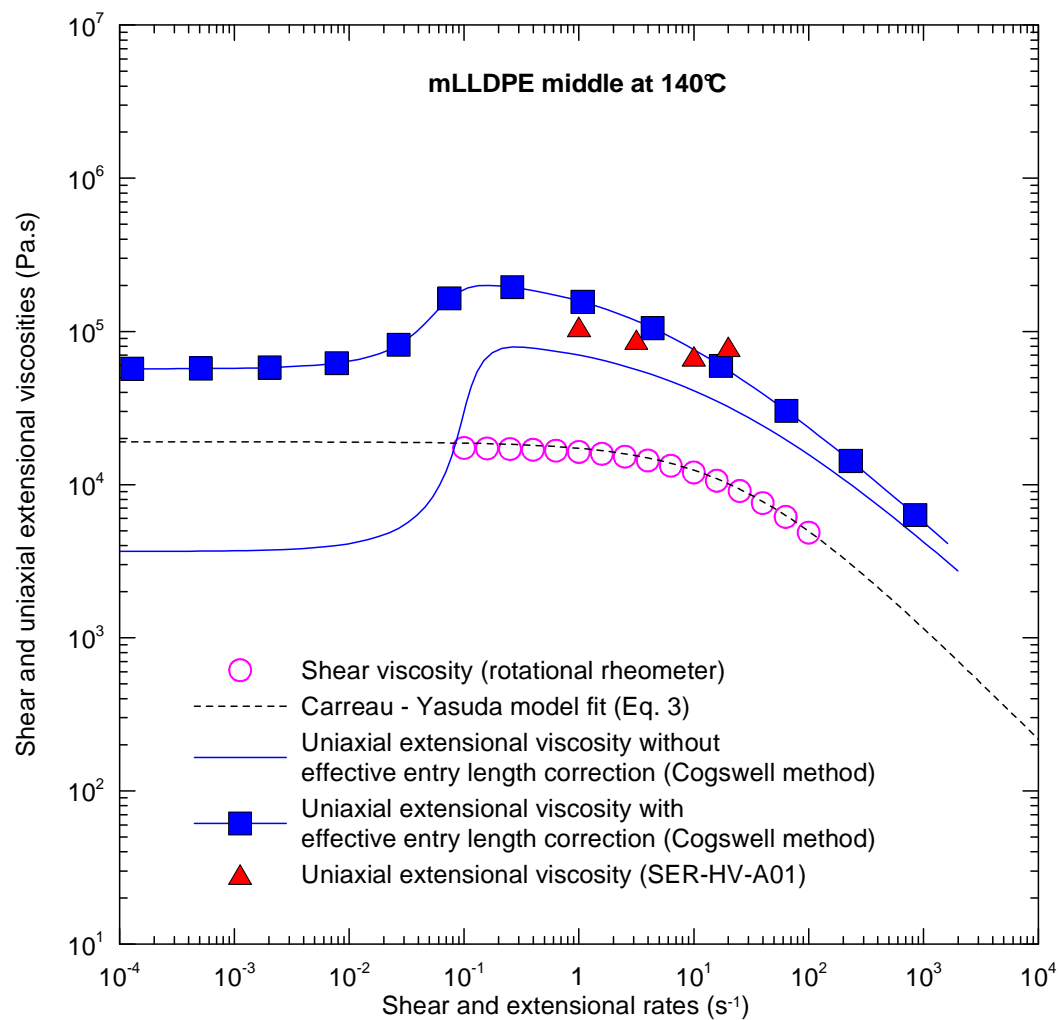


Fig. 40. Comparison between uncorrected/corrected Cogswell extensional viscosity data and SER measurements for slightly branched mLLDPE (middle) at 140°C. Shear viscosity data obtained from rotational rheometer are also provided in this Figure

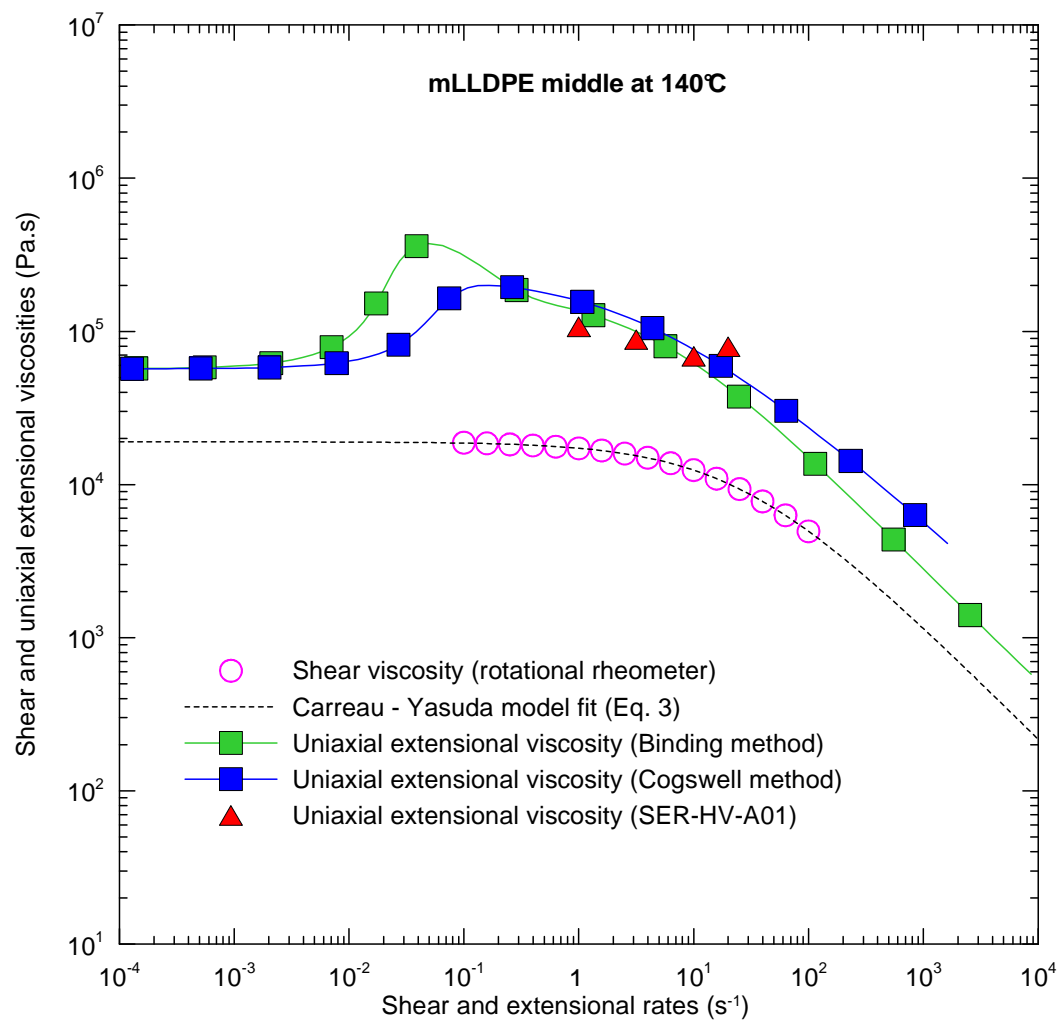


Fig. 41. Comparison between uncorrected/corrected Binding, Cogswell extensional viscosity data and SER measurements for slightly branched mLLDPE (middle) at 140°C. Shear viscosity data obtained from rotational rheometer are also provided in this Figure

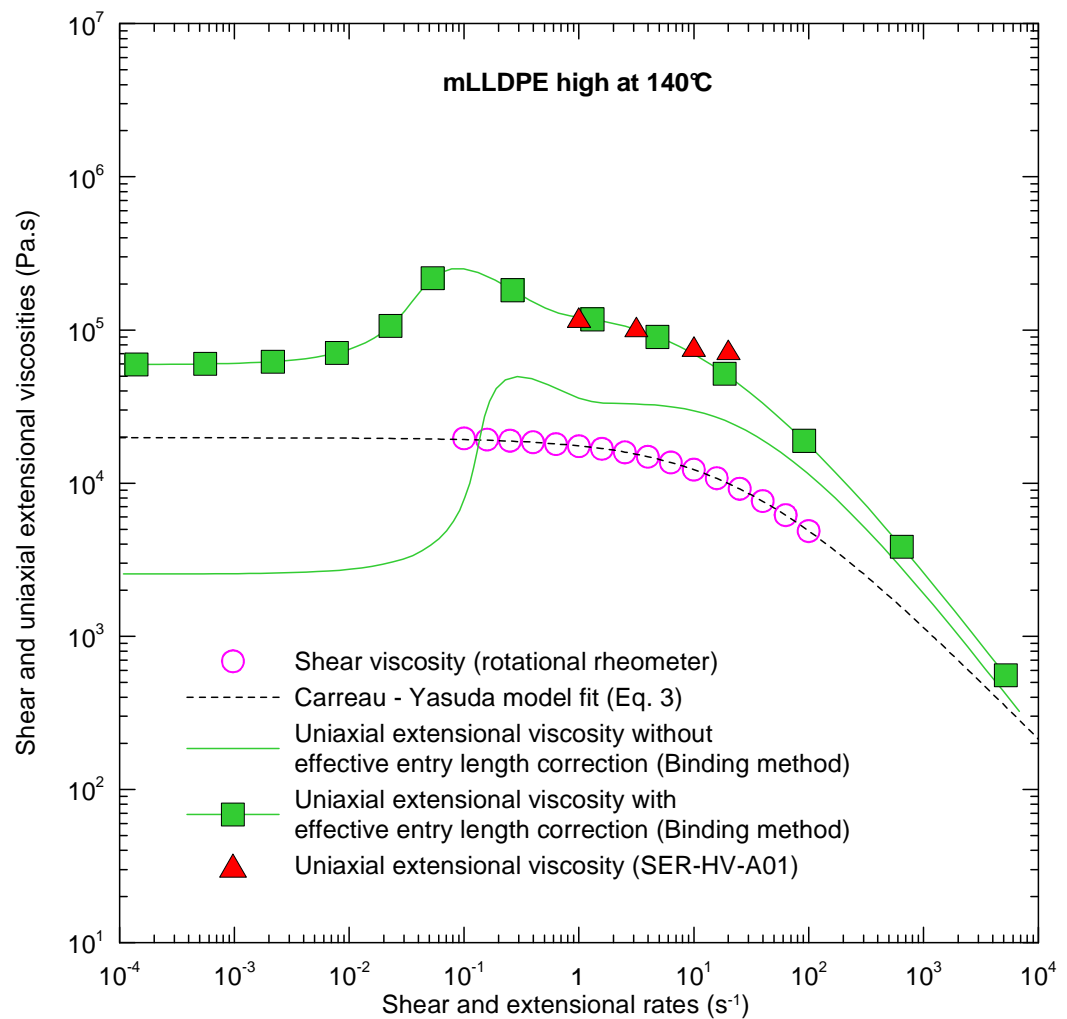


Fig. 42. Comparison between uncorrected/corrected Binding extensional viscosity data and SER measurements for highly branched mLLDPE (high) at 140°C. Shear viscosity data obtained from rotational rheometer are also provided in this Figure

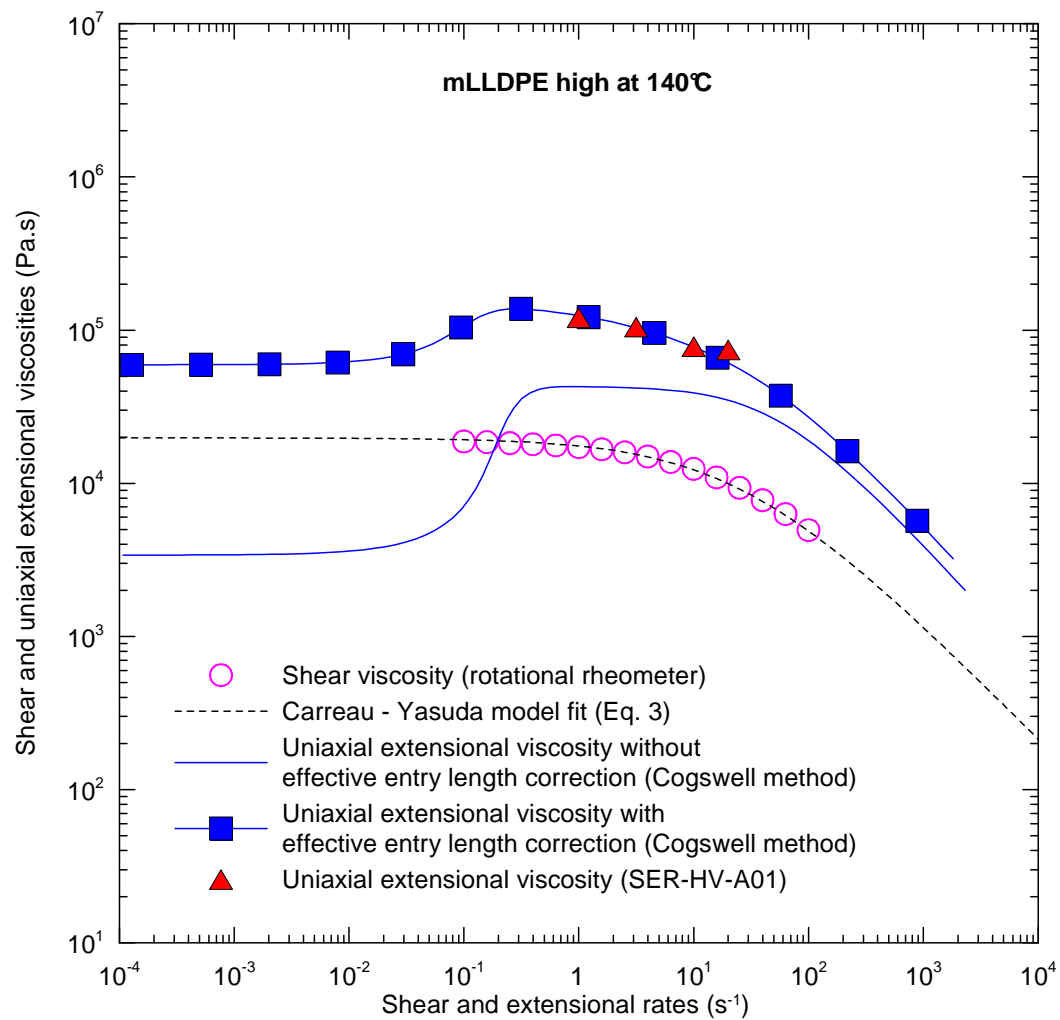


Fig. 43. Comparison between uncorrected/corrected Cogswell extensional viscosity data and SER measurements for highly branched mLLDPE (high) at 140°C. Shear viscosity data obtained from rotational rheometer are also provided in this Figure

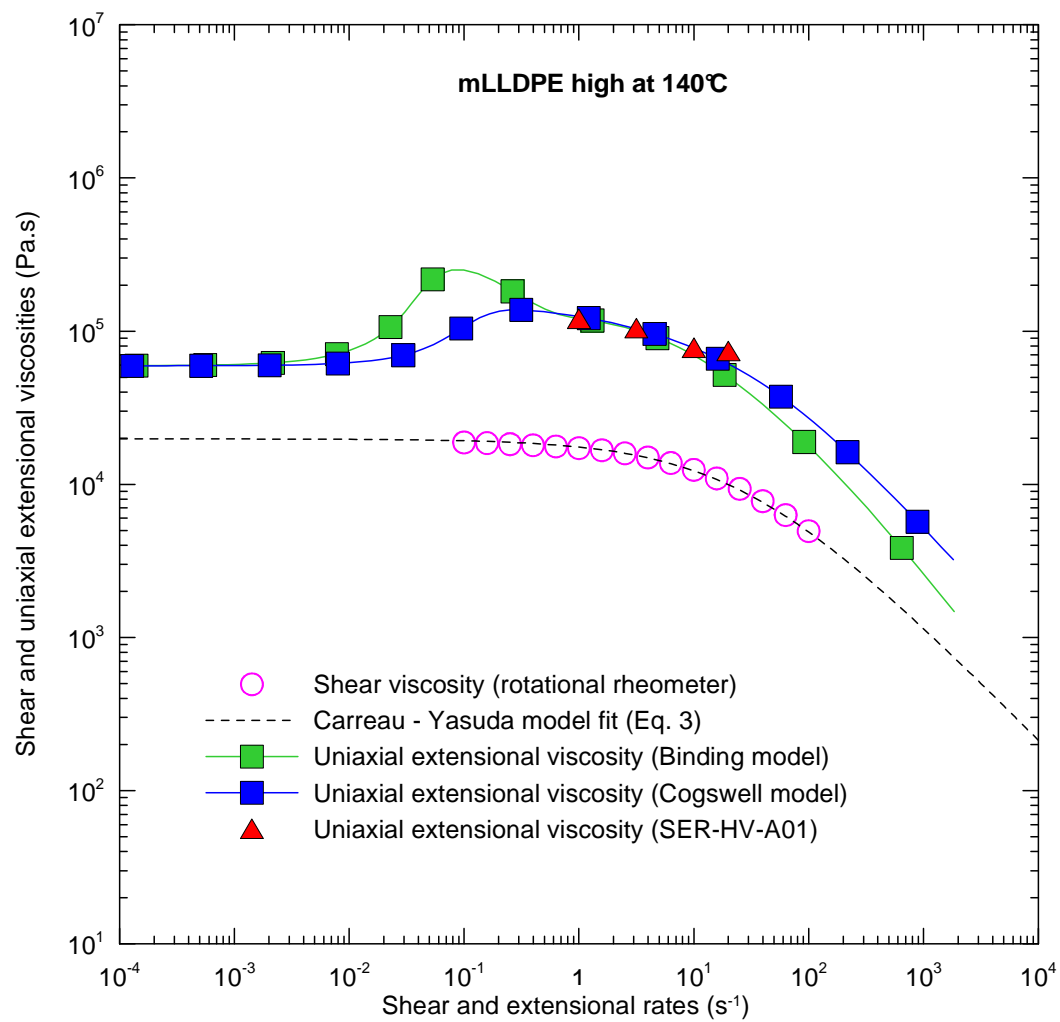


Fig. 44. Comparison between uncorrected/corrected Binding, Cogswell extensional viscosity data and SER measurements for highly branched mLLDPE (high) at 140°C. Shear viscosity data obtained from rotational rheometer are also provided in this Figure

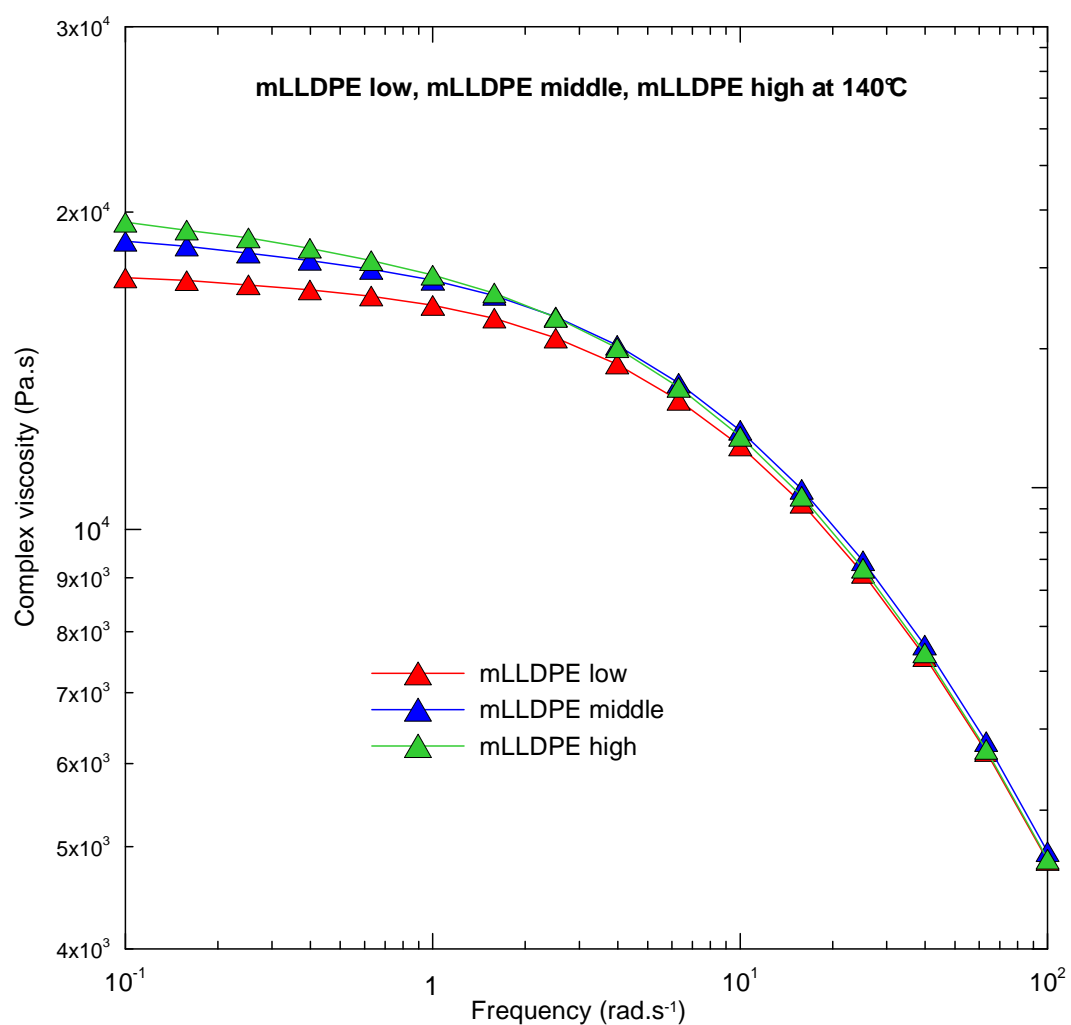


Fig. 45. Complex viscosity data for three mLLDPEs having different level of long chain branching obtained experimentally by ARES rotational rheometer at 140°C

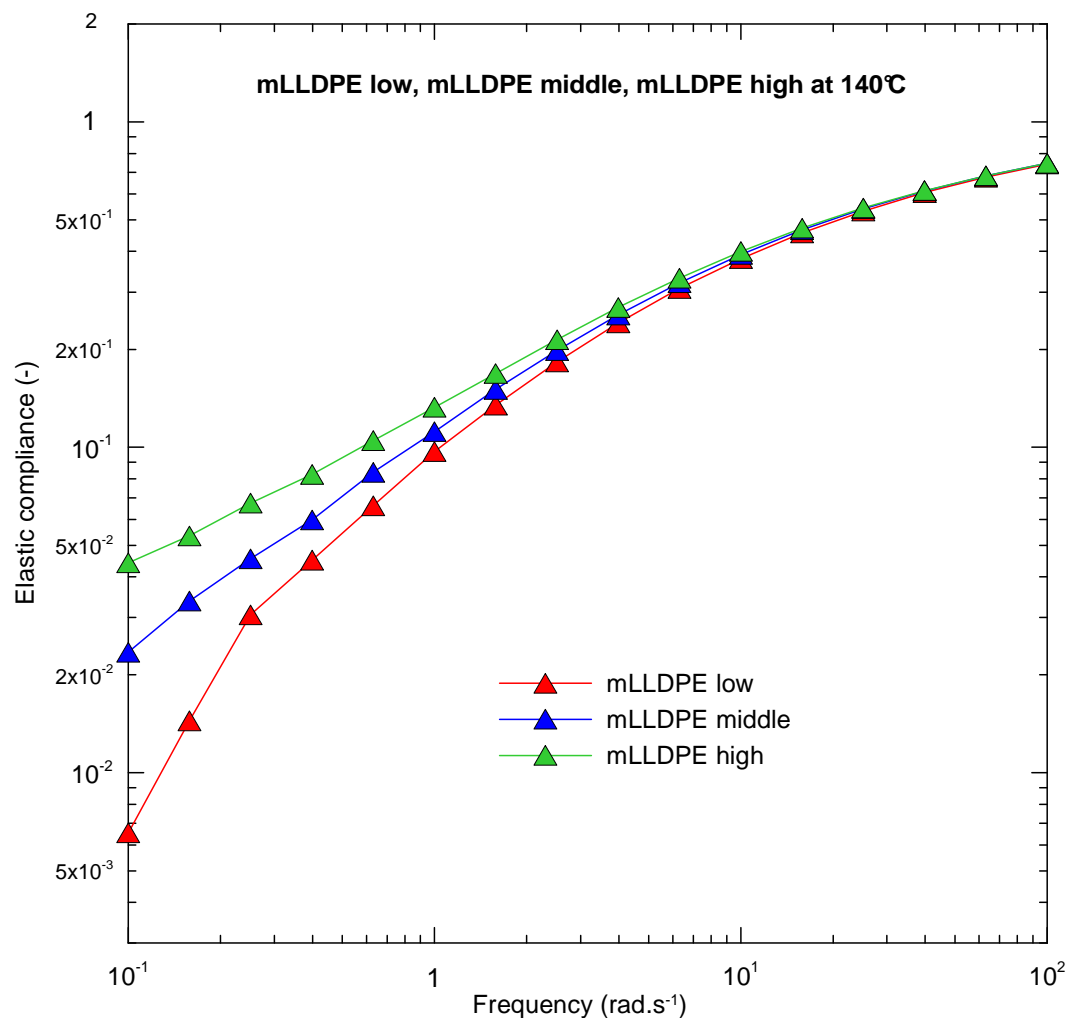


Fig. 46. Elastic compliance data for three mLLDPEs having different level of long chain branching obtained experimentally by ARES rotational rheometer at 140°C

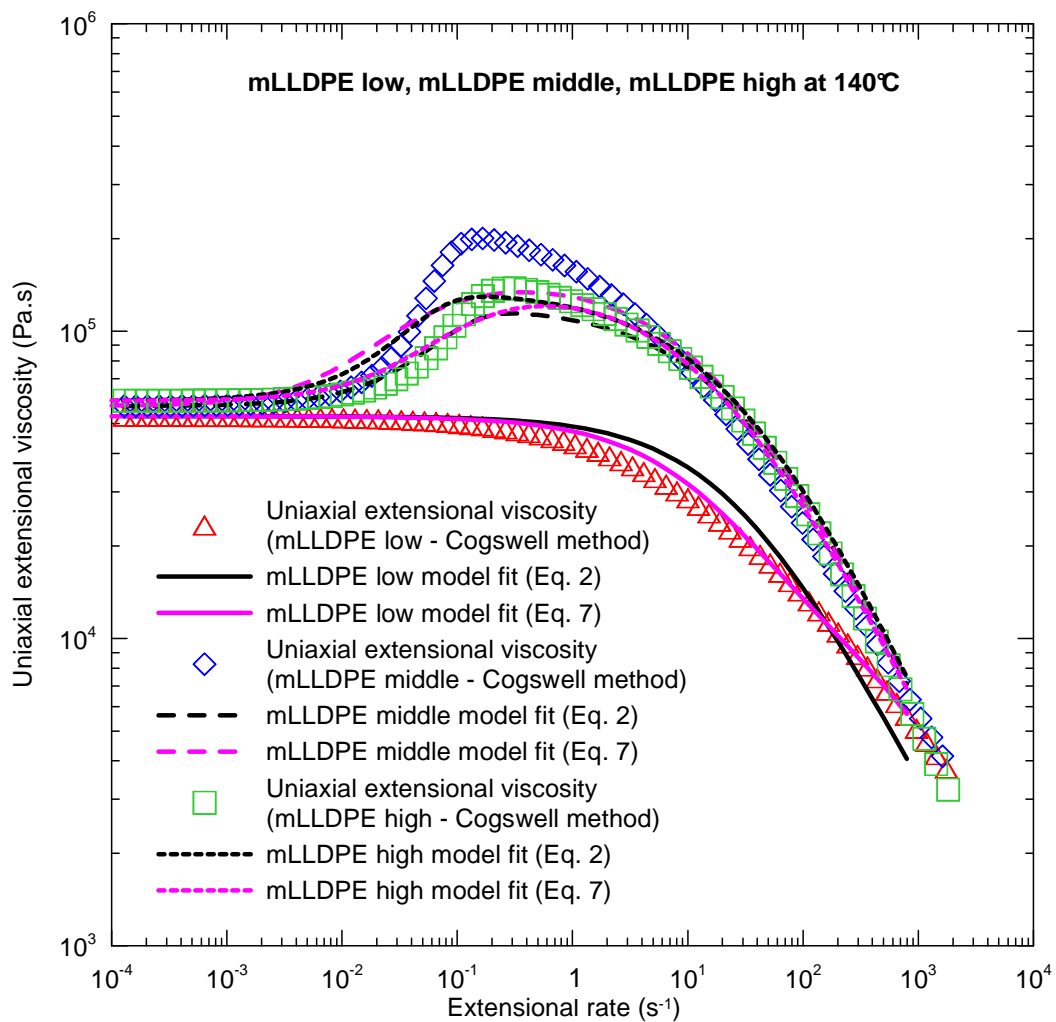
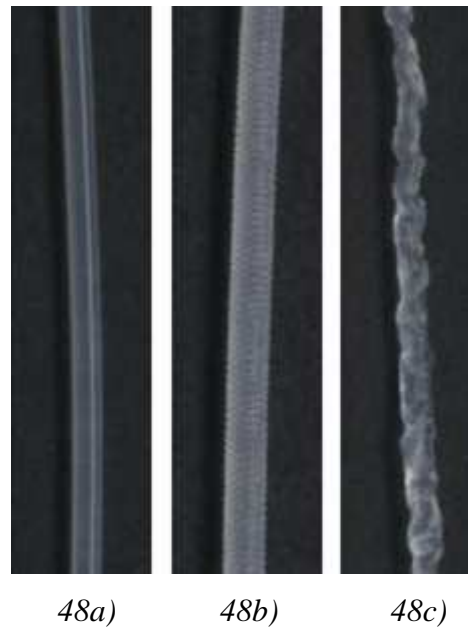


Fig. 47. Comparison between corrected Cogswell uniaxial extensional viscosity data and fitting lines given by generalized Maxwell model according Barnes [24] and generalized Newton model according to Zatloukal et. al. [23] for three mLLDPEs having different level of long chain branching obtained at 140°C

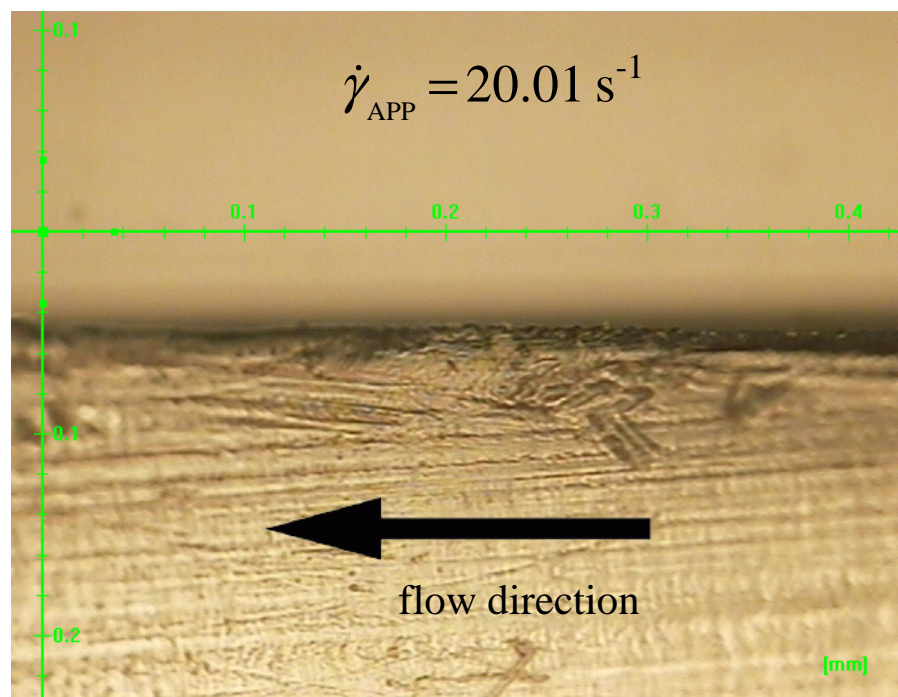


48a)

48b)

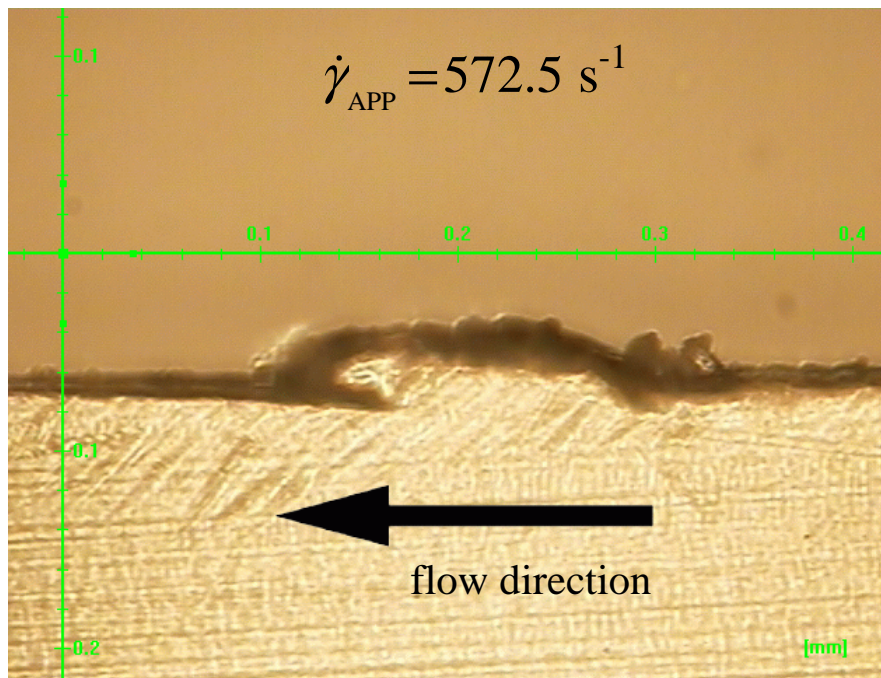
48c)

48d)



The Fig. 48 description is provided on the next page

48e)



48f)

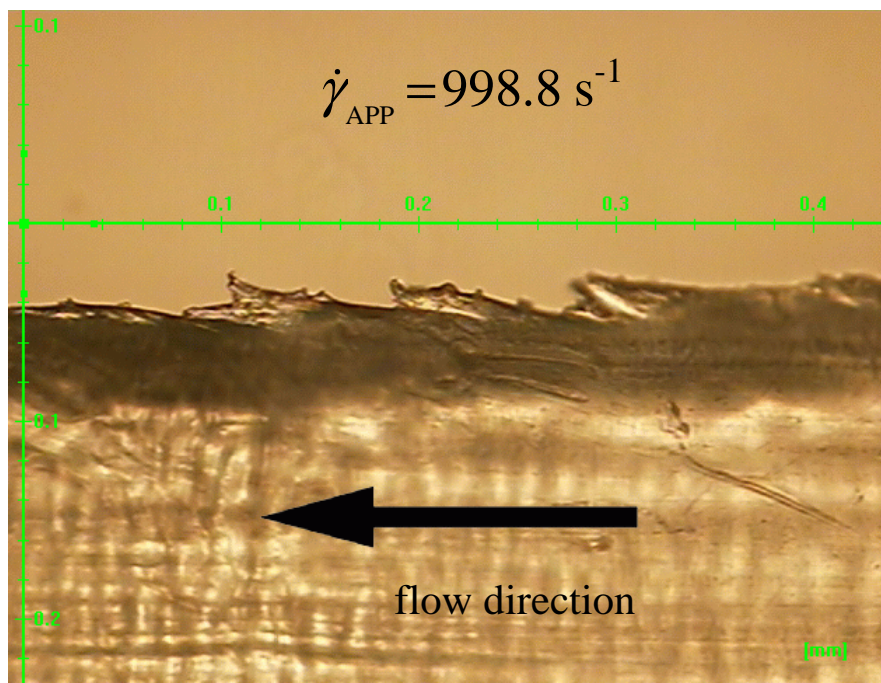


Fig. 48. Extrudate defects development observed during the mLLDPE extrusion. 48a) Stable flow; 48b) Unstable flow - shark skin phenomenon; 48c) Unstable flow - gross melt fracture; 48d) Extrudate cut in the flow direction under stable condition; 48e) Extrudate cut in the flow direction at the shark skin onset; 48f) Extrudate cut in the flow direction for fully developed shark skin

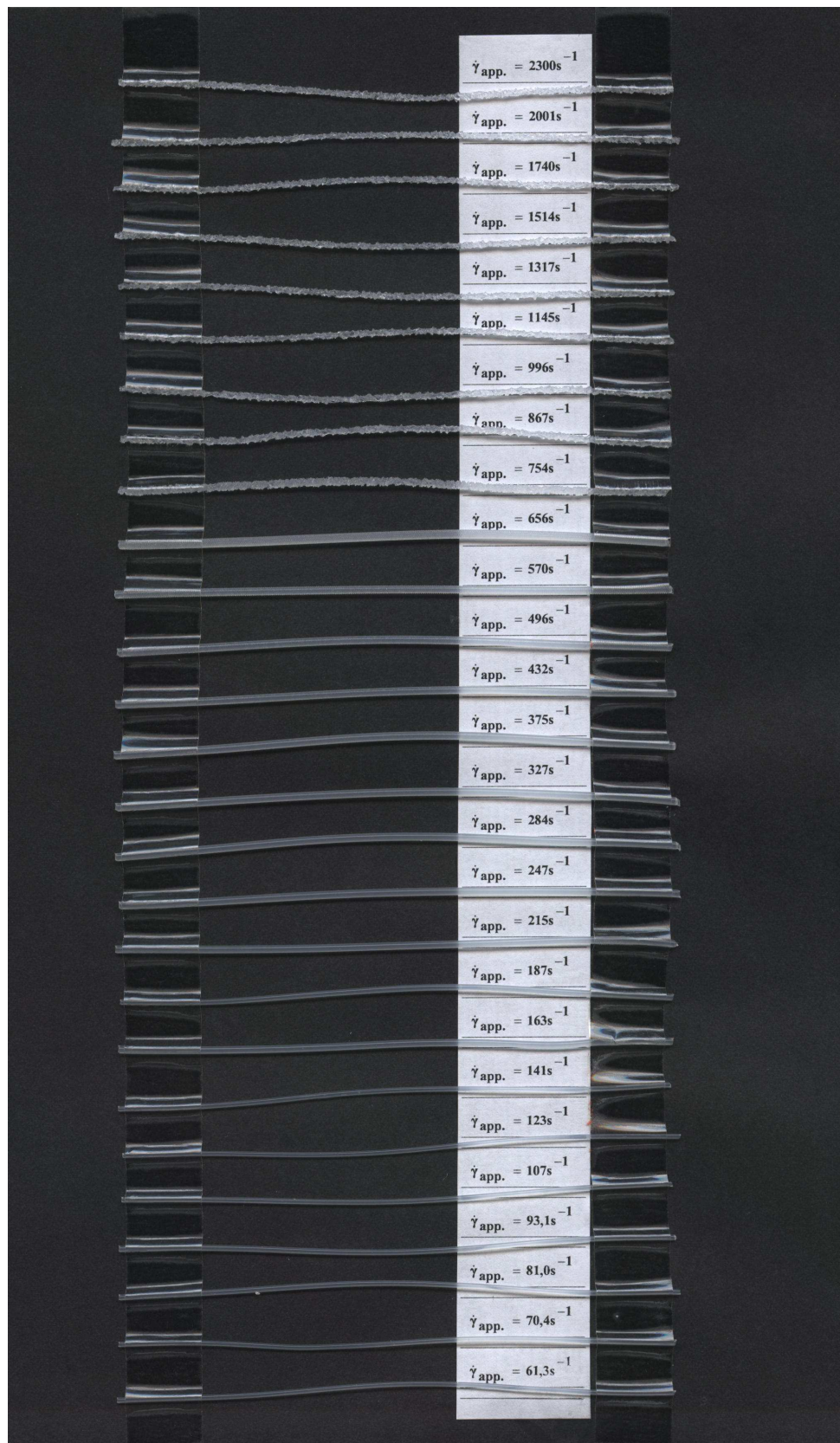


Fig. 49. Linear mLLDPE (low) extrudate samples obtained from orifice die ($L/D=0$, $D=1$ mm) at $140^\circ C$ for wide range of apparent shear rates ($61,3-2300 s^{-1}$)

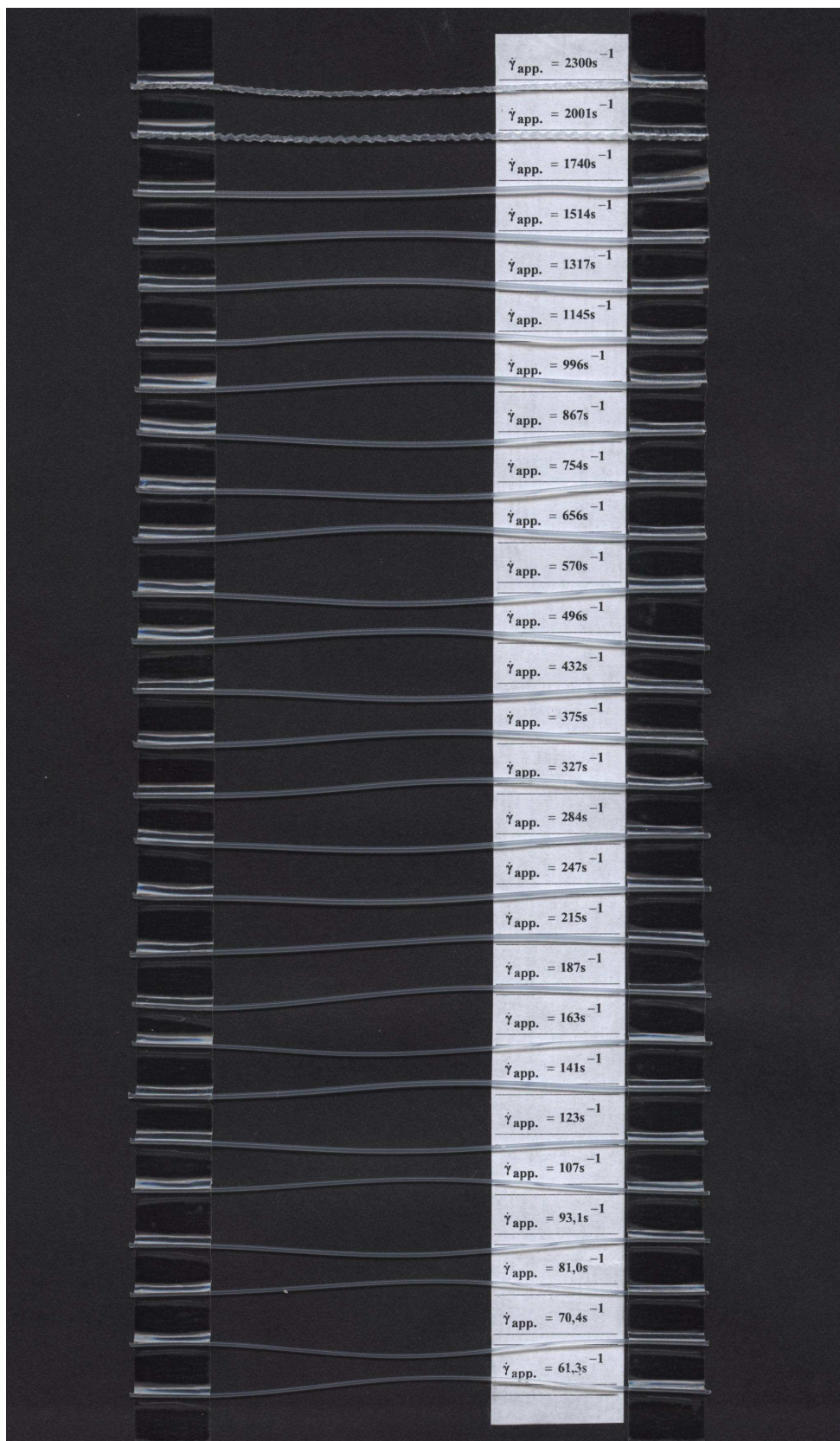


Fig. 50. Linear mLLDPE (low) extrudate samples obtained from long capillary die ($L/D=16$, $D=1$ mm) at 140°C for wide range of apparent shear rates ($61,3\text{-}2300\text{ s}^{-1}$)

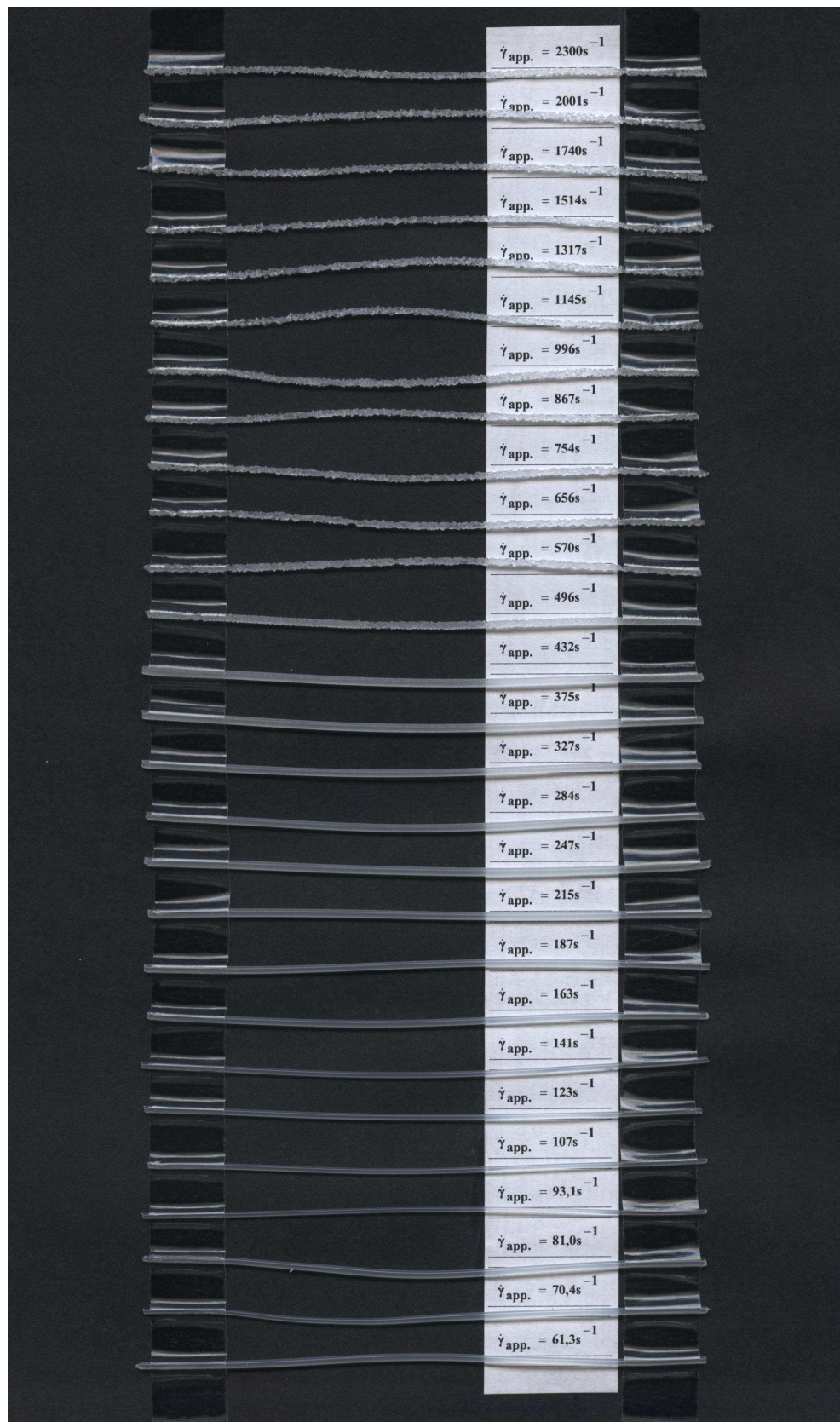


Fig. 51. Slightly branched mLLDPE (middle) extrudate samples obtained from orifice die ($L/D=0$, $D=1$ mm) at $140^\circ C$ for wide range of apparent shear rates ($61,3-2300 s^{-1}$)

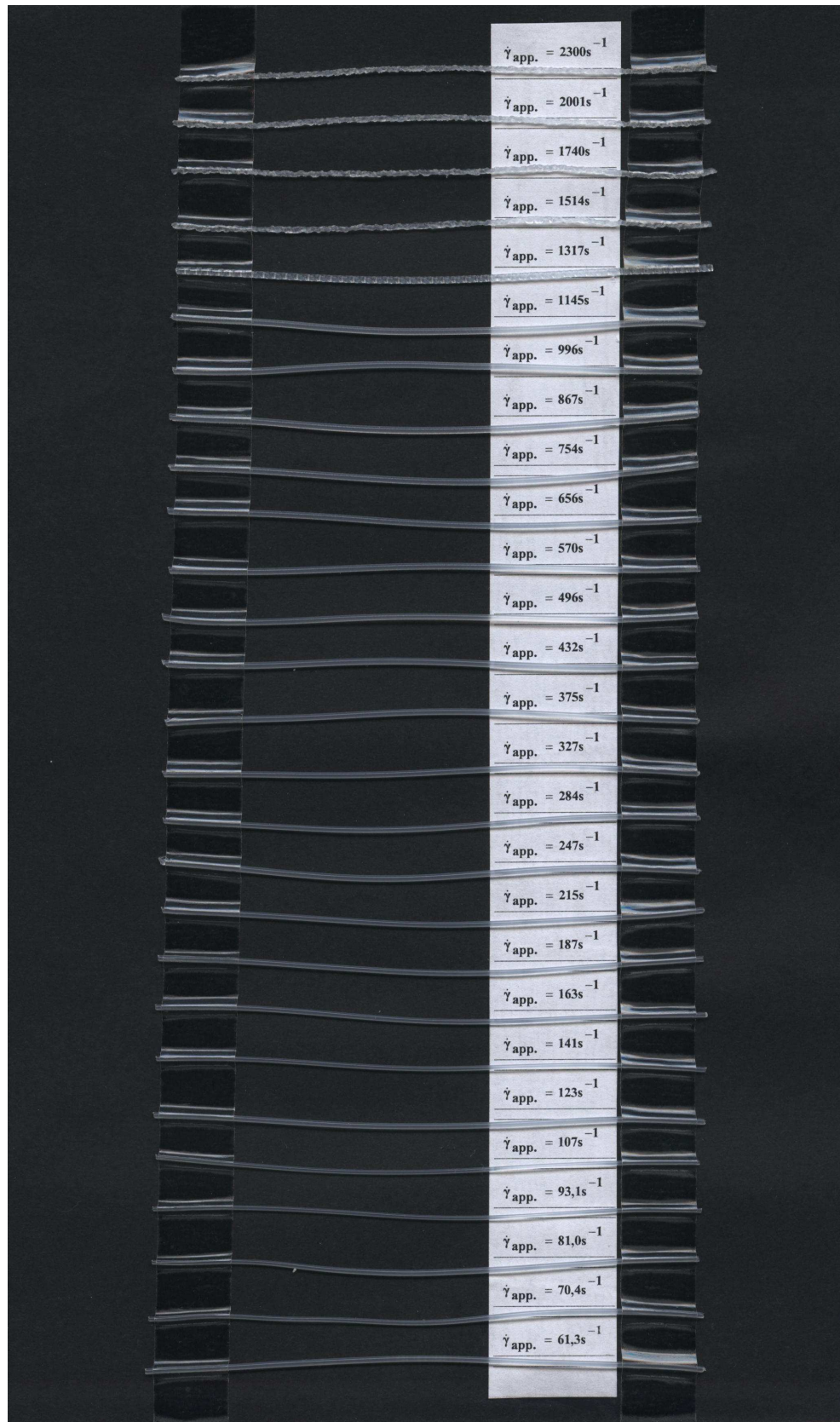


Fig. 52. Slightly branched mLLDPE (middle) extrudate samples obtained from long capillary die ($L/D=16$, $D=1$ mm) at $140^\circ C$ for wide range of apparent shear rates ($61,3-2300 s^{-1}$)

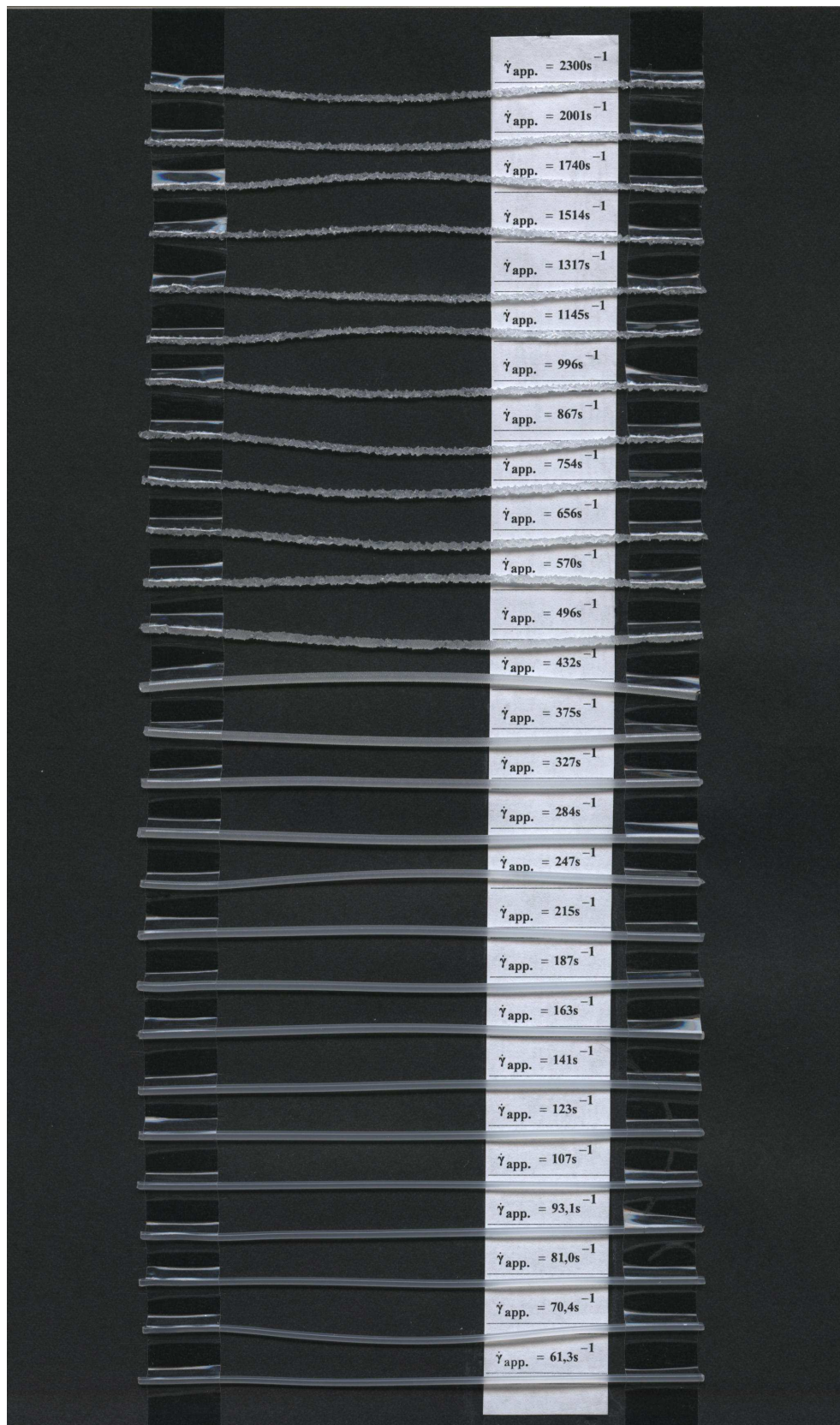


Fig. 53. Highly branched mLLDPE (high) extrudate samples obtained from orifice die ($L/D=0$, $D=1$ mm) at $140^\circ C$ for wide range of apparent shear rates ($61,3-2300 s^{-1}$)

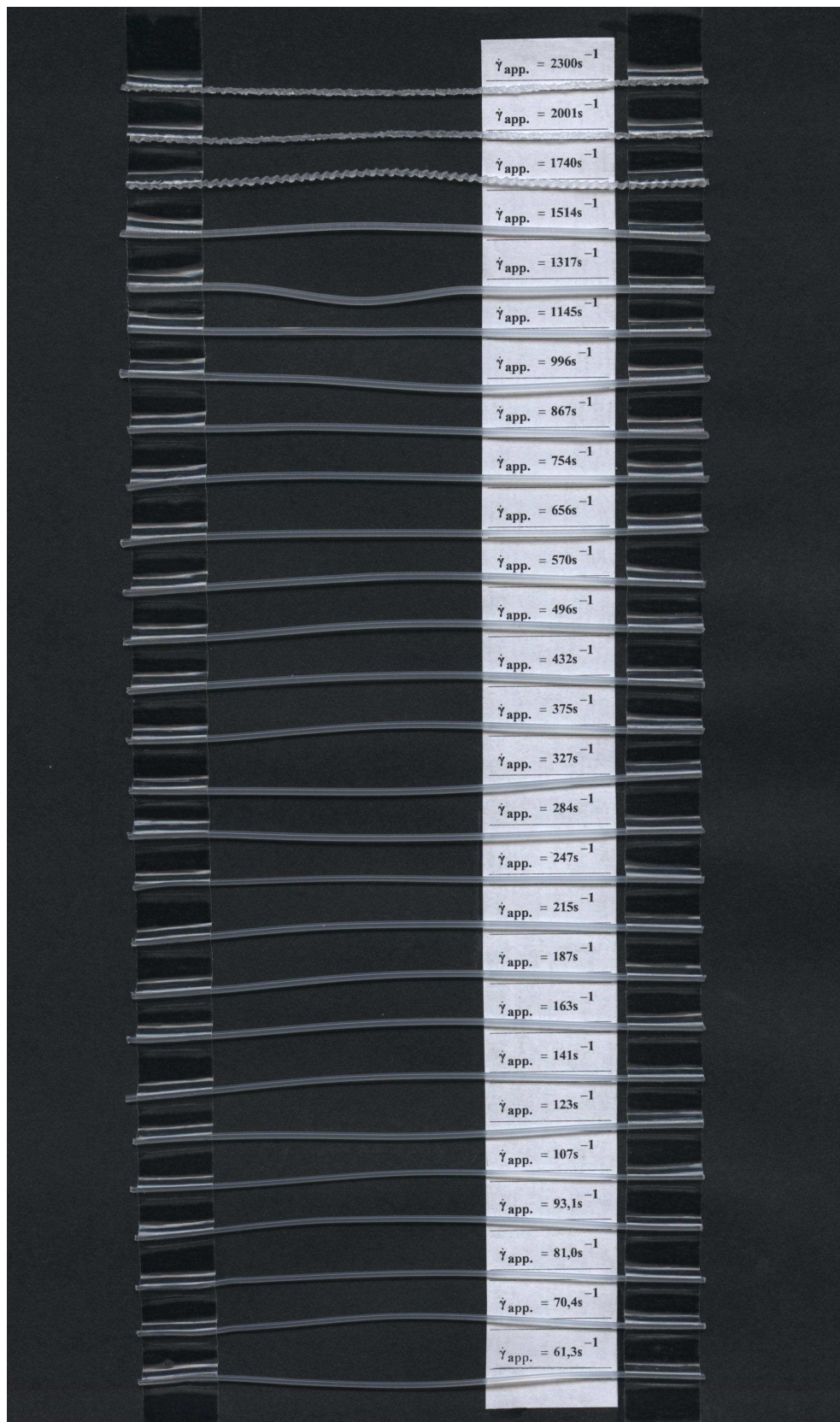


Fig. 54. Highly branched mLLDPE (high) extrudate samples obtained from long capillary die ($L/D=16$, $D=1$ mm) at $140^\circ C$ for wide range of apparent shear rates ($61,3-2300 s^{-1}$)

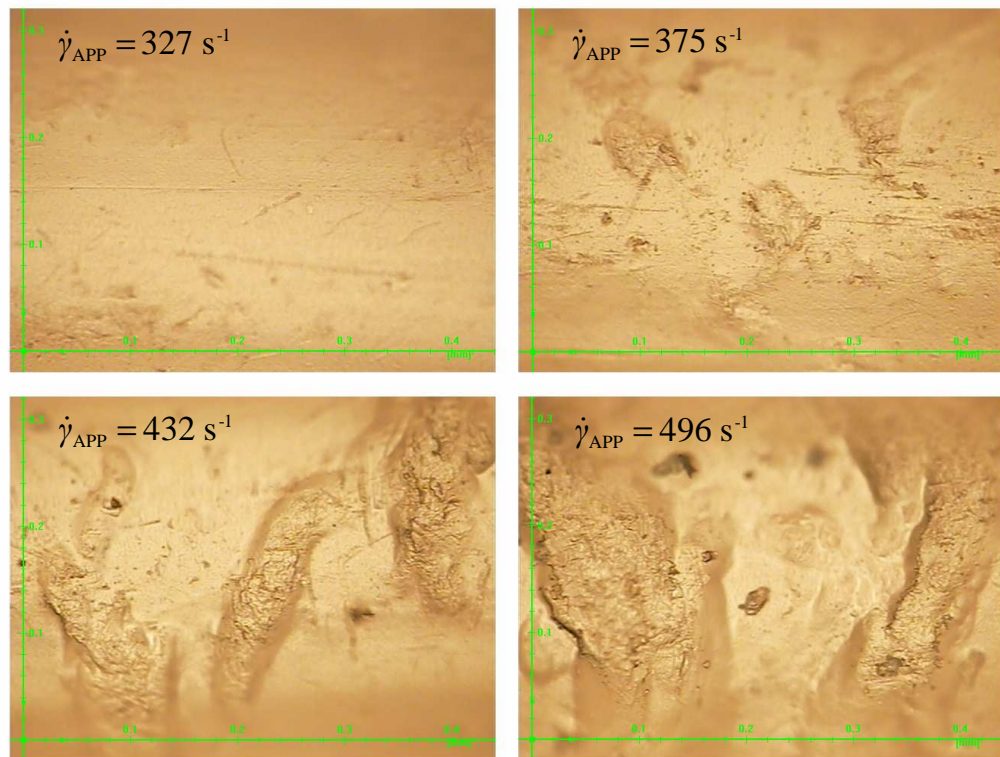


Fig. 55. Surface details of the linear mLLDPE (low) extrudates at different apparent shear rates; T=140°C

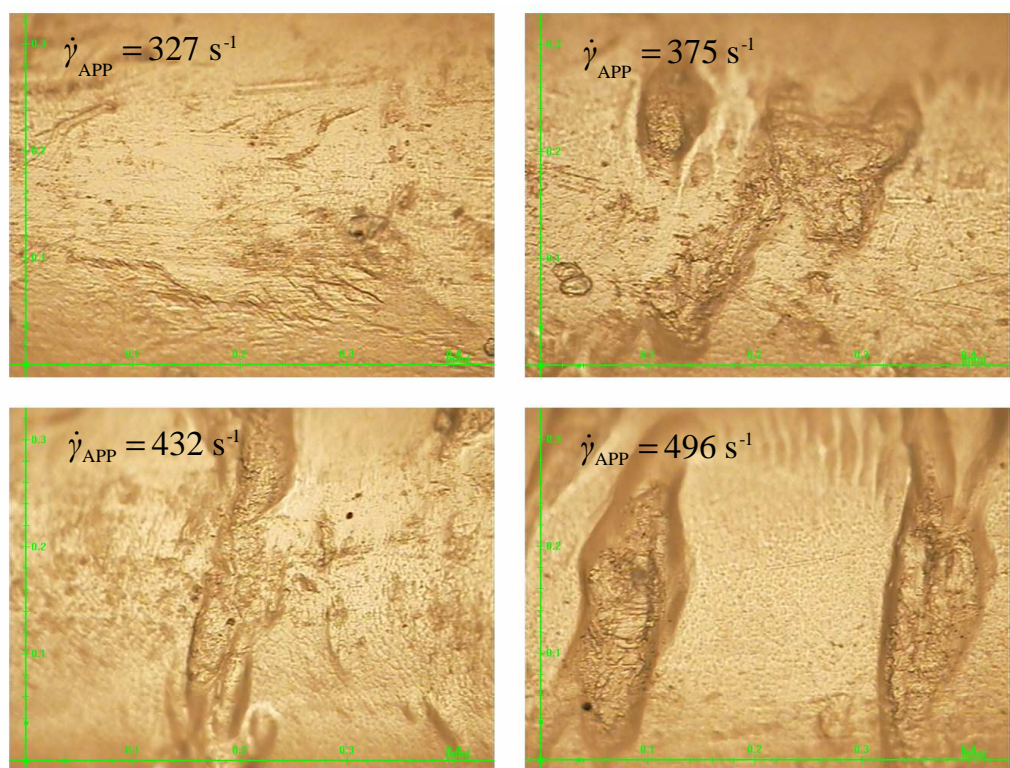


Fig. 56. Surface details of highly branched mLLDPE (high) extrudates at different apparent shear rates; T=140°C

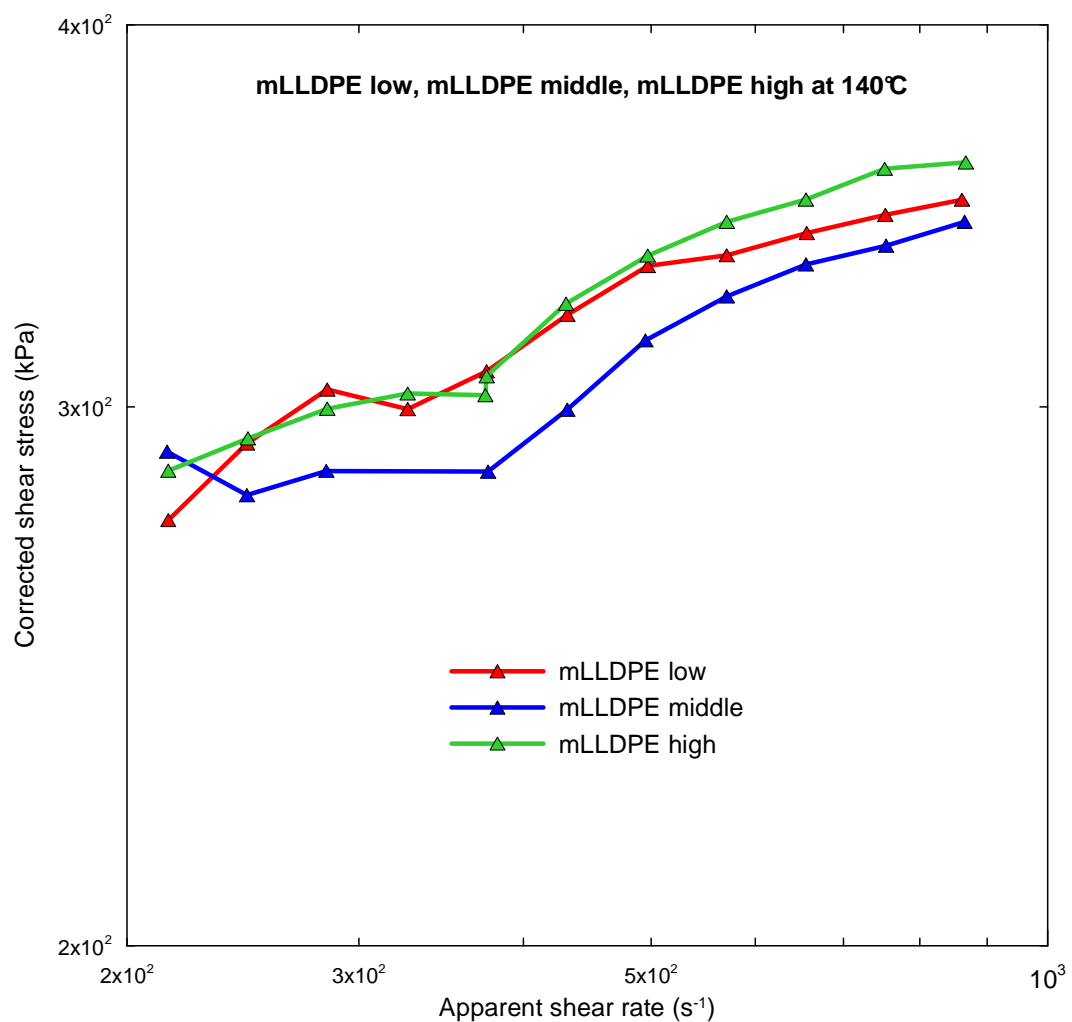


Fig. 57. Comparison between wall shear stress at very high apparent shear rates for three mLLDPEs having different level of long chain branching measured by capillary rheometer at 140°C

CONCLUSION REMARKS

1. It has been shown that very sensitive pressure transducer (250 PSI) with specific care during its calibration has to be done to obtain reasonable entrance viscosity data.
2. For two highly branched LDPEs, it has been revealed that the steady uniaxial extensional viscosity determined by the corrected Cogswell and Binding methods is in acceptable agreement with the SER uniaxial extensional viscosity data. In more detail, both methods tend to slightly undervalue the strain hardening level in contrary to SER data in this case. Finally, the effective entry length correction has been found to be crucially important procedure to get reasonable extensional viscosity data from the measure entrance viscosities. On the other hand, for linear as well branched mLLDPEs, it has been revealed that both, corrected Cogswell and Binding methods have very good capability to describe the extensional viscosity which has been confirmed by direct comparison with SER extensional viscosity data.
3. It has been found that increase in the long chain branching of mLLDPEs increases extensional strain hardening, Newtonian viscosity and elastic compliance.
4. It also has been revealed that both, generalized Maxwell model according to Barnes-Roberts [24] and generalized Newton model according to Zatloukal et.al [23] has good capability to quantify the level of extensional strain hardening and thus, indirectly, also the level of long chain branching in the mLLDPE melts.
5. It has been shown that processibility of the mLLDPEs in extrusion processes can be improved by increasing of long chain branching up to its optimum level. On the other hand, continues additional increase of long chain branching in mLLDPE melts may lead to flow stability decrease leading to narrower processing window.

REFERENCES

- [1] KANAI, T., CAMPBELL, G. A.: *Film processing*, Hanser Publishers, Munich, Germany, 1999.
- [2] MAŇAS, M., VLČEK, J.: *Aplikovaná reologie*, Univerzita Tomáše Bati ve Zlíně, Zlín, Česká republika, 2001.
- [3] ROSATO, D. V.: *Extruding Plastics – Practical processing handbook*, ChapmanHall, Massachusetts, USA, 1998.
- [4] VLACHOPOULOS, J., VLČEK, J.: *Polymer rheology and processing*, McMaster University, Hamilton, Canada, 1994.
- [5] VLACHOPOULOS, J., WAGNER, J. R.: *The SPE Guide on Extrusion Technology and Troubleshooting*, Society of Plastics Engineers, Brookfield, USA, 2001.
- [6] MORRISON, F. A.: *Understanding rheology*, Oxford university press, Inc., New York, USA, 2001.
- [7] COGSWELL, F. N.: *Polymer melt rheology – a guide for industrial practice*, Woodhead publishing limited, Cambridge, England, 1994.
- [8] MÜNSTEDT, H.: *New universal extensional rheometer for polymer melts*, J. Rheol., 23, p. 421-436, 1979.
- [9] SENTMANAT, M. L.: *Miniature universal testing platform: from extensional melt rheology to solid-state deformation behaviour*, Rheol. Acta, 43, p. 657-669, 2004.
- [10] SENTMANAT, M. L., WANG, B. N., MCKINLEY, G. H.: *Measuring the transient extensional viscosity of polyethylene melts using the SER universal testing platform*, J. Rheol., 49 (3), p. 585-606, 2005.
- [11] ZATLOUKAL, M., VLČEK, J., TZOGANAKIS, C., SÁHA, P.: *Improvement in techniques for the determination of extensional rheological data from entrance flows: computational and experimental analysis*, J. Non-Newtonian Fluid Mech., 107, p. 13-37, 2002.
- [12] AGASSANT, J. F., AVENAS, P., SERGENT, J. P., CARREAU, P. J.: *Polymer processing*, Hanser Verlag, Munich, Germany, 1991.

- [13] PÖTSCH, G., MICHAELI, W.: *Injection molding*, Hanser Publishers, Munich, Germany, 1995.
- [14] MÜNSTEDT, H., AUHL, D.: *Rheological measuring and their relevance for molecular characterization of polymers*, J. Non-Newtonian Fluid Mech., 128, p. 62-69, 2005.
- [15] HACHMANN, P., MEISSNER, J.: *Rheometer for equibiaxial and planar elongations of polymer melts*, J. Rheol., 47(4), p. 989-1010, 2003.
- [16] COGSWELL, F. N.: *Converging flow of polymer melts in extrusion dies*, Polym. Eng. Sci. 12, p. 64-73, 1972.
- [17] BINDING, D. M.: *An approximate analysis for contraction and converging flows*, J. Non-Newtonian Fluid Mech. 27, p. 173-189, 1988.
- [18] GIBSON, A. G.: *Die entry flows of reinforced polymers*, Composites, 20, p. 57-64, 1989.
- [19] Xpansion Instruments, www.xinst.com [online]. c2005 [cit. 2006-05-27]. Available at WWW: <http://www.xinst.com/products_modes.htm>.
- [20] BIRD, R. B., ARMSTRONG, R. C., HASSAGER, O.: *Dynamics of polymer liquids (Vol.1)*, John Wiley & Sons, New York, USA, 1987.
- [21] ZATLOUKAL, M., KOPYTKO, W., LENGÁLOVÁ, A., VLČEK, J.: *Theoretical and experimental analysis of interfacial instabilities in coextrusion flows*, 98, p. 153-162, 2005.
- [22] LARSON, R.G.: *Constitutive Equations for Polymer Melts and Solutions*, Butterworth Publisher, Boston, Massachusetts, USA, 1988.
- [23] ZATLOUKAL, M., MAVRIDIS, H., VLČEK, J., SÁHA, P.: *Modeling of non-isothermal film blowing process by using variational principles*, SPE ANTEC 825-829, Charlotte, USA, 2006.
- [24] BARNES, H. A., ROBERTS, G. P.: *A simple empirical model describing the steady-state shear and extensional viscosities of polymer melts*, J. Non-Newtonian Fluid Mech. 44, p. 113-126, 1992.

- [25] ZATLOUKAL, M.: *Differential viscoelastic constitutive equations for polymer melts in steady shear and elongational flows*, J. Non-Newtonian Fluid Mech., 113, p. 209-227, 2003.
- [26] PIVOKONSKY, R., ZATLOUKAL, M., FILIP, P.: *On the predictive/fitting capabilities of the advanced differential constitutive equations for branched LDPE melts*, J. of Non-Newtonian Fluid Mech., 135(1), p. 58-67, 2006.

LIST OF SYMBOLS

τ	Extra stress tensor	Pa
η_0	Newtonian viscosity	Pa.s
$\underline{\underline{D}}$	Deformation rate tensor	s ⁻¹
T	Temperature	°C
II_D	Second invariant of deformation rate tensor	1
III_D	Third invariant of deformation rate tensor	1
a_t	Arrhenius equation for temperature – dependent shift factor	1
E_a	Activation energy	J
R	Universal gas constant	J.mol ⁻¹ .K ⁻¹
T_r	Reference temperature	°C
λ	Relaxation time	s
a	Adjustable parameter in Carreau-Yasuda function	1
\bar{n}	Adjustable parameter in Carreau-Yasuda function	1
α	Extensional strain-hardening-parameter in Generalized Newtonian model	1
ζ	Adjustable parameter in Generalized Newtonian model	1
η_E	Uniaxial extensional viscosity	Pa.s
τ_{xx}	Normal stress	Pa
τ_{yy}	Normal stress	Pa
$\dot{\varepsilon}$	Extensional rate	s ⁻¹
τ	Stress tensor	Pa
$\bar{\lambda}(II_D)$	Deformation rate-dependent relaxation time	s
$\underline{\underline{\tau}}^{\nabla}$	Upper convected stress tensor derivate	Pa.s ⁻¹
$\eta(II_D)$	Deformation rate-dependent viscosity	Pa.s

λ_0	Constant in Generalized Maxwell model	s
K_1	Constant in Generalized Maxwell model	s
L_{0C}	Length of orifice capillary die	m
L_{LC}	Length of long capillary die	m
D_{0C}	Diameter of orifice capillary die	m
D_{LC}	Diameter of long capillary die	m
D_B	Diameter of capillary rheometer barrel	m
P_{LC}	Pressure drop measured on the long capillary die	Pa
P_{0C}	Pressure drop measured on the orifice capillary die	Pa
R_c	Capillary radius	m
τ_{xy}	Shear stress	Pa
$\dot{\gamma}_{APP}$	Apparent shear rate	s^{-1}
Q	Volume flow rate	$m^3 \cdot s^{-1}$
n	Power-law index	1
η	Shear viscosity	Pa.s
$\dot{\gamma}$	Shear rate	s^{-1}
η_{ENT}	Apparent entrance viscosity	Pa.s
$\eta_{ENT,0}$	Plateau-value of entrance viscosity in entrance viscosity model	Pa.s
λ'	Entrance viscosity model parameter	s
a'	Entrance viscosity model parameter	1
α'	Entrance viscosity model parameter	s
β'	Entrance viscosity model parameter	1
ξ'	Entrance viscosity model parameter	1
m	Index of consistence	$Pa \cdot s^n$

$\eta_{ENT,C}$	Corrected entrance viscosity	Pa.s
$\left(\frac{L_{OC}}{D_{OC}}\right)_a$	Ratio of length to diameter at orifice capillary die	1
$\left(\frac{L_{LC}}{D_{LC}}\right)_b$	Ratio of length to diameter at long capillary die	1
$\eta_{ENT,a}$	Entrance viscosity measured on the orifice capillary die	Pa.s
$\left(\frac{L_C}{D_C}\right)_{Tr}$	Correction factor for orifice die	1
$\eta_{ENT,a,0}$	Entrance viscosity plateau measured on an orifice capillary die	Pa.s
$\eta_{ENT,e}$	Entrance viscosity plateau for Binding and Cogswell method	Pa.s
σ_E	Extensional stress	Pa
τ_{xyC}	Corrected shear stress	Pa
k	Binding model parameter	1
\hat{t}	Binding model parameter	1
I_{nk}	Binding's function	1
ζ	Binding model parameter	1
l	Binding model parameter	Pa.s ^k
F	Tangential stretching force	N
\bar{T}	Torque	Nm
Ω	Drive shaft rotation rate	s ⁻¹
F'	Intermeshing gear force	N
F_F	Friction force	N
O	Master drum's axis of rotation	
O'	Slave drum's axis of rotation	
t	Time	s

A_0	Initial cross-section area	m^2
ρ_s	Solid-state density	$\text{kg}\cdot\text{m}^{-3}$
ρ_M	Melt density of the sample	$\text{kg}\cdot\text{m}^{-3}$
$\eta_E^+(t)$	Tensile stress growth function	$\text{Pa}\cdot\text{s}$
ω	Frequency	$\text{rad}\cdot\text{s}^{-1}$
G'	Storage modulus	Pa
G''	Loss modulus	Pa
η^*	Complex viscosity	$\text{Pa}\cdot\text{s}$
M_n	Number average of molecular weight	$\text{g}\cdot\text{mol}^{-1}$
M_w	Weight average of molecular weight	$\text{g}\cdot\text{mol}^{-1}$
π	Ludolf's number	1
N_1	First normal stress difference	Pa

LIST OF FIGURES

<i>Fig. 1. Flow through extrusion die (material is flowing from left to right).....</i>	13
<i>Fig. 2. Calendering</i>	13
<i>Fig. 3. Injection moulding</i>	14
<i>Fig. 4. Fiber spinning</i>	14
<i>Fig. 5. Tubular film blowing</i>	15
<i>Fig. 6. Schematic drawing of Münstedt tensile rheometer</i>	16
<i>Fig. 7. Scheme of Meissner's metal belt clamping rheometer producing equibiaxial and planar elongational flows.....</i>	17
<i>Fig. 8. Sample clamping by metal belts</i>	18
<i>Fig. 9. Scheme of capillary rheometer.....</i>	19
<i>Fig. 10. Scheme of SER Universal Testing Platform. This type is mounted on Controled - Rate rotational rheometer Configuration (CRR), which has a separate motor and transducer (L_0 - unsupported length, Ω - drive shaft rotation rate, \bar{T} - torque, F- tangential force).....</i>	20
<i>Fig. 11. Behaviour of the sample during the experiment on SER.....</i>	21
<i>Fig. 12. Comparison of the capabilities of SER Universal Testing Platform and other melt rheometer technologies</i>	21
<i>Fig. 13. Linear and branched molecule of polymers.....</i>	23
<i>Fig. 14. Linear and branched molecule at shear flow</i>	23
<i>Fig. 15. Linear and branched molecule at shear flow</i>	24
<i>Fig. 16. Linear and branched molecule at elongational flow</i>	25
<i>Fig. 17. Photo of Rosand RH7-2 twin-bore capillary rheometer</i>	31
<i>Fig. 18. Scheme of twin-bore capillary rheometer</i>	32
<i>Fig. 19. Detail of long (left) and orifice (right) capillary dies</i>	33
<i>Fig. 20. Photo of Advanced Rheometric Expansion System ARES.....</i>	40
<i>Fig. 21. Photo of SER-HV-A01 Universal Testing Platform mounted in ARES.....</i>	41
<i>Fig. 22. Force diagram of SER Universal Testing Platform</i>	42
<i>Fig. 23. Five times repeated measurements of the entrance viscosity for LDPE Escorene material with no pressure calibration between the measurements at 200°C</i>	52

Fig. 24. Five times repeated measurements of the entrance viscosity for LDPE Escorene material with pressure calibration made between the measurements at 200°C. The solid line represents the entrance viscosity model fit (Eq. 16)	53
Fig. 25. Entrance viscosity for LDPE Lupolen material 150°C with applied pressure calibration. The solid line represents the entrance viscosity model fit (Eq. 16).....	54
Fig. 26. Comparison between uncorrected/corrected Binding extensional viscosity data and SER measurements for LDPE Escorene at 200°C. Shear viscosity data obtained from rotational and capillary rheometer are also provided in this Figure	55
Fig. 27. Comparison between uncorrected/corrected Cogswell extensional viscosity data and SER measurements for LDPE Escorene at 200°C. Shear viscosity data obtained from rotational and capillary rheometer are also provided in this Figure	56
Fig. 28. Comparison between uncorrected/corrected Binding (low extensional rate range), Cogswell (high extensional rate range) extensional viscosity data and SER measurements for LDPE Escorene at 200°C. Shear viscosity data obtained from rotational and capillary rheometer are also provided in this Figure	57
Fig. 29. Comparison between uncorrected/corrected Binding extensional viscosity data and SER measurements for LDPE Lupolen at 150°C. Shear viscosity data obtained from rotational rheometer are also provided in this Figure	58
Fig. 30. Comparison between uncorrected/corrected Cogswell extensional viscosity data and SER measurements for LDPE Lupolen at 150°C. Shear viscosity data obtained from rotational rheometer are also provided in this Figure	59
Fig. 31. Comparison between uncorrected/corrected Binding (low extensional rate range), Cogswell (high extensional rate range) extensional viscosity data and SER measurements for LDPE Lupolen at 150°C. Shear viscosity data obtained from rotational rheometer are also provided in this Figure	60
Fig. 32. Transient uniaxial extensional viscosity data for three mLLDPEs having different level of long chain branching obtained by SER at 140°C	61

Fig. 33. Entrance viscosity for linear mLLDPE (low) at 140°C with applied pressure calibration. The solid line represents the entrance viscosity model fit (Eq. 16).....	62
Fig. 34. Entrance viscosity for slightly branched mLLDPE (middle) at 140°C with applied pressure calibration. The solid line represents the entrance viscosity model fit (Eq. 16).....	63
Fig. 35. Entrance viscosity for highly branched mLLDPE (high) at 140°C with applied pressure calibration. The solid line represents the entrance viscosity model fit (Eq. 16).....	64
Fig. 36. Comparison between uncorrected/corrected Binding extensional viscosity data and SER measurements for linear mLLDPE (low) at 140°C. Shear viscosity data obtained from rotational rheometer are also provided in this Figure	65
Fig. 37. Comparison between uncorrected/corrected Cogswell extensional viscosity data and SER measurements for linear mLLDPE (low) at 140°C. Shear viscosity data obtained from rotational rheometer are also provided in this Figure	66
Fig. 38. Comparison between uncorrected/corrected Binding, Cogswell extensional viscosity data and SER measurements for linear mLLDPE (low) at 140°C. Shear viscosity data obtained from rotational rheometer are also provided in this Figure	67
Fig. 39. Comparison between uncorrected/corrected Binding extensional viscosity data and SER measurements for slightly branched mLLDPE (middle) at 140°C. Shear viscosity data obtained from rotational rheometer are also provided in this Figure	68
Fig. 40. Comparison between uncorrected/corrected Cogswell extensional viscosity data and SER measurements for slightly branched mLLDPE (middle) at 140°C. Shear viscosity data obtained from rotational rheometer are also provided in this Figure	69
Fig. 41. Comparison between uncorrected/corrected Binding, Cogswell extensional viscosity data and SER measurements for slightly branched mLLDPE (middle) at 140°C. Shear viscosity data obtained from rotational rheometer are also provided in this Figure	70

Fig. 42. Comparison between uncorrected/corrected Binding extensional viscosity data and SER measurements for highly branched mLLDPE (high) at 140°C. Shear viscosity data obtained from rotational rheometer are also provided in this Figure	71
Fig. 43. Comparison between uncorrected/corrected Cogswell extensional viscosity data and SER measurements for highly branched mLLDPE (high) at 140°C. Shear viscosity data obtained from rotational rheometer are also provided in this Figure	72
Fig. 44. Comparison between uncorrected/corrected Binding, Cogswell extensional viscosity data and SER measurements for highly branched mLLDPE (high) at 140°C. Shear viscosity data obtained from rotational rheometer are also provided in this Figure	73
Fig. 45. Complex viscosity data for three mLLDPEs having different level of long chain branching obtained experimentally by ARES rotational rheometer at 140°C	74
Fig. 46. Elastic compliance data for three mLLDPEs having different level of long chain branching obtained experimentally by ARES rotational rheometer at 140°C	75
Fig. 47. Comparison between corrected Cogswell uniaxial extensional viscosity data and fitting lines given by generalized Maxwell model according Barnes [24] and generalized Newton model according to Zatloukal et. al. [23] for three mLLDPEs having different level of long chain branching obtained at 140°C	76
Fig. 48. Extrudate defects development observed during the mLLDPE extrusion. 48a) Stable flow; 48b) Unstable flow - shark skin phenomenon; 48c) Unstable flow - gross melt fracture; 48d) Extrudate cut in the flow direction under stable condition; 48e) Extrudate cut in the flow direction at the shark skin onset; 48f) Extrudate cut in the flow direction for fully developed shark skin.....	78
Fig. 49. Linear mLLDPE (low) extrudate samples obtained from orifice die (L/D=0, D=1mm) at 140°C for wide range of apparent shear rates (61.3- 2300 s ⁻¹)	79

Fig. 50. Linear mLLDPE (low) extrudate samples obtained from long capillary die (L/D=16, D=1mm) at 140°C for wide range of apparent shear rates (61.3-2300 s ⁻¹)	80
Fig. 51. Slightly branched mLLDPE (middle) extrudate samples obtained from orifice die (L/D=0, D=1mm) at 140°C for wide range of apparent shear rates (61.3-2300 s ⁻¹)	81
Fig. 52. Slightly branched mLLDPE (middle) extrudate samples obtained from long capillary die (L/D=16, D=1mm) at 140°C for wide range of apparent shear rates (61.3-2300 s ⁻¹)	82
Fig. 53. Highly branched mLLDPE (high) extrudate samples obtained from orifice die (L/D=0, D=1mm) at 140°C for wide range of apparent shear rates (61.3-2300 s ⁻¹)	83
Fig. 54. Highly branched mLLDPE (high) extrudate samples obtained from long capillary die (L/D=16, D=1mm) at 140°C for wide range of apparent shear rates (61.3-2300 s ⁻¹)	84
Fig. 55. Surface details of the linear mLLDPE (low) extrudates at different apparent shear rates; T=140°C	85
Fig. 56. Surface details of highly branched mLLDPE (high) extrudates at different apparent shear rates; T=140°C	85
Fig. 57. Comparison between wall shear stress at very high apparent shear rates for three mLLDPEs having different level of long chain branching measured by capillary rheometer at 140°C	86

LIST OF TABLES

Tab. 1. Extensional rheometers overview, (adapted from [6]).....	22
Tab. 2. Parameters of the entrance pressure drop model (Eq. 16) for LDPEs and mLLDPEs	46
Tab. 3. Parameters of Careau-Yasuda model (Eq. 3) for shear viscosity curves of LDPEs	46
Tab. 4. Measured loss and storage modules for investigated mLLDPEs at 140°C.....	48
Tab. 5. Newtonian viscosity (determined at 140°C) and activation energy for mLLDPEs	48
Tab. 6. Function parameters of used constitutive equation for mLLDPE shear and extensional rheology description	49
Tab. 7. Capillary flow stability flow evaluation for mLLDPE samples.....	50

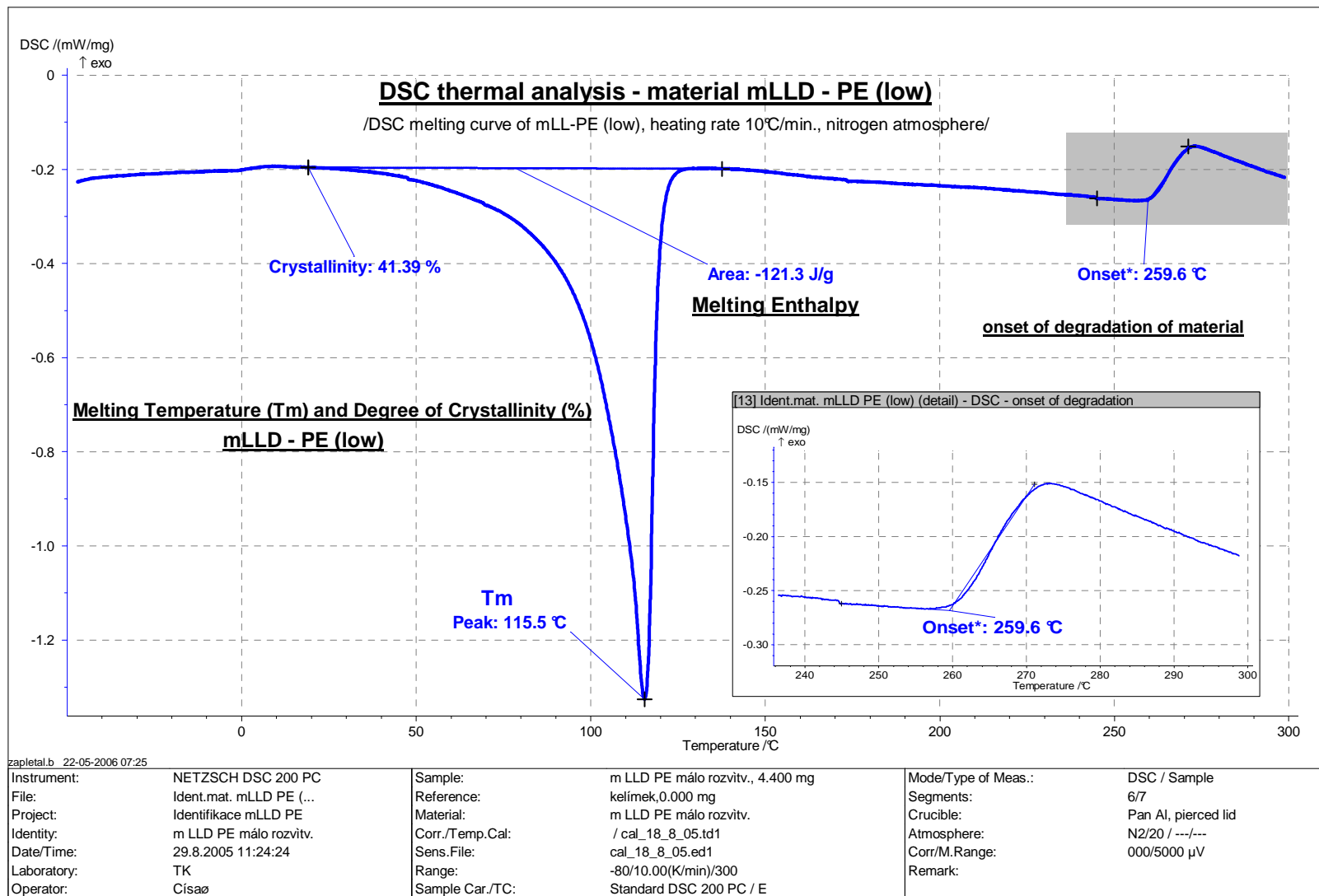
LIST OF APPENDICES

Appendix A I: DSC Thermal analysis

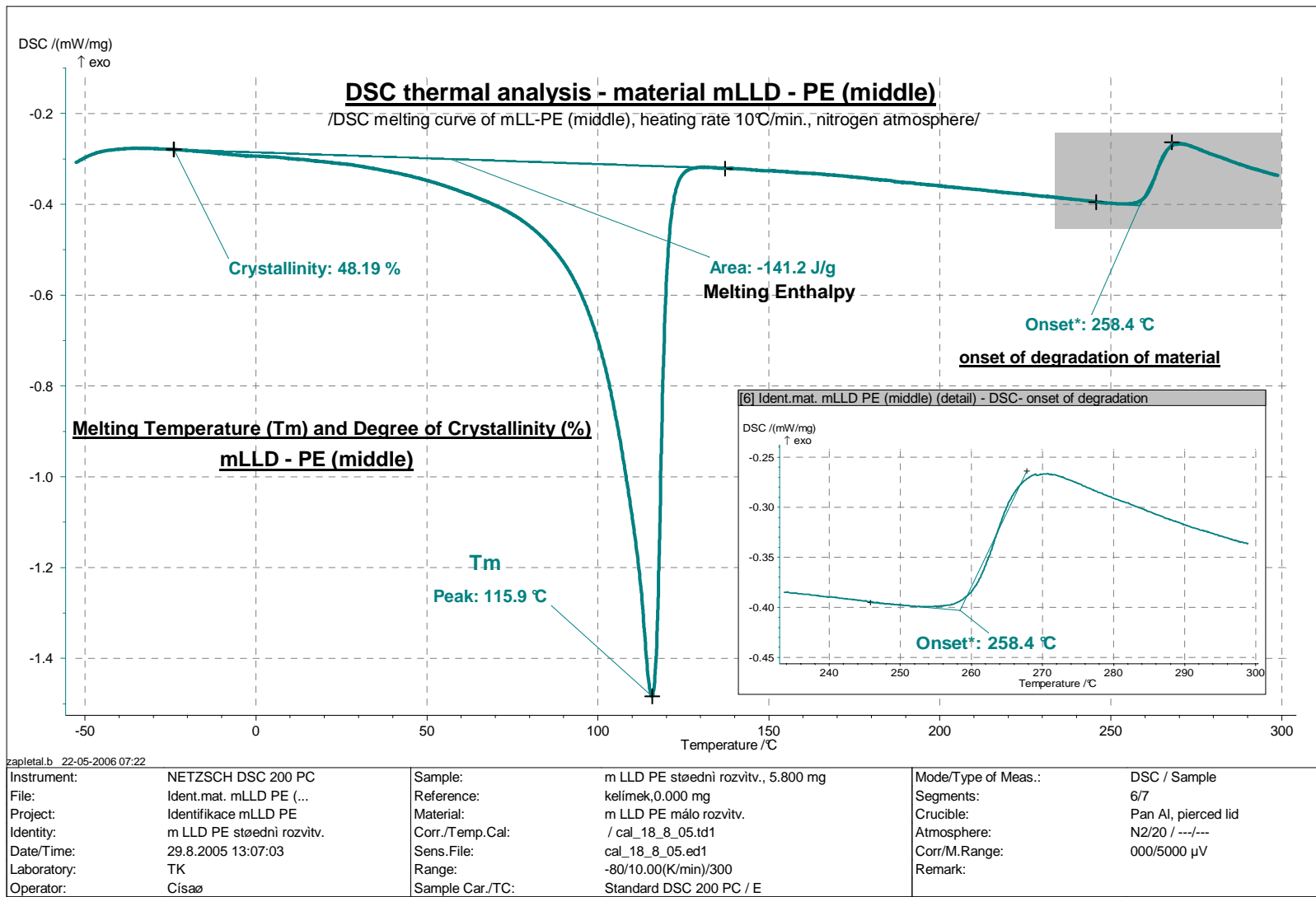
Appendix A II: CD-ROM

APPENDIX A I: DSC THERMAL ANALYSIS

DSC curve for linear mLLDPE (low)



DSC curve for slightly branched mLLDPE (middle)



DSC curve for highly branched mLLDPE (high)

